Systematic Tire Testing and Model Parameterization for Tire Traction on Soft Soil

Rui He

Dissertation submitted to the faculty of the Virginia Polytechnic Institute and State University in partial fulfillment of the requirements for the degree of

Doctor of Philosophy
In
Mechanical Engineering

Corina Sandu, Chair
Adrian Sandu
Saied Taheri
Andrew J. Kurdila

December 13th, 2019
Blacksburg, VA, USA

Keywords: terramechanics, tire off-road dynamics, tire test, soil test; model parameterization, tire tractive performance, soil compaction, multi-pass effect

Systematic Tire Testing and Model Parameterization for Tire Traction on Soft Soil

Rui He

Abstract

Tire performance over soft soil influences the performance of off-road vehicles on soft soil, as the tire is the only force transmitting element between the off-road vehicles and soil during the vehicle operation. One aspect of the tire performance over soft soil is the tire tractive performance on soft soil, and it attracts the attention of vehicle and geotechnical engineers. The vehicle engineer is interested in the tire tractive performance on soft soil because it is related to vehicle mobility and energy efficiency; the geotechnical engineer is concerned about the soil compaction, brought about by the tire traffic, which accompanies the tire tractive performance on soft soil. In order to improve the vehicle mobility and energy efficiency over soft soil and mitigate the soil compaction, it's essential to develop an in-depth understanding of tire tractive performance on soft soil.

This study has enhanced the understanding of tire tractive performance on soft soil and promoted the development of terramechanics & tire model parameterization method through experimental tests. The experimental tests consisted of static tire deflection tests, static tire-soil tests, soil properties tests, and dynamic tire-soil tests. The series of tests (test program) presented herein produced parameterization and validation data that can be used in tire off-road traction dynamics modeling and terramechanics modeling.

The 225/60R16 97S Uniroyal (Michelin) Standard Reference Test Tire (SRTT) and loamy sand were chosen to be studied in the test program. The tests included the quantification or/and measurement of soil properties of the test soil, pre-traffic soil condition, the pressure distribution in the tire contact patch, tire off-road tractive performance, and post-traffic soil compaction. The influence of operational parameters, e.g., tire inflation pressure, tire normal load, tire slip ratio, initial soil compaction, or the number of passes, on the measurement data of tire performance parameters or soil response parameters was also analyzed. New methods of the rolling radius estimation for a tire on soft soil and of the 3-D rut reconstruction were

developed. A multi-pass effect phenomenon, different from any previously observed phenomenon in the available existing literature, was discovered.

The test data was fed into optimization programs for the parameterization of the Bekker's model, a modified Bekker's model, the Magic Formula tire model, and a bulk density estimation model. The modified Bekker's model accounts for the slip sinkage effect which the original Bekker's pressure-sinkage model doesn't. The Magic Formula tire model was adapted to account for the combined influence of tire inflation pressure and initial soil compaction on the tire tractive performance and validated by the test data. The parameterization methods presented herein are new effective terramechanics model parameterization methods, can capture tire-soil interaction which the conventional parameterization methods such as the plate-sinkage test and shear test (not using a tire as the shear tool) cannot sufficiently, and hence can be used to develop tire off-road dynamics models that are heavily based on terramechanics models.

This study has been partially supported by the U.S. Army Engineer Research and Development Center (ERDC) and by the Terramechanics, Multibody, and Vehicle (TMVS) Laboratory at Virginia Tech.

Systematic Tire Testing and Model Parameterization for Tire Traction on Soft Soil

Rui He

General Audience Abstract

Big differences exist between a tire moving in on-road conditions, such as asphalt lanes, and a tire moving in off-road conditions, such as soft soil. For example, for passenger cars commonly driven on asphalt lanes, normally, the tire inflation pressure is suggested to be between 30 and 35 psi; very low inflation pressure is also not suggested. By contrast, for off-road vehicles operated on soft soil, low inflation pressure is recommended for their tires; the inflation pressure of a tractor tire can be as low as 12 psi, for the sake of low post-traffic soil compaction and better tire traction. Besides, unlike the research on tire on-road dynamics, the research on off-road dynamics is still immature, while the physics behind the off-road dynamics could be more complex than the on-road dynamics. In this dissertation, experimental tests were completed to study the factors influencing tire tractive performance and soil behavior, and model parameterization methods were developed for a better prediction of tire off-road dynamics models. Tire or vehicle manufacturers can use the research results or methods presented in this dissertation to offer suggestions for the tire or vehicle operation on soft soil in order to maximize the tractive performance and minimize the post-traffic soil compaction.

Dedication

This dissertation is dedicated to love and peace, science, engineering, art, and beauty.

Acknowledgements

First and most importantly, I would really like to thank Prof. Corina Sandu. I feel blessed and lucky to study with her being my advisor. Since the day she brought me to Virginia Tech, she has been super helpful, patient and tolerant in training me all these years. She also has given me so much freedom in my research and provided me with lots of chances to cooperate with other researchers, to participate in other research projects, and to present my research results in conferences.

I would also like to truly thank my other three Ph.D. committee members: Prof. Adrian Sandu, Prof. Andrew J. Kurdila, and Prof. Saied Taheri. It's my honor to have them in my committee, and their suggestions and feedback have been crucial and polished my research.

My project mentors from ERDC Mr. Javier E. Osorio and Mr. Justin Carrillo have given me supports throughout my ERDC project. They have always been nice, patient, and thought-provoking. It has been really lucky for me to have them as my project mentors. It is an honor for me to work on this ERDC project as ERDC has a long, glorious history in terramechanics research.

I have received support and guidance from a few researchers in Europe and South Africa: Prof. Valentin Ivanov and Dr. Dzmitry Savitski from Technische Universität Ilmenau and Prof. P. Schalk Els from the University of Pretoria. I do appreciate the publication opportunities with these excellent researchers.

I am grateful to my labmates: Dr. Tan Li, Mr. Zhi Chai, Dr. Yitao Zhu, Dr. Anudeep Bhoopalam, Mr. Aamir Khan, Dr. Emilio Jimenez, Mrs. Hoda Mousavi as well her husband Mr. Mehran Shams, Mr. Mohit Shenvi, and some of the CVeSS labmates; I have enjoyed working with and talking to you all, from which I have learned a lot. Dr. Tan Li is one of my role models; in my time at Virginia Tech, I have aspired to work as hard and be as productive as Dr. Tan Li.

I shall also thank my friends in US and China for the incentives and encouragement I got from them during my study at Virginia Tech, and they are Dr. Weifeng Cheng, Dr. Yu Pan, Dr. Sihui Ma and her husband Mr. Jiajun Li, Mr, Chuan Xiao, Mr. Beichen Liu, Miss Jieru

Xie, Mr. Xie He, Mr. Sen Mei, Mr. Shi-tong Xiong, Mr. Yifan Yang, Mr. Yuanzhou Yang, Mr. Jingwei Luo, Dr. Kujin Tang, Miss Sijie Fang, Dr. Taoran Deng (also one of my role models), and Mrs. Lu Sun. Special thanks must be addressed to Mrs. Lu Sun for mentally and enduringly accompanying me like my family in the past five years.

Special thanks shall also be addressed to some of my favorite musicians: Ludwig van Beethoven, Johann Sebastian Bach, Béla Bartók, Dmitri Shostakovich, Allan Holdsworth, Eric Dolphy, Keith Jarrett. Doing research can be so silent a work that makes you feel alone and can be always in one place for a long time. Thanks to their music during my research, I feel hardly alone with adequate sound and comfortable atmosphere, feel like visiting various places, and work with pleasure.

Finally, and equally important, I would like to express my gratitude to my parents, without them, I am nothing; without their endless support and love, I could not have been where I am now.

Just one more thing, I want to thank the creator whom I have always believed in.

"I think it's time we blow this scene. Get everybody and stuff together. Okay, three, two, one let's jam."

- *Cowboy Bebop*

Table of Contents

List of Figures

List of Tables

List of Abbreviations

Abbreviation	Description
AERI	Agricultural Engineering Research Institute
ATV	All-terrain vehicle
CI	Cone index
CIV	CRREL's instrumented vehicle
CRREL	Cold Regions Research and Engineering Laboratory
DE	Drawbar efficiency
DEM	Discrete element method
DOE	Design of experiment
DP	Drawbar pull
DPC	Drawbar pull coefficient
DSCP	Digital Static Cone Penetrometer
DTS test	Dynamic tire-soil test
FEM	Finite element method
GA	Genetic algorithm
GWC	Gravimetric water content
ISC	Initial soil compaction
LSA model	Load-sinkage analytical model
MFTM	Magic Formula tire model
SP test	Soil properties test
SRTT	Standard reference test tire
STS test	Static tire-soil test
SUV	Sport-utility vehicle
SWIFT	Short Wavelength Intermediate Frequency Tyre
TMVS	Terramechanics, Multibody, and Vehicle Systems
T-Rig	Terramechanics Rig
TRV	Traction research vehicle
VWC	Volumetric water content
WITS	Wireless internal tire sensors

Nomenclature

Symbol	Description	Unit
a	Half length of the flattened portion of the tire-soil contact patch	[mm]
$A_{i,\ i = 1, 2, 3, 4}$	Empirical model parameters that relate bulk density to volumetric water content and cone index	
A_c	2D tire-soil contact patch area	
$\alpha_{i,\ i=1, 2, 3, 4}$	Coefficients that relate the Magic Formula model parameters to tire normal load, soil cohesion, and soil friction angle.	
B	Stiffness factor of the MFTM model	
B_i	Model parameter of the LSA model	
b	Geometric parameter of the plate in contact with the soil: the width (or smaller dimension) of a rectangular plate or the radius of a circular plate	[mm]
b_t	Tire section width	[mm]
b_w	Wheel width	[mm]
B_T	Geometry parameter that characterizes the plate dimension for the Terzaghi bearing capacity model	[mm]
b_{ts}	Tire-soil contact patch width	[mm]
$b_{i,\ i=0,1,2,3\ldots}$	Coefficients that relate tire normal load to the MFTM model parameters	
$\beta_{i,\ i=1,\ 2,\ 3\ldots}$	Empirical model parameters of the multi-pass effect model	
C	Shape factor of the MFTM model	
c	Soil cohesion	[kPa]
c_n	Soil cohesion at the nth pass of the multi-pass effect model	
$c_{i,\ i=0,1,2,3\ldots}$	Coefficients that relate tire inflation pressure to the MFTM model parameters	
$C_{i,\ i = 1, 2, 3, 4}$	Empirical model parameters that relate bulk density to gravimetric water content and cone index	
CI	Cone index of soil	[kPa]
C_n	Wheel numeric proposed by Wismer and Luth	
CP	Cross probability	
d	Tire diameter	[mm]
D	Peak value of the MFTM model	
$D_{i,\ i = 1, 2}$	Model parameters of the LSA model	
Δ	Amount of mutation for each gene	
δ	Tire deflection on a hard surface	
DP	Drawbar pull	[kN]
DPC	Drawbar pull coefficient	
d_{rut}	Rut depth	[mm]
$d_{wheel\text{-}soil}$	Vertical distance between wheel center and undisturbed soil surface	[mm]

Symbol	Description	Unit
d_{tr}	Tread depth of tire	[mm]
E	Curvature factor of the MFTM model	
E_Y	Young's modulus	[kPa]
η	Drawbar efficiency	
F	Parameter that controls the disturbance of two random chromosomes on the disturbing vector	
Fz	Tire normal load	[kN]
$G_{i,\ i\ =\ 1,\ 2,\ 3,\ 4}$	Model parameters of the Pokrovski's analytical shear stress-displacement model	
γ_d	Bulk density of soil	[g/cm^3]
γ	Unit weight of soil	[N/m^3]
h_f	Unloaded section height of tire	[mm]
$Itermax$	Max number of iterations	
j	Shear displacement	
K_s	Shear modulus	
K_{sn}	Shear modulus at the nth pass of the multi-pass effect model	
K_t	Tire stiffness in the tangential direction	[kNm^{-1}]
k	Sinkage modulus	
$k_{i,\ i\ =\ 1,\ 2}$	Model parameters of another Reece's model	
k_c	Coefficient that represents the effect of soil cohesion on sinkage modulus for the Bekker's model	
k'_c	Coefficient that represents the effect of soil cohesion on sinkage modulus for the Reece's model	
k_r	Reece's sinkage constant	
k_ϕ	Coefficient that represents the effect of soil frictional angle on sinkage modulus for the Bekker's model	
k'_ϕ	Coefficient that represents the effect of soil frictional angle on sinkage modulus for the Reece's model	
$\lambda_c,\ \lambda_\gamma,\ \lambda_q,$	Shape coefficient of the plate for the Terzaghi bearing capacity model	
MP	Mutation probability	
n	Sinkage exponent	
n_p	Number of pass in the multi-pass effect model	
$n_{i,\ i=0,1}$	Coefficient that relates slip ratio to sinkage exponent	
NP	Number of individuals in the population	
N_{CM}	Mobility number for cohesive soils	
$N_c,\ N_\gamma,\ N_q$	Bearing capacity factors that are function of the soil friction angle and shape coefficients for the Terzaghi bearing capacity model	
ω	Dimensionless coefficient of the LSA model	
ω_w	Wheel angular speed	[rad/s]

Symbol	Description	Unit
p	Pressure	[kPa]
p_{gr}	Average ground pressure in the tire contact patch on a hard ground	[kPa]
$\bar{p}$	Average contact pressure in the tire-soil contact patch	[kPa]
p_i	Tire inflation pressure	[kPa]
ϕ	Soil friction angle	
r_f	Unloaded radius of tire	[mm]
r_0	Rolling radius	[mm]
r	Loaded radius of tire	[mm]
r_w	Wheel radius	[mm]
ρ_p	Tire percent radial deflection	
s	Longitudinal slip ratio	
S_h	Horizontal shift of the MFTM model	
S_v	Vertical shift of the MFTM model	
S_{tire}	Tire sinkage	[mm]
σ	Normal stress	[kPa]
T	Motor torque	[N.m]
τ	Shear stress	kPa
τ_{max}	Shear strength (maximum shear stress that leads so soil failure)	kPa
θ_A	Tire angle at the exit of the flat portion of the tire-soil contact patch (point A)	
θ_t	Arbitrary tire angle	[rad]
θ_g	Gravimetric water content	[g/g]
θ_v	Volumetric water content	[m^3/ m^3]
θ_w	Arbitrary wheel angle	[rad]
θ_{w1}	Wheel entry angle (the acute angle between the centerline of the wheel and the beginning of the wheel-soil contact interface)	[rad]
θ_{w2}	Wheel exit angle (the acute angle between the centerline of the wheel and the end of the wheel-soil contact interface)	[rad]
θ_{wm}	Wheel angle of the maximum radial stress point	[rad]
$u_{i,\ i=1,2,3,\ldots}$	Model parameters of the Upadhyaya et al. empirical DPC model	
V	Disturbing vector	
V_x	Longitudinal velocity at the axle of wheel	[m/s]
X	Magic Formula model input	
X_{best}	Best chromosome of one generation of population	
$X_{p,\ i}$	Chromosome that is crossed with the disturbing vector	
$X_{r,\ i}$	Randomly selected chromosome	
x_m	Optimal model input at the maximum Magic Formula model output	

Symbol	Description	Unit
x_c	X coordinate of the tire-soil contact patch contour	[mm]
ξ	Dimensionless contact pressure concentration coefficient of the LSA model	
Y	Magic Formula model output	
y_m	Maximum Magic Formula model output	
y_s	Asymptotic Magic Formula model output	
z	Sinkage of soil	[mm]
z_t	Sinkage of tire	[mm]
z_0	Sinkage of tire in towing mode	[mm]
z_c	Z coordinate of the tire-soil contact patch contour	[mm]
ζ_1	Model parameter of the parabolic tire-soil contact patch contour model	

Chapter 1

Introduction

In this chapter, the research documented by this dissertation is introduced in terms of the motivation behind this research, the objectives to achieve in this research, and the main contributions of this research. Next, the organization of this dissertation is explained.

1.1 Background and Motivation

Tires mounted onto off-road vehicles are operated on deformable soil (soft soil) in multiple applications, e.g., a military vehicle on unpaved road in a military mission, a heavy-duty vehicle in a construction site, a tractor ploughing on a field, a timber truck in a forest, a racing sport-utility vehicle (SUV) in the Dakar Rally, etc. Because of such applications, lots of research has been conducted previously in industry and academia to study tire-soil interaction that helps engineers to better understand and predict tire performance over soft soil and soil behavior under tire traffic. The study of tire-soil interaction involves knowledge fields such as soil mechanics, terramechanics, tire mechanics and heavily relies on experimental tests such as tire tests, soil tests, and tire-soil tests. The soil test and tire-soil test preferably require sufficient characterizations of the test soil condition and controllable soil condition.

One concern in the study of tire-soil interaction is the tire tractive performance on soft soil. Model useful in tire off-road traction dynamics modeling can be semi-empirical or empirical which means some of its model parameters can be only determined by experimental tests. (The tire off-road traction theoretically accounts for off-road conditions including soft soil.) Some commonly used model parameterization methods, such as the plate-sinkage test and plate-shear test [1], might not be the best choice for tire off-road traction dynamics modeling.

Tire inflation pressure is an operational parameter that is of interest to the tire-soil interaction researchers, because it has been reported that changing tire inflation pressure led to the improvement in tire off-road tractive performance [1] and the reduction in soil compaction that is normally unwanted in agricultural applications [6].

For passenger car tires and multi-purpose vehicle tires, little published test data is accessible on tire off-road tractive performance at a wide range of slip ratio and on the combined effect of tire inflation pressure, slip ratio, and initial soil compaction on tire off-road tractive performance and soil response. Also, little information is available on using tire-soil test data to parameterize classical pressure-sinkage models for the tire off-road traction dynamics modeling. An application of the tire-soil test data to the parameterization of terramechanics model would add a new parameterization method for the tire off-road traction dynamics modeling in addition to the plate-sinkage test and plate-shear test. A very few pieces of existing literature discuss the multi-pass effect, let alone include the test data about the multi-pass effect. Besides, as a common tire on-road tractive performance prediction tool, the Magic Formula tire model only has a very few applications to the tire off-road tractive performance prediction [7], [8]. None of these applications considers the combined influence of tire inflation pressure and initial soil compaction.

1.2 Research Objectives

In order to address the concerns behind the background and motivation as described in previous subsection and to provide new insights into the study of tire traction on soft soil, the research documented in this dissertation was launched. The primary research objectives are listed as below:

1. Perform necessary tire-soil tests, tire tests, or soil tests and develop relevant test methods to measure the parameters and relationships of interest about the tire off-road traction dynamics and the soil response to tire traffic, with the test soil condition being sufficiently characterized and repeatable.

2. Investigate the influence of operational parameters on the parameters and relationships

of interest about the tire off-road traction dynamics and the soil response to tire traffic. Operational parameters include tire inflation pressure, slip ratio, normal load, initial soil compaction, and number of passes.

3. Use the test data to parameterize models useful in the tire off-road traction dynamics modeling (evaluate the model parameters). Develop new parameterization methods for these models that are supposed to capture the physics of tire-soil interaction.

1.3 Research Approach

As for the research objectives listed in the last subsection, the first two research objectives were achieved by the experimental test methods that mainly comprised design of experiments (Table 4.3, Table 4.6, Table 4.7, Table 4.9, Table 4.10, and Table 4.11), the employment of the test facilities and tools (Section 3.1), and the soil preparation method (Section 3.2). Also, the test methods were developed only for the laboratory test, not for the field test.

The accomplishment of the first two research objectives provided the basis for the fulfillment of the third research objective: the test data was fed into optimization programs for model parameterization. The test method and optimization program together formed the proposed model parameterization method.

As for the optimization program, based on some commonly used algorithms, which aims to determine the model parameters, it will require a proper initial guess of model parameters. However, for a highly nonlinear model to which the optimization is applied, it is always difficult to obtain a proper initial guess of model parameters. To get over this, a genetic algorithm (Section 5.2.2) was incorporated into an optimization program for model parameterization in this study.

To model a complex phenomenon and avoid a large computation cost that usually accomplishes most high-fidelity models which are based on the numerical method such as finite element method or discrete element method, the semi-empirical or empirical approach is normally adopted; this also applies to modeling the influence of variations in tire inflation pressure and initial soil compaction on the Magic Formula model output (Section 5.2.4) and

the slip sinkage effect on the Bekker's model parameter (Section 5.3.2).

1.4 Research Contribution

The research documented in this dissertation was intended to study tire tractive performance on soft soil. In this research, a Standard Reference Test Tire (SRTT) and a loamy sand were tested through multiple tire, soil, and tire-soil tests at the TMVS lab, Virginia Tech, and the test data was analyzed and fed into optimization programs to extract model parameters. The principal research contributions are listed below:

- A lab test method was developed to study tire traction on soft soil. The test method includes an estimation method of the rolling radius at low wheel longitudinal speed under various levels of soil compaction, a method to reconstruct the rut formed by the tire traffic, a method to sufficiently characterize the soil condition of the prepared test soil, and an on-site soil compaction evaluation method. (Soil compaction is characterized by bulk density.)

- The combined influence of tire inflation pressure, initial soil compaction, and slip ratio on drawbar pull, rut depth, rut length, tire sinkage, and drawbar efficiency in traction mode; the combined influence of tire inflation pressure, initial soil compaction, and normal load on motion resistance coefficient, rut depth, and rolling radius in towing mode; and the combined influence of initial soil compaction, tire normal load, and tire inflation pressure on loaded radius, rut depth and rut length for a non-rolling tire were analyzed.

- A new phenomenon that involves the multi-pass effect and rut fluctuation is discovered in the laboratory multi-pass tire-soil tests. This phenomenon is different from any phenomenon of the multi-pass effects recorded in the existing literature. A physical explanation was provided about the mechanism behind this phenomenon.

- Parameterization methods were developed for a bulk density estimation model, the Bekker's pressure-sinkage model, a modified Bekker's pressure-sinkage model, and the Magic Formula tire model. In the parameterization methods, the test data was fed

into optimization programs to compute model parameters. The modified Bekker's pressure-sinkage model could account for the slip sinkage effect and has been validated, in terms of the rut depth prediction, against the test data. The Magic Formula tire model was adapted for variations in tire inflation pressure and initial soil compaction; its accuracy in predicting the drawbar pull of tire on soft dry soil was validated against the test data.

- The proposed parameterization method for the Bekker's model or the modified Bekker's model, which uses the rut reconstruction from the laboratory static tire-soil tests or uses the test data from laboratory dynamics tire-soil tests and static tire deflection test (on the rigid ground), is a new Bekker's model parameterization method, compared with the conventional parameterization method based on the plate-sinkage test. The modified Bekker's model, parameterized by this new method, was validated against the test data.

Due to the fact that an SRTT is commonly used in tire tests conducted by tire manufacturers, it was chosen for the experimental and modeling part of this study. Also due to the fact that a large amount of soil that can fill the soil bin of the T-Rig is not always attainable; shipping this amount of soil from the soil provider to the TMVS lab cannot be completed within short time, only the loamy sand was tested in this study. However, the developed test methods and parameterization methods in this study are generally applicable to other tires and soils. The developed test methods can produce parameterization and validation data to be used in tire off-road traction dynamics modeling and terramechanics modeling. The developed parameterization method can be used to develop off-road tire dynamics models.

1.5 Dissertation Outline

This dissertation is organized in six chapters, and each chapter is summarized as follows:

Chapter 1 offers an introduction of this study.

Chapter 2 presents a comprehensive literature review on experimental tests and proposed

models for the study of tire-soil interaction from previous research; the major topics involved are the soil condition characterization and parameters of interest in the experimental tests, the modeling approaches, model parameterization, and crucial relationships & parameters in and tire off-road traction dynamics, the effect of tire inflation pressure on tire off-road tractive performance, and the basic terminology in tire-soil interaction.

Chapter 3 describes the tools & apparatus and soil preparation method for the experimental tests of this study. The functions of the Terramechanics Rig and the use of the tools to measure the soil and tire parameters in the tests and to prepare the soil are explained in this chapter.

Chapter 4 first introduces the relationships between the tests whose design of experiment, procedures, and results for the tests are described next in this chapter; the test data is displayed and analyzed.

Chapter 5 details the evaluation of the model parameters using the test data collected. Models of interest and the proposed model are explained first, followed by the comparison between the test data and the model prediction that uses the model parameters evaluated by the proposed model parameterization methods.

Finally, Chapter 6 summarizes the findings of this study, documents the comments pertinent to this study, and proposes future research directions.

Chapter 2

Literature Review

This chapter includes materials from [10] *by R. He, C. Sandu, A. K. Khan, A. G. Guthrie, P. S. Els and H. A. Hamersma;* [11] *by R. He, C. Sandu, and J. E. Osorio; and* [12] *by R. He, C. Sandu, and J. E. Osorio, with the permission from Elsevier, and the agreement attached.*

The tire-soil interaction influences tire tractive performance on soft soil and soil reaction to tire traffic. Research on multiple aspects of tire-soil interaction has been previously conducted by various approaches. Common modeling and test methods and typical aspects of tire-soil interaction are reviewed in this chapter; the research directions worth exploring of these reviewed topics are also pointed out. This chapter will cover:

- A brief introduction on terminology in tire-soil interaction.
- Soil parameters to characterize the soil condition,
- Relationships and parameters of interest in experimental tests and modeling,
- Tire inflation pressure influences, and
- Existing models in tire off-road traction dynamics

2.1 Basic Terminology in Tire-Soil Interaction

The parameters that characterize the tire-soil contact patch, the tire off-road dynamics, and the soil deformation don't have a uniform definition in existing literature. The definition of the parameters commonly used in the tire on-road dynamics might not work for the tire off-road dynamics because of the difference between the physics of the former and the latter. Therefore, in this section, the basic terminology about tire and soil that is employed in this dissertation is explained.

It is reported in some literature that when the terrain stiffness is significantly lower than the total tire stiffness (the carcass stiffness plus the inflation pressure), the flexible tire on the terrain can be regarded as a rigid wheel (the rigid mode of operation) [13], [14]. However, it was found according to the test data, as it will be presented later in Section 4.3.2, that the test tire on the soil, under the normal load, has non-zero tire deflection (the elastic mode of operation). Given the elastic mode of operation, it is assumed that the tire-soil interaction of a non-rolling tire and a rolling tire can be illustrated by the following two-dimensional schematics in Figure 2.1. As shown in Figure 2.1b, unlike the flat tire contact patch in the tire on-road dynamics, the tire-soil contact patch consists of a flattened portion AB, a curved portion BC at the front of the tire, and a curved portion AD at the rear of the tire.

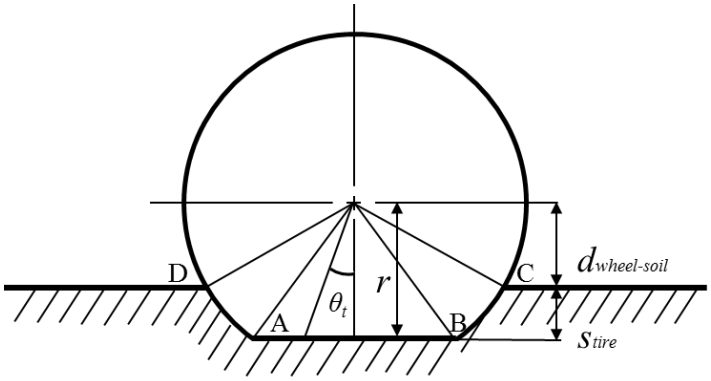

(a) A non-rolling tire on soil

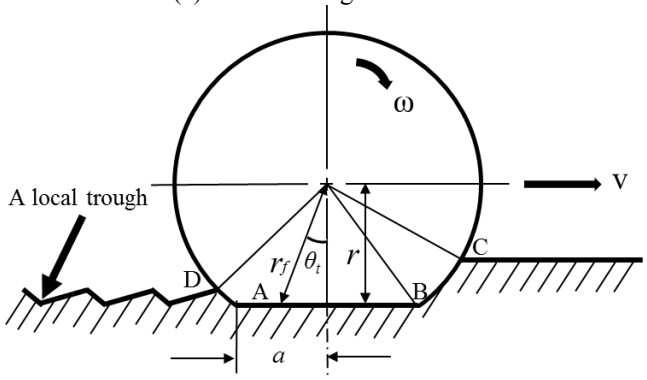

(b) A rolling tire on soil a rolling tire on soil

Figure 2.1: Schematics of tire-soil interaction.

A rut is formed to the left of the point D (for the tire moving to the right, as indicated in Figure 2.1b), and rut depth, also named the plastic deformation of soil or residual sinkage in some literature [15], [16], is defined as the vertical distance between the rut bottom (after the traffic) and the rut bottom's original undisturbed surface (before the traffic).

Sinkage is defined as the vertical displacement from its original position (before the traffic) experienced by the soil when the soil is subjected to pressure (during the traffic) from some pressure source, e.g., a tire, a wheel, etc. The sinkage due to the normal load of the pressure source is named static sinkage, and the sinkage due to the slip between the pressure source and the terrain is named slip sinkage.

The sinkage of a tire (tire sinkage) is defined as the sinkage at the lowest point on the tire-soil contact patch, and when the slip velocity at that lowest point is non-zero; the tire sinkage comprises static sinkage and slip sinkage. At the same point of soil, the sinkage is larger than the rut depth because of the elastic rebound of the soil upon unloading and the shear displacement of soil. The elastic rebound could be negligibly small if the soil shows more plastic behavior, such as for dry and sandy soil [14]. When the slip ratio increases past a certain level, the rut bottom becomes very wavy, as described in Section 4.5.2, and can no longer be considered flat as it has sometimes been illustrated by the simplified schematics in the literature [14], [13], [17].

Effective rolling radius, also referred to as effective tire radius [18], effective radius, or rolling radius [19] in other literature, is defined as the quotient of the longitudinal speed (forward speed) of wheel center divided by the angular speed of wheel revolution [20]. The definition of effective rolling radius works for the traction mode, towing mode, and braking mode of the tire. In this paper, rolling radius is the effective rolling radius of a tire on soil under the free-rolling condition i.e., zero driving and braking torque [14]. The rolling radius is a special case of effective rolling radius and shall not be confused with effective rolling radius[21]. The self-propelled condition, i.e., zero drawbar pull, is also named to be the free roll or free-rolling condition in some literature [22], [21], while in some other literature [14], [23], the free roll or free-rolling condition is defined the same as the towing condition, i.e., zero driving and braking torque. In this dissertation, the free-rolling condition differs from the self-propelled condition and equals the towing condition.

The slip ratio defined in this paper is a function of the longitudinal velocity at the axle of the wheel V_x, the angular speed of the wheel ω_w, and the rolling radius r_0 [14], as shown by Equation (2.1). Equation (2.1) indicates that the slip ratio is zero for a tire under free-rolling

condition on the test soil. Note that in Section 5.2.3 – 5.2.4, the zero slip ratio is not defined under the free-rolling condition but is defined under the self-propelled condition on the test soil, i.e., zero drawbar pull, in agreement with one of the zero conditions defined in [22].

$$s = \left(1 - \frac{V_x}{r_0 \omega_w}\right) \times 100\% \qquad 2.1$$

When a tire is moving on soil in the traction mode, i.e., driving torque is larger than zero, there are two types of longitudinal forces developed in the tire-soil contact patch, gross tractive force and motion resistance, sometimes named rolling resistance [16]. The latter is the sum of external motion resistance and the internal motion resistance. The internal motion resistance is due to the energy dissipation in the hysteresis of tire material [14]. The external motion resistance comprises compaction resistance and bulldozing resistance. The gross tractive force is a longitudinal force converted from the axle torque [22]. The gross tractive force minus the internal motion resistance gives tractive force [24]. The tractive force, sometimes named tractive effort [14] or thrust force [25], can be determined by integrating the horizontal component of shear stress over the tire-soil contact patch [24]. Drawbar pull (DP), occasionally referred to as net traction, is defined as the gross tractive force minus the motion resistance force [26]. Drawbar pull coefficient (DPC), or tractive coefficient [27], is simply the ratio of the DP over the dynamic tire normal load (tire normal load). The dynamic tire normal load can vary from the static tire normal load due to a change in tire loaded radius and weight transfer effect.

Soil compaction can be characterized by multiple parameters such as bulk density, void ratio, air permeability, etc. [28] The bulk density has been frequently used in previous research as the single parameter to quantify soil compaction. In this study, bulk density is also chosen to quantify soil compaction. Also, per Section 5.1, bulk density can be related to the CI and water content. For this reason, in this study, the CI and water content are also chosen to quantify soil compaction.

2.2 Experimental Tests in the Study of Tire-Soil Interaction

The study of tire-soil interaction largely relies on experimental tests such as soil tests, tire-soil tests, and tire tests in a few cases as these tests can be conducted to assess tire off-road performance, determine soil parameters and other parameters of interest, and validate or parameterize different models of interest. In the study of tire-soil interaction, soil tests are mostly related to the soil condition characterization. The tire-soil tests are most relevant to the study of tire off-road tractive performance which is the major topic of this dissertation and an important branch of the tire-soil interaction study. This section briefly introduces various types of soil tests and tire-soil tests and the parameters measured in them.

2.2.1 Soil Condition Characterization and Soil Tests

In the study of tire-soil interaction, the soil condition needs to be characterized, from perspectives of typical soil properties such as soil texture classification, soil water content, soil compaction, and soil shearing property, commonly by soil parameters such as soil texture (gradation or particle size distribution), cone index (CI), remolding index (RI), dry bulk density (bulk density), water content, soil friction angle, and soil cohesion. In the soil test and tire-soil test, proper soil parameters need to be evaluated for the test soil such that the soil condition is characterized sufficiently, and this will also facilitate research result comparison or help researchers who wants to repeat the same test.

As for the soil texture, cone index, bulk density and water content, direct measurement can be made by performing soil tests specified by specific standards, e.g., ASTM or ISO standards for particle size distribution [29], [30], [31], [32]; ASAE standard for CI [33]; SAE standard about the remolding test for the measurement of CI and RI [34]; ASTM standard for bulk density [35]; and ASTM standards for water content [36], [37], [38].

A penetration test must be done to determine the CI. In the penetration test, a static cone penetrometer directly measures the CI; yet, manually maintaining a constant penetration speed to form a static penetration can be challenging [39]. Alternatively, a dynamic cone penetrometer indirectly measures the CI by relating it to the penetration distance of the cone

[40].

Soil friction angle and soil cohesion are related through the Mohr-Coulomb equation Equation (2.2), and multiple types of shear test can be run to determine these two parameters; the most common type of shear test is the triaxial compression test. Depending on the texture classification of the test soil and the kind of shearing being studied, a proper type of shear test needs to be chosen. For example, the vane shear test is only suitable for clays that are purely cohesive, i.e., friction angle is zero [41]. In studies of horizontal shearing, the vane shear test is not preferable, because the soil cohesion obtained is for vertical shearing and cannot be generally considered equal to the soil cohesion for the horizontal shearing [23]. As an alternative method to evaluate the soil friction angle and the soil cohesion, the penetration test with a dynamic cone penetrometer could be carried out based on empirical relationships established by Russian researchers [42]. Tests for the evaluation of soil friction angle and soil cohesion are also discussed in Section 2.3.2

$$\tau_{\max} = c + \sigma \tan\phi \qquad 2.2$$

In the SAE standard about off-road vehicle mobility evaluation [34], a sufficient soil condition characterization requires evaluation of the aforementioned soil parameters plus parameters of the pressure-sinkage and shear stress-shear displacement relationship. The tests necessary for the evaluation of the parameters of the pressure-sinkage and shear stress-shear displacement relationship are discussed in Section 2.3.2.

2.2.2 Tire-Soil Tests and Parameters or Relationships of Interest

A tire moving on soft soil could operate in towing mode (also referred to as pure rolling mode), traction mode (also referred to as driving mode), or braking mode [43], [23]. Dynamic tire-soil (DTS) tests were completed previously either in fields (field DTS tests) or in labs (lab DTS tests) to study the tire off-road performance in the towing mode [44], [45], in the traction mode [46], [47], [48], and in the braking mode [49]. The lab DTS tests are usually conducted in a soil bin that contains the test soil, while the field DTS tests are performed outdoor on natural terrains. In the lab DTS tests, the soil can be well prepared in the soil bin

to achieve the objective soil compaction level and soil moisture level. By contrast, in field DTS tests, there could be more uncontrollable uncertainties in preparing the test soil, and hence it could be more difficult than in DTS tests to repeat the objective soil condition. However, in lab DTS tests, the usually used soil bin imposes a space limit which renders the range of test tire longitudinal speed low, while, in field DTS tests, space limit is not generally deemed a restriction. The instrumentation of test facilities used in the laboratory and field tire-soil tests and the parameters that these test facilities can measure are summarized in Table 2.1 – Table 2.4

Table 2.1: Instrumentation of test facilities and parameters that can be measured for the laboratory dynamic tire-soil tests, part 1.

Test Facilities	Sensors	Measured Parameters
The dynamometer with a small soil bin and two large soil bins, Land Locomotion Laboratory [50]	Sensing part of the Dynamometer	Drawbar pull, input wheel/sprocket torque, slip and soil sinkage
Terramechanics rig, Virginia Tech	Kistler P650 Wheel Hub Sensor	The 3 wheel forces and 3 wheel moments, wheel angular speed and displacement
UPM indoor tire traction testing facility, University Putra Malaysia [51]	Strain gage typed load cells	Drawbar pull and vertical wheel forces
	ONO SOKKI MP-981 encoder	Wheel longitudinal speed
	ONO SOKKI MP-981 encoder	Wheel revolution speed
	KYOWA DT 100A displacement transducer	Tire sinkage
Traction research vehicle (TRV), USDA-ARS National Soil Dynamics Lab [52]	Torque transducer	Input wheel torque
	3 load cells	Vertical wheel force
	Load cells	Drawbar pull
All-terrain vehicle (ATV) tire single wheel machine, USDA-ARS National Soil Dynamics Lab[52]	Potentiometer	Vertical position of the test machine outer frame
	6 load cells	Longitudinal, vertical, and lateral tire forces
Indoor traction measurement system, Kyoto University [53]	Octagonal ring transducer	Drawbar pull
	Linear potentiometer	Tire sinkage
	Rotary encoder	Wheel revolution angle
	Strain gauge	Driving torque
	Rotary encoder	Longitudinal wheel displacement

Table 2.2: Instrumentation of test facilities and parameters that can be measured for the laboratory dynamic tire-soil tests, part 2.

Test Facilities	Sensors	Measured Parameters
Tire traction testing facility, Junagadh Agricultural University [54]	Ring transducer	Drawbar pull
	Torque transducer	Input wheel torque
	Electric platform balance	Static vertical wheel force
	Load cells	Drawbar pull and vertical wheel force
Indoor traction measurement system, Urmia University, Iran [55]	Optic tachometer	Wheel longitudinal speed
	Encoder	Wheel revolution speed
	Not specified	Tire sinkage
Indoor tire testing facility, IIT Kharagpur [56]	Extended octagonal ring transducer	Lateral wheel force
	Dynograph recorder	Drawbar pull
	LVDT	Tire deflection
Single wheel tester, Agricultural Engineering Research Institute (AERI), Iran [57]	Load cell	Vertical wheel force
Single tire and track loading apparatus, Off-Road Dynamics Research Laboratory, Cranfield University [58]	A fifth wheel and digital encoder	Wheel/sprocket longitudinal speed
	Digital encoder mounted on the wheel	Wheel/sprocket revolution speed
	Talcum powder line and drawstring transducer	Soil displacement

Table 2.3: Instrumentation of test facilities and parameters that can be measured for the field dynamic tire-soil tests, part 1.

Test Facilities	Sensors	Measured Parameters
In-situ tire test rig, University of Tehran [59]	4 S-beam load cells	Lateral and longitudinal wheel force, input wheel torque, and self-aligning torque
	Opto-counter	Wheel longitudinal speed
	Velocity transducer	Wheel revolution speed
	Strain gauged torque tube	Input wheel torque
NIAE Mk II single wheel tester [60]	Strain gauge	Drawbar pull
Single Wheel Testing Device, UDESC – SC [61]	Tacho-generators	Wheel longitudinal and revolution speed
	Not mentioned	Drawbar pull, wheel torque and wheel revolution speed

Single Wheel Traction Testing Machine, University of California, Davis (Upadhyaya et al., 1986)	Forward speed sensor	Wheel longitudinal speed
	Wheel RPM sensor	Wheel revolution speed,
	Load cell for vertical and draft loads	Drawbar pull, vertical wheel forces
	Torque transducers	Wheel input torque
	Front depth gage	Elevation of the undeformed surface,
	Axle height gage	Axle height
	Rear depth gage	Elevation of deformed surface

Table 2.4: Instrumentation of test facilities and parameters that can be measured for the field dynamic tire-soil tests, part 2.

Test Facilities	Sensors	Measured Parameters
Single wheel tester, Hohenheim University [62]	Piezoelectric force transducer	Wheel forces and wheel torques
Instrumented Vehicle for Off-road Dynamics Testing, Lublin Institute of Technology [63]	Rotating wheel dynamometer	Three wheel forces and three wheel moments
	Datron CORREVIT sensor	Vehicle longitudinal speed
Cold Regions Research and Engineering Laboratory's (CRREL's) instrumented vehicle (CIV) [64]	Triaxial load cell	Vertical, lateral, and longitudinal wheel force
	Velocity sensors	Wheel revolution speed
	Linear motion potentiometer	Turning angles
	Motion pack sensor	Vehicle accelerations
	Fifth wheel tachometer	Vehicle longitudinal speed
Portable Tire Test Trailer, Intelligent Transport Laboratory, Virginia Tech [65]	Kistler's 6-axis force/torque transducer	3 wheel forces and 3 wheel moments
Large tire testing trailer, Vehicle Dynamics Group, University of Pretoria [66]	Wheel force transducers	Wheel force and wheel moments
Single wheel tester, Off-Road Dynamics Research Laboratory, Cranfield University [58]	Not mentioned	Torque, slip, load, and speed

From Table 2.1 to Table 2.4, it's clear that most test facilities are capable of measuring wheel forces and wheel moments, and some of them are also capable of measuring the wheel input torque. The reason is that the data of these measurements can be used to calculate the drawbar pull, drawbar coefficient, or drawbar efficiency (tractive efficiency) which are the parameters commonly used to characterize the tire tractive performance in off-road conditions.

A few of the test facilities listed in Table 2.1, Table 2.2, Table 2.3, and Table 2.4 also can measure the soil deformation parameters (soil response parameters) such as tire sinkage or soil displacement. Apart from using the sensors listed in the tables above, other alternative methods to measure the soil response parameters have been developed in the past decade. Soil sinkage was measured in lab DTS tests by using Wireless Internal Tire Sensors (WITS), a string potentiometer, and an ultrasonic sensor. WITS was mainly composed of eight optical sensors and an accelerometer, and they were installed around the wheel circumference [48]. Image processing technique was utilized to measure soil sinkage in lab DTS tests [67] and rut depth in field DTS tests [15]. In both measurement methods developed by Naranjo et al. and Guthrie et al., two groups of sensors or cameras were placed respectively in front of and behind the moving tire such that the undisturbed soil and the rut formed after traffic were measured, and another group of sensors or cameras were mounted inside the body of tire to measure the tire loaded radius.

Aside from tractive performance parameters and soil response parameters which are related to the geometry of the tire-soil interaction interface (tire-soil contact patch), the other parameters of interest in the dynamic tire-soil tests include the pressure distribution and stress in the tire-soil contact patch. Attaching miniature pressure transducers to the surface of tire tread and lug could measure the normal stress of the points in the tire-soil contact patch [68], and attaching three-axial force transducers in a similar way to the tire could measure the normal stress, the tangential stress and the lateral stress of the points in the tire-soil contact patch [69], [70]. The three-directional contact stress data measured this way can approximate the three dimensional stress distribution in the tire-soil contact patch, i.e., the stress as a function of both the angular position and the lateral position of points in the contact patch, if an adequate number of transducers are mounted in the lateral direction so as to cover the entire tire-soil contact patch during the tire rotation.

Pressure-sinkage relationship and shear stress-shear displacement relationship are also the concerns in the tire-soil interaction study, measurement methods for the parameters involved in these relationships are discussed in Section 2.3.2.

2.3 Tire Off-Road Traction Dynamics

An important aspect of tire-soil interaction is the tire off-road traction dynamics, as it is closely related to the acceleration performance and fuel economy of off-road vehicle and the soil compaction of the terrain where the tire traverses. Drawbar pull (DP), drawbar pull coefficient (DPC), and drawbar efficiency (DE) are three commonly used parameters to characterize tire off-road tractive performance.

2.3.1 Modeling Approaches

The tire off-road traction modeling was attempted in previous literature mainly by empirical approaches [71], [46], semi-empirical approaches [13], [49], theoretical approaches [24], and numerical approaches [72], [73], [74], [75]. It's worth mentioning that the boundary between the first three aforementioned approaches is not uniquely and strictly defined; in some theoretical approach, a few empirical relationships could exist; some model, claimed to be semi-empirical by its developer, is defined to be empirical in this dissertation.

2.3.1.1 Empirical Approach

The empirical approach is purely based on the data collected from tire tests, soil tests, or tire-soil tests, and the data determines the mathematical form of models.

Using the DP measurements from field dynamic tire-soil tests (DTS tests), Wismer and Luth modeled the DPC of a tire moving on the soft soil as an empirical function of wheel numeric and slip ratio, per Equation (2.3). This empirical model captured the soil condition by using the cone index (CI) as an independent variable of the wheel numeric Equation (2.4) [71].

$$DPC = 0.75\left(1-\exp(-0.3C_n s)\right)-\left(\frac{1.2}{C_n}+0.04\right) \qquad 2.3$$

$$C_n = \frac{CI \cdot d \cdot b_t}{F_z} \tag{2.4}$$

Upadhyaya et al. conducted field DTS tests with the single wheel tester as described in [76], and the DP measurements from the tests were found to fit an empirical DPC model Equation (2.5) that didn't take any soil parameter as an independent variable or model parameter [77]. Model parameterization results of the Upadhyaya et al. empirical DPC model showed that empirical model parameters varied between different soil conditions given the same tire under the same tire normal load [77], [46]. This demonstrates the influence of soil condition on the DPC while such influence cannot be reflected by the Upadhyaya et al. empirical DPC model [77].

$$DPC = u_1\left(1 - \exp(-u_2 s)\right) \tag{2.5}$$

Later, the Upadhyaya et al. empirical DPC model was refined to account for the influence of cone index and gravimetric water content by setting the model parameters as functions of the cone index and gravimetric water content, Equations (2.6) – (2.7), but the regression analysis to compute the coefficients for these soil parameters didn't yield desirable results [78].

$$u_1 = 0.311 + 0.067\frac{b_t}{2a} + 0.001\frac{CI}{p_i} + 1.089\theta_g - 0.933\frac{CI}{p_i} \cdot \left(\frac{F_z}{CI \cdot b_t \cdot 2a}\right)^2 \tag{2.6}$$

$$\begin{aligned}\frac{1}{u_2} = {} & -5.376 - 0.764\frac{u_1 F_z}{2a} + 4.923\frac{b_t}{2a} - 211.152\frac{F_z}{CI \cdot b_t \cdot 2a} \cdot \theta_g \\ & + 101\frac{u_1}{2a} \cdot \frac{F_z}{CI \cdot b_t \cdot 2a} + 32.6446\theta_g + 30.913u_1\end{aligned} \tag{2.7}$$

To obtain better regression results, the model parameters of the Upadhyaya et al. empirical DPC model were related to the model parameters of the empirical Janosi and Hanamoto shear stress-displacement model, Equations (2.8) – (2.9) [79], from which improvements were made by relating the model parameters of the Upadhyaya et al. empirical DPC model also to the model parameters of the Reece pressure-sinkage model, Equations (2.10) – (2.11) [80].

$$u_1 F_z = 6.675 + 0.952 A_c \tau_{\max} - 19.208 \tau_{\max} K_s b_t \qquad 2.8$$

$$\frac{1}{u_2} = -4.682 + 413.067 \left(u_1 \frac{\bar{p}}{\tau_{\max}} \cdot \frac{K_s}{2a} \right) + 41.377 \frac{u_1 F_z}{K_t \cdot 2a} \qquad 2.9$$

$$u_1 F_z = 1.73 + 0.572 A_c \tau_{\max} + 3.589 \tau_{\max} K_s b_t + 5.672 \frac{\bar{p}}{k_r} \qquad 2.10$$

$$u_1 u_2 F_z = 0.881 \left(\frac{r_f - r}{2a} \right)^{0.183} \left(\frac{S_{tire} + r_f - r}{2a} \right)^{1.346} \left(\frac{b_t}{K_s} \right)^{-1.717} \left(\frac{2a}{K_s} \right)^{1.713} \left(\frac{2ab_t}{A_c} \right)^{4.198} \left(\tau_{\max} A_c \right)^{0.685} \qquad 2.11$$

Like the Upadhyaya et al. empirical DPC model, another empirical model that can be used to characterize the steady-state DP-slip relationship is the Magic Formula tire model (MFTM) [81]. Because of the MFTM's empirical nature, the data about tire force vs. slip collected from dynamic tire tests is always required for the model parameterization. Optimization needs to be performed to the test data in order to evaluate the set of the model parameters for the MFTM that has the desirable fit to the test data. Several methods have been proposed to perform the optimization for the parameterization of the MFTM [82], [83], [84].

Although the MFTM was originally proposed for tire on-road dynamics [81], [85], attempts have been made to extend the use of the MFTM to tire off-road dynamics [7], [8]. Pauwelussen and Laib parameterized the MFTM using the test data about DP vs. slip for two farm tires on sandy soil [7]. Besides, the model parameters of the MFTM were correlated with tire normal load, soil cohesion, and soil friction angle, as shown by Equatons (2.12) – (2.14), by equating the semi-empirical tractive force model proposed in [86] and the MFTM [7].

$$B \cdot C \cdot D = \left(c \cdot \alpha_1 \cdot F_z^{\alpha_2} + F_z \cdot \tan\phi \right) \left(1 + \alpha_3 F_z^{\alpha_4} \right) \qquad 2.12$$

$$D \cdot \sin(C \cdot \arctan B) = \left(c \cdot \alpha_1 \cdot F_z^{\alpha_2} + F_z \cdot \tan \phi \right) \quad 2.13$$

$$\frac{B \cdot C \cdot D \cos(C \cdot \arctan B)}{1 + B^2} = \left(c \cdot \alpha_1 \cdot F_z^{\alpha_2} + F_z \cdot \tan \phi \right) \exp(-\alpha_3 F_z^{\alpha_4}) \quad 2.14$$

For cohesive soil, such as clay, the model parameters of the MFTM were established to be functions of a clay-tire numeric, Equations (2.15) – (2.18), and the MFTM was used to compute the drawbar pull coefficient [8].

$$N_{CM} = \frac{CI \cdot b_t^{0.9} \cdot d^{0.65} \cdot \delta^{0.45}}{F_z} \quad 2.15$$

$$D = 0.73 - \frac{2.1}{N_{CM} + 2.18} \quad 2.16$$

$$S_v = 0.15 + \frac{0.71}{N_{CM} - 0.78} \quad 2.17$$

$$BCD = 3.63 \log_{10}(N_{CM}) + 0.47 \quad 2.18$$

2.3.1.2 Semi-empirical Approach

The semi-empirical approach basically applies some of the empirical pressure-sinkage models and the empirical shear-displacement models, and combine these empirical models, soil mechanics models and tire mechanics models to compute the DPC, DP, or DE of a tire on soft soil. Basically, the horizontal component of the shear stress and the horizontal

component of the pressure (radial stress) are integrated over the tire-soil contact patch to calculate gross tractive force (assuming the internal motion resistance is negligible) and compaction resistance respectively. If the bulldozing force is neglected, DP can be obtained by subtract the compaction resistance from the gross tractive force.

Shumlevich and Osetinsky developed a semi-empirical tire off-road traction model, performed field DTS tests, and validated the Shumlevich and Osetinsky traction model in both traction mode and braking mode by using the test data collected [49]. The core part of the Shumlevich and Osetinsky traction model was to model the tire-soil contact patch contour as a parabola, per Equation (2.19). The Janosi and Hanamoto shear stress-shear displacement model and Bekker's pressure-sinkage model were applied in the Shumlevich and Osetinsky traction model.

$$z_c = d_{rut} - \zeta_1 x_c^2 \tag{2.19}$$

Senatore and Sandu proposed a semi-empirical steady state tire model that took the slip sinkage effect and multi-pass effect into account when computing the DP [13]; experimental tests remained to be performed to validate this semi-empirical model and to determine the model parameters of this semi-empirical model. The slip sinkage effect was considered by setting slip ratio as an independent variable for the sinkage exponent, per Equation (2.20). Equations (2.21) – (2.22) account for the influence of multi-pass on soil shear parameters. The geometry of the tire-soil contact patch and the radial stress distribution in the tire-soil contact patch were portrayed by the Chan and Sandu model [17] and the Wong and Reece model [87] respectively.

$$n = n_0 + n_1 s \tag{2.20}$$

$$c_n = c\left\{1 + \left[1 - \exp\left(\frac{-s_0}{\beta_1}\right)\right]\beta_2 + \beta_3 n_p\right\} \tag{2.21}$$

$$K_{sn} = K_s \left\{ 1 + \left[1 - \exp\left(\frac{-s_0}{\beta_1}\right) \right] \beta_2 + \beta_3 n_p \right\} \quad 2.22$$

2.3.1.3 Theoretical Approach

The theoretical approach adopts purely theoretical pressure-sinkage and shear stress-displacement models.

Take the theoretical performance analytical (TPA) model for example [24], the Load-Sinkage Analytical (LSA) model [42] Equation (2.23), was used in an integral over contact patch to calculate compaction resistance, and the Pokrovski's analytical shear stress-displacement model [24] Equation (2.24), was used in another integral to calculate tractive force.

$$p = \frac{1}{\frac{D_1}{B_i} + \frac{D_2}{E_Y z} \omega \cdot b \cdot \xi} \quad 2.23$$

$$\tau = \left[G_1 \exp\left(-G_2 j\right) + G_3 \right] \times \left[1 - \exp\left(-G_4 j\right) \right] \quad 2.24$$

The model parameters of Equation (2.23), D_1, D_2, B_i, ω, ξ are related to the soil cohesion, soil friction angle, soil bulk density, hardpan depth, and Young's modulus [42], and the model parameters of Equation (2.24), G_1, G_2, G_3, G_4 can be related to the contact ground pressure, soil cohesion and soil friction angle [24]. Lyasko claimed that the model parameters of the TPA model are invariant soil parameters, and their values don't depend on the shape and size of the plates used in pressure-sinkage tests and shear tests for the model parameterization [24]; this could be an advantage over some semi-empirical models based on the Bekker pressure-sinkage model (Bekker model), as the soil parameters of the Bekker model were found to vary with the plate shape and size [88], [89]. Lyasko also claimed the TPA model works for vehicles with tires; however, details about the geometry and stress-distribution of the tire-soil contact patch were not provided in [24].

2.3.1.4 Numerical Approach

In the numerical approach, such as the finite element method (FEM) and the discrete element method (DEM), the soil is discretized and treated as a set of continuum-based finite elements or as a group of circular, elliptical, spherical, or ellipsoidal elements; the tire can be modelled as a FEM tire model [75], [90] or a lumped-masses model [72], [73]. In the study of tire off-road traction, the DEM is applied mostly to model frictional soil, such as sand; the FEM has been applied to both frictional soil and cohesive soil [91].

In the FEM to model the tire and soil behavior in tire-soil interaction, a soil constitutive model is needed to characterize the elastic behavior and hardening/softening plastic soil behavior in the stress-strain scope under various loading conditions. A lot of soil constitutive models have been proposed, and they are reviewed in [92], [91]; the most commonly used soil constitutive models in the study of the tire-soil interaction are the modified Drucker-Prager model with a cap [93] and the modified Cam-Clay model [94]; Mohr-Coulomb model has also been utilized in the earlier studies [95], [96], [97], in some of which the visco-plastic stress-strain model was attempted [97]. These elastoplastic models are already implemented in ABAQUS with a user-friendly interface [98]; several researchers ran simulations of a tire running on the deformable soil in ABAQUS [99], [100], [101], [102].

It is worth noting that the soil constitutive models assume the soil to be modeled is a continuum, and even though the soil constitutive models have been implemented to predict the large soil deformation [74], [101], [103], they are still reported to have limitations in predicting the significant soil flow that can happen when the slip ratio of the tire on the soil is high [1]. Also, in most of the study of tire-soil interaction where the FEM was applied, the shear stress in the tire-soil contact interface is modeled by the Coulomb frictional law that doesn't depend on the slip ratio; the inability to account for the influence of the slip ratio on the contact shear stress can result in the inaccuracy of drawbar pull and tire sinkage prediction.

In the DEM, the main soil model is the contact model that applies the spring-damper mechanism, with the damping being either viscous damping or Coulomb damping, to compute the contact force/moment between two elements or between an element and a tire.

Ideally, the contact force can be tensile because any soil presents at least a slight cohesion effect [104]. However, it is found that the cohesion effect was ignored in some previous research as a part of simplification of DEM modelling. Simplification of DEM modelling also includes ignoring contact moments and setting zero damping, and how the simplification of DEM modelling is done depends on the type of soil to be modeled and the constraint of computing power.

Both FEM and DEM are featured with a high computational cost and not ready to be incorporated into the multibody dynamics software for real-time simulation; to get over these shortcomings, Madsen et al. discretized a tire and soil and developed a numerical tire off-road traction model which was used in multi-body dynamics environment and achieved near real-time off-road vehicle dynamics simulation [72], [73]. In the Madsen et al. model, theoretical soil mechanics models that respectively characterize the vertical load-sinkage relationship, horizontal load-vertical stress relationship, and bulldozing force-deformation relationship, together with the semi-empirical Janosi and Hanamoto shear stress-shear displacement model, were used to compute the tire drawbar pull and soil deformation [73].

2.3.2 Relationships of Interest, Model Parameters, and Model Parameterization

Compared with soil physical property parameters and soil mechanics parameters, cone index-related soil parameters are more commonly selected as model inputs of empirical tire off-road traction models to characterize the soil condition [24]; the cone index-related soil parameters can be evaluated by using cone penetrometers.

The pressure-sinkage relationship, the shear stress-shear displacement relationship, the pressure distribution (radial stress distribution) in the tire-soil contact patch, and the geometry of the tire-soil contact patch could be the four most important features to be considered in theoretically or semi-empirically modeling tire off-road traction.

Multiple pressure-sinkage models and several shear stress-shear displacement models were developed in previous literature and were summarized in [10]; only some empirical and semi-empirical models of them, such as the Bekker's model Equation (2.25), the Reece's

model Equaton (2.26), and the Janosi and Hanamoto model Equation (2.27), with relatively simpler mathematical forms, were incorporated into the semi-empirical tire off-road traction models as described in [80], [49], [13], [14].

$$p = \left(\frac{k_c}{b} + k_\phi \right) z^n \tag{2.25}$$

$$p = \left(c k_c' + \gamma k_\phi' b \right) \left(\frac{z}{b} \right)^n \tag{2.26}$$

$$\tau = \tau_{\max} \left[1 - \exp\left(-j / K_s \right) \right] \tag{2.27}$$

The pressure distribution in the tire-soil contact patch is affected by tire features, tire normal load, tire inflation pressure, soil conditions, and slip ratio [105], [14]. Few attempts were made to model the pressure distribution in the tire-soil contact patch; a uniform or parabolic pressure distribution was often assumed in modeling the off-road traction of agricultural tires. Schjønning et al. proposed an empirical pressure-distribution model with the ratio of actual tire inflation pressure to the tire inflation pressure recommended by the tire manufacturer being a model input [106]; this model didn't account for the influence of slip ratio on the location of the maximum pressure in the contact patch. In contrast, the radial stress distribution model, originally proposed for the wheel-soil interaction [87], considers the influence of slip ratio; this model was used occasionally with slight adaptation in the semi-empirical tire off-road traction model developed by [13].

$$p(\theta_w) = \begin{cases} \left(k_1 + k_2 b_w \right) \left(\frac{r_w}{b_w} \right)^n \left(\cos\theta_w - \cos\theta_{w1} \right)^n & \left(\theta_{wm} \le \theta_w < \theta_{w1} \right) \\ \left(k_1 + k_2 b_w \right) \left(\frac{r_w}{b_w} \right)^n \left\{ \cos\left[\theta_{w1} - \left(\frac{\theta_w - \theta_{w2}}{\theta_{wm} - \theta_{w2}} \right) \left(\theta_{w1} - \theta_{wm} \right) \right] - \cos\theta_{w1} \right\}^n & \left(\theta_{w2} < \theta_w \le \theta_{wm} \right) \end{cases} \tag{2.28}$$

Also in semi-empirically modeling tire off-road traction, the bulldozing effect may need to be considered in the calculation of the external motion resistance [14], possibly because

there could be bulldozing force in the curved portion of the tire-soil contact patch. The force associated with the bulldozing effect can be computed by using the Terzaghi's bearing capacity equation Equation (2.29) [13].

$$p = cN_c\lambda_c + \frac{B_T}{2}\gamma N_\gamma \lambda_\gamma + \gamma N_q \lambda_q z \qquad 2.29$$

Unlike the typical semi-empirical approach per Section 2.3.1.2, in the numerical approach to model tire off-road traction, the pressure-sinkage relationship is not directly modelled; instead, the soil stress-strain relationship (in the FEM) or the contact force-relative velocity/distance relationship between the elements or between the element and tire tread (in the DEM) are directly modeled.

The parameterization of the aforementioned terramechanics models and soil models (the calibration of the model parameters) in Section 2.3 is essentially obtaining values of soil mechanics parameters, such as soil cohesion, soil friction angle, Poisson's ratio, Young's modulus, etc.; and values of some other model parameters, some of which are empirical parameters. These model parameters, unlike soil physical properties parameters, cannot be directly measured. The evaluation of these model parameters relies on some tire-soil or soil tests and the measurement data of model outputs, model inputs, and other variables that can be related to these parameters from these tests.

If these parameters are purely about the soil alone and not associated with the running gears or other tools that interact with the soil, e.g., soil cohesion, soil friction angle, Poisson's ratio, Young's modulus, the traditional test methods of soil mechanics such as the triaxial compression test, the isotropic compression test, the direct shear test, etc., can be conducted to evaluate these parameters. The model parameterization for most soil constitutive models relies on the lab soil tests such as the tri-axial compression test and the one-dimensional compression test [91]. However, the soil sampled in the lab soil tests might not resemble the natural soil. Due to that, Field soil tests were performed to determine the soil parameters of the soil constitutive model [107]; in the field test, the soil is less disturbed from its natural status than in the lab soil test. To determine the micro-mechanical parameters of the contact

model in the DEM, an optimization program need to be run; in the optimization program, the micro-mechanical parameters are tuned so as to produce the DEM simulation result close to the soil mechanics test result [108], [109], [110] or the plate-sinkage test [104], [111]. As introduced earlier, the DEM simulation is computational expensive. To reduce the total time spent in running the optimization program, some assumption will be established, e.g., the contact stiffness in tangential direction was assumed to be the same as that in normal direction [104].

If the model parameter to be evaluated is associated with the running gear or other tools that interact with the soil, such as the empirical model parameters of the pressure-sinkage models and of the shear stress-shear displacement models and the coefficient of friction between tire and soil, the plate-sinkage test, the shear test using shear plates, or the tire-soil test must be carried out. In the FEM, the well-known Coulomb friction model is widely used to compute the shear stress in the tire-soil contact patch; however in most cases, the coefficient of friction was assigned a value that didn't have valid experiment basis [112], [113], [114].

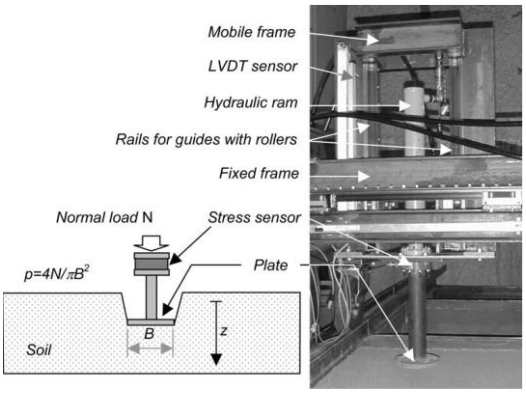

Figure 2.2: Plate-sinkage test (source from Gotteland and Benoit, 2006 [115]**, Figure 1; reprinted with permission from Elsevier).**

For those tire off-road traction models that were proposed based on the pressure-sinkage model and shear stress-shear displacement model, the tire off-road traction model parameterization includes the parameterization of the pressure-sinkage model and shear stress-shear displacement model, some of which was done by using the data of variation in pressure with sinkage and the data of variation in shear stress with shear displacement from the plate-sinkage tests and shear tests respectively [116], [1], [17].

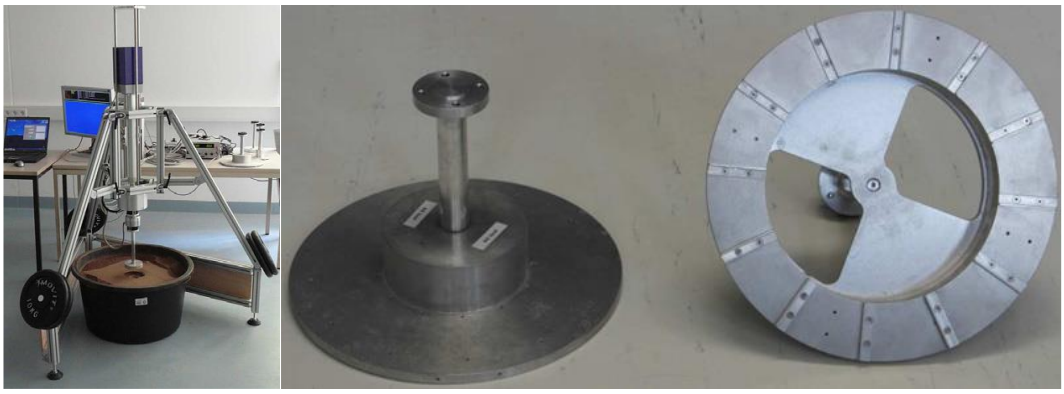

(a) Bevameter and annular shear plates for the plate-shear test (source from Apfelbeck et al., 2011 [88], Figure 2 and Figure 10; reprinted with permission from Elsevier).

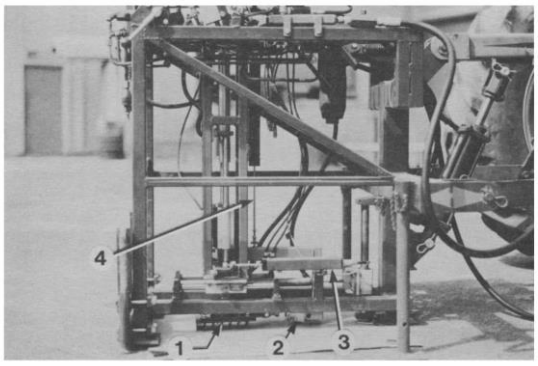

(b) Rectangular shear plate for the plate-shear test (source from Upadhyaya et al., 1993 [117], Figure 4; reprinted with permission from Elsevier).

Figure 2.3: Plate-shear tests.

However, in these plate-sinkage tests and shear tests, it was not a tire but a plate or a rectangular or annular shear plate being used as the tool to interact with soil; this way, the interaction of the tool with the soil in the tests cannot represent the realistic tire-soil interaction [118]. The tire-soil test can be a promising test method to parameterize the pressure-sinkage model and shear stress-shear displacement model used in tire off-road traction dynamics modeling, although it has not found its use in the previous publication like that. Nevertheless, field DTS tests found their use in the parameterization of some empirical tire off-road traction models that are independent of the pressure-sinkage model and the shear stress-shear displacement model [77]. Although Plackett pointed out that the plate-soil interaction could not represent the realistic tire-soil interaction [118], parameter values of the pressure-sinkage model and shear stress-shear displacement model, obtained by performing the plate-sinkage tests and shear tests using shear plates, were used in modeling tire off-road performance.

2.4 Effect of Tire Inflation Pressure

Tire inflation pressure is an influencing factor for both of the tire off-road performance and soil compaction, and it has been investigated in DTS tests mostly for tractor tires.

The combined influence of tire inflation pressure and tire normal load on rut depth, rut width, the cone index in the tire tracks, the length of the tire-soil contact patch, and the pressure of a few points on the lug was studied in field DTS tests for a Goodyear 16.9R38 R-l agricultural tractor tire [68] and a Goodyear 18.4 R38 Dyna Torque Radial (2 star) R-l agricultural tractor tire [119], [120] on sandy loam and clay loam. The field DTS tests were run at a constant slip ratio. In the field DTS tests for the latter tractor tire, the influence of tire inflation pressure on net traction and tractive efficiency at a constant slip ratio was also investigated [120].

In lab DTS tests to study tire rolling resistance, it was found that an increase in tire inflation pressure led to a decrease in rolling resistance of a Goodyear 9.5L-14, 6 radial ply tire on clay loam, and such influence of tire inflation pressure became larger as tire normal load increased [45], while Elwaleed et al. observed that a decrease in inflation pressure of a Bridgestone 5-12, 4 ply, lug M tractor tire from its recommended value, 221 kPa, to 193 kPa, and to 166 kPa resulted in a decrease and next an increase in motion resistance on sandy clay loam [121].

The test results of the field DTS tests done in the past at multiple levels of slip ratio indicate that lowering tire inflation pressure could improve or hardly influence tire off-road traction, depending on the tire design and soil condition. The influence of longitudinal velocity and inflation pressure on traction coefficient and traction efficiency at various levels of slip ratio up to 100% was studied in field DTS tests for a 13.6-28 6PR bias-ply tractor tire on concrete field, the rotary cultivated field of sandy loam, and the paddy fields of sandy loam and loamy sand with stubble. From the test results it was concluded that a reduction in the tire inflation pressure improved tractive performance considerably on the paddy field with stubble but not significantly on the first two types of test field [27].

Extensive field DTS tests had been conducted using the University of California, Davis

(UCD) single wheel traction tester. Wulfsohn et al. tested four tractor tires on a well-tilled Yolo loam soil at two levels of inflation pressure and three levels of tire normal load, and found that the change between two levels of tire inflation pressure didn't affect the off-road tractive performance [122]. Bashford et al. tested 18.4R42 and 18.4R16 tractor tires on a wheat stubble surface and a plowed surface of Sharksburg silty loam at three levels of tire inflation pressure, and drew a conclusion that better off-road tractive performance was achieved on the wheat stubble surface for both tires with lower inflation pressure and on the plowed surface for only the 18.4R42 tire with lower inflation pressure [123].

Several tire models in the tire on-road or off-road dynamics take tire inflation pressure as a model input. In the tire on-road dynamics, TNO MF-TYRE 6.1 Magic Formula equations take the influence of tire inflation pressure into account; some of their model parameters are functions of the tire inflation pressure [124]. Höpping et al. found that the TNO MF-TYRE 6.1 Magic Formula equations can only achieve desirable accuracy for small variations in tire inflation pressure; to accurately model the dynamics of a tire with large variations in tire inflation pressure, second order polynomials were introduced to describe the tire normal load and inflation pressure dependencies of the Magic Formula model parameters [125]. Apart from the Magic Formula, another element of Short Wavelength Intermediate Frequency Tyre (SWIFT) model that accounts for the tire inflation pressure changes and models tire enveloping behavior is the tandem-cam model [126].

In the tire off-road dynamics, some semi-empirical tire models account for the pressure-sinkage relationship and the pressure distribution in the tire-soil contact patch; the latter is influenced by the tire inflation pressure [105]. Therefore, although these tire models don't set the tire inflation pressure as a model input, they implicitly consider the tire inflation pressure changes; the compaction resistance model for pneumatic tires presented in [14] and the empirical DPC model in [79] are both examples. The Senatore and Sandu tire model and the Upadhyaya et al. semi-empirical DPC model both have the tire inflation pressure as a model input; the former needs the tire inflation pressure to determine the location of the maximum normal stress [13], and the latter has one model parameter written as a function of the tire inflation pressure [78].

It was found that in no existing literature, the Magic Formula tire model was extended for large inflation pressure changes and tire off-road traction by using the test data from dynamic tire-soil tests.

Chapter 3

Experimental Setup

This chapter includes materials from [11] *by R. He, C. Sandu, and J. E. Osorio, with the permission from Elsevier, and the agreement attached.*

The tools and apparatus used in the test program (described in Chapter 4) include the Terramechanics Rig, the Tekscan® pressure mapping system, a cone penetrometer, a water content sensor, a soil sampling kit, and other miscellaneous tools. This chapter elaborates on these tools and apparatus in terms of their specifications and their use in the tests and soil preparation.

3.1 Tools and Apparatus

The main test facility in the test program was the Terramechanics Rig (T-Rig) at the Terramechanics, Multibody, and Vehicle Systems (TMVS) Laboratory of Virginia Tech, as it can be seen from Figure 3.1. After being mounted onto the carriage of the T-Rig, the test tire can spin at a preset constant revolution speed, under the actuation of a motor (the wheel motor). A separate motor (the carriage motor) powers the translation of the carriage along the soil bin (or the longitudinal movement of the tire), via a belt drive system, at a constant longitudinal speed of 6 cm/s. Under this motion control setup, the slip control of the tire was achieved by varying the revolution speed of the wheel motor that powered the tire spin. Tire normal load was applied by a pair of air springs and dynamically controlled around a preset value by using a PID controller. The control signal was sent to an Enfield M1d proportional valve that regulated the mass flow of the air going into the air springs. A KISTLER P650 force hub measured the three wheel forces and three wheel moments at a sampling frequency of 160 Hz. More details about the function and instrumentation of the T-Rig can be found in [127], [128].

Figure 3.1: Terramechanics Rig before November 2017, at the TMVS Lab, Virginia Tech.

Before November 2017, the test tire mounted on the Terramechanics rig could not move in towing mode; the motor torque always transmitted to the wheel/tire. Because of that, tire rolling radius, defined in the free rolling condition as the zero condition, could not be measured directly. That's why estimation of the tire rolling radius was performed, as described in Section 4.4.1, to calculate slip ratios in the laboratory dynamic tire-soil tests conducted before November 2017. Since November 2017, a clutch, mounted between the wheel motor and the wheel shaft, had been incorporated into the Terramechanics Rig, enabling the separation of wheel torque from the wheel and hence the free-rolling of a tire.

(a) Tire-wheel-shaft-clutch assembly. (b) zoom-in view of the clutch.

Figure 3.2: Assembly of tire, wheel, shaft, and clutch of the Terramechanics Rig after November 2017. The clutch is disengaged; the teeth are separated.

A Tekscan® pressure mapping system was utilized to measure and record the pressure distribution in the tire contact patch. The main component of this system was a Tekscan® 3150 pressure pad that consists of pressure sensors that are called sensel. The value of the maximum pressure this pressure pad can measure is 862 kPa. The pressure pad has 2288 sensels totally, with its spatial resolution being 1.4 sensels per square centimeter [129]. Before use, the pressure pad underwent equilibration and calibration. The equilibration ensured all the sensel readings were almost the same when a uniform load was applied onto the pressure pad. After the equilibration was done, the calibration was carried out to guarantee the force reading of the pressure pad would be as close to the real value of the tire normal load as possible. During the static tire deflection test, the pressure pad was placed inside a protective case; otherwise, the pressure pad would be in contact with the tire; when the normal load was increased gradually to the preset value, the damage induced by shear would occur to the pressure pad as a consequence of the carcass deformation.

In the test program, the test soil in the soil bin needed to be sampled, and the measurements of bulk density, gravimetric water content (GWC), volumetric water content (VWC), and CI needed to be taken for the test soil. A soil sampling kit was utilized to sample the soil from the soil bin. The soil sampling kit consisted of an aluminum soil core sampler, shown in Figure 3.3 with a 10.08 cm height and a 185.15 cm^3 inner volume, two aluminum lids, a scoop, and a dead blow hammer. To start the soil sampling, the sampler was tapped into soil by the dead blow hammer such that the soil just completely surrounded the sampler. The scoop of the soil sampling kit was used to remove the soil around the sampler, the top and bottom of the sampler were lidded, and the sampler containing the soil was taken away at the end of sampling.

Gravimetric water content was measured by following the steps prescribed in the ASTM standards [37]. Immediately after the soil was sampled, the soil mass was measured; with the volume of the sampler known, wet density was calculated. Next, the soil was dried to a constant mass; the final constant mass was measured. The difference in the soil mass, from the moment before drying the soil to the moment the soil was dried to a constant mass, was calculated. An AMIR digital scale of 500 grams load capacity, 0.01 grams resolution, and 0.01 grams accuracy was used to measure mass. Drying the soil was performed in a

microwave oven with 600 W maximum power and vented chambers. With the wet density, the final constant mass, and the mass difference obtained, bulk density and gravimetric water content of the sample soil were calculated.

(a) Sampler was immersed in the soil.

(b) Soil around the sampler was removed by a scoop.

(c) Sampler was sealed by lids.

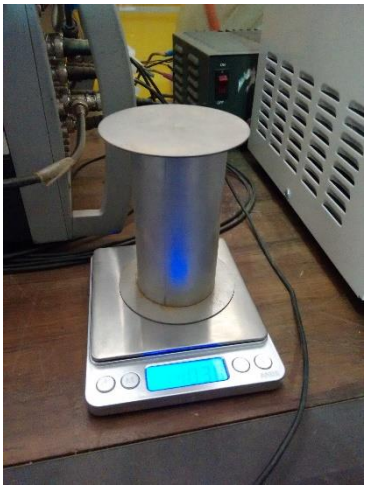

(d) Sampler was taken out of the test soil and weighed.

Figure 3.3: Soil sampling kit and its use.

Volumetric water content was measured by using the Campbell Scientific HS2P volumetric water content probe [130]. It comprises a pair of 12 cm dielectric water content sensor rods that can measure the average volumetric water content of the soil in contact with the 12 cm sensor rods. During the measurement of VWC, the sensor rods were vertically inserted into the soil. The measurement accuracy and the measurement resolution of this

VWC probe are 3% and 0.05%, respectively.

Cone index was measured using a Humboldt HS-4210 Digital Static Cone Penetrometer [131]. During operation, the Digital Static Cone Penetrometer (DSCP) was pressed in a way such that the cone penetrated vertically and slowly into the soil. The penetration of the DSCP proceeded until 12 cm penetration depth was reached, and the DSCP measured the penetration resistance force and recorded the maximum penetration resistance force of the whole penetration process. The cone index was obtained by dividing the maximum penetration force by the cone base area [14]. The base area of the HS-4210 DSCP is 1.5 cm^2, and the resolution of the penetration resistance force measurement is 4.45 N (1 lbf).

Distance measurement were taken by using a set of rulers or a Bosch GLM 15 Compact Laser Measure. When using the laser measure between an object and the test soil, e.g., measuring the tire loaded radius in the static tire-soil tests, a piece of paper was placed on the soil for better laser reflection and hence a more accurate measurement, as shown in Figure 3.4.

Figure 3.4: Laser measure being used between the tire and soil.

Record of the rut (the footprint on the soil) boundary resorted to a piece or pieces of 12'' by 12'', 0.007'' thick, super light plastic sheet. Marker pen drew the boundary of what was vertically projected onto the plastic sheet, as depicted in Figure 3.5. The set of rulers and plastic sheets that worked in or on the rut were deliberately chosen to be light and operated carefully to avoid as much as possible disturbing the soil, measures that aimed to keep the

rut intact.

Figure 3.5: Use of two conjunct pieces of plastic sheet to record the rut boundary.

3.2 Soil Preparation Method

The soil preparation was completed in the soil bin from the soil surface to a depth of around 15 cm (15 cm is the maximum value of the soil depth for the soil of interest in this study, as it will be explained later in Section 4.5.1) in some tests of the test program; the flat soil track resulted from the soil preparation had a soil depth larger than 30 cm. The objective of the soil preparation is to achieve the soil condition of interest; a similar soil condition is expected to be realized after going through the same soil preparation steps.

There were four main steps of the soil preparation method: shoveling, tilling, leveling, and compacting. During the first step, a shovel was used to render soil failure to the soil. Coming to the second step, an electric tiller was used to till the soil, with the purpose of eliminating the soil lumps and ensuring the loosest state of the soil. As for the third step, a leveler was dragged by the carriage moving from the rear end to the front end of the soil bin to create a flat soil track, as shown in the Figure 3.6c. In the fourth step, a roller was compacting the soil. The roller was dragged by the carriage from the front end of the rig to the rear end, and then back to the front end, thus finishing one trip of compacting. Also, the water content of the test soil in the soil bin of the T-rig could not be maintained at any level higher than the low level [127]; therefore, before the four main steps, the soil was left at its

driest condition, which is another important part of the soil preparation method, to ensure the water content in one test is re-achievable.

In the tire-soil tests or soil tests, it's challenging and yet important to sufficiently characterize the soil condition of the test soil, because the soil can be highly non-homogeneous, and insufficient characterization of soil condition might result in difficulty or impossibility in comparing the test results with others. It's also challenging yet important to control the soil condition of the test soil given that the relevant technology is not mature enough to be cost-effective for lab use, and failure in controlling the soil condition might render test results skewed.

(a)

(b)

(c)

(d)

Figure 3.6: Soil after: (a) the shoveling; (b) the tilling; (c) the leveling; (d) the compacting of the soil preparation method.

The soil preparation method adopted in this study facilitates controlling the test soil condition and, together with taking measurements of the soil parameters per Section 4.2.1, 4.4.2, and 4.5.1, contributes to the sufficient characterization of the test soil condition.

Chapter 4

Test Program

This chapter includes materials from [11] *by R. He, C. Sandu, and J. E. Osorio, with the permission from Elsevier, and the agreement attached.*

The indoor evaluation of tire performance on soil and on rigid surface, soil response, and soil condition was conducted with the experimental setup described in Chapter 3 at the TMVS laboratory of Virginia Tech. The tests involved in the test program, i.e., the laboratory soil properties tests, the static tire deflection tests, the static tire-soil tests, and the dynamic tire-soil tests, were performed from November 2016 to November 2017 and from June 2019 to November 2019, and the details of these tests, including the relationships between the tests, test procedures, and test results, are presented in this chapter.

4.1 Test Program Overview

Different tests were completed in the test program of this study, and the connection between these tests is introduced in this section. The tests completed in the test program and their relationship are summarized in Figure 4.1.

All the tests of the test program were carried out in lab. In the static tire-soil tests (STS test) and the dynamic tire-soil tests, the test soil was placed inside a soil bin and prepared following the steps described in Section 3.2, while in the laboratory soil properties tests, the test soil was not prepared. The test tire was tested on the flat surface of the steel U channels in the static deflection tests. The values of the rolling radius estimated in the laboratory static tire-soil tests of July 2017 were used to set nominal slip ratios in some of the laboratory dynamic tire-soil tests before the Terramechanics Rig had the capability of measuring the rolling radius directly (only since November 2017).

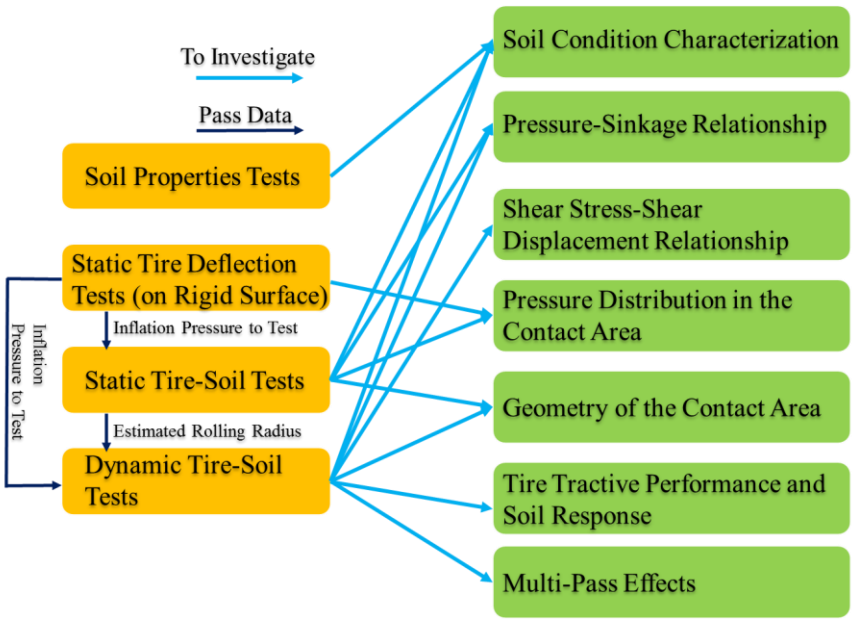

Figure 4.1: Relationship of the tests performed in the test program.

The tire used throughout the test program was a 225/60R16 97S Uniroyal (Michelin) Standard Reference Test Tire (the SRTT). As for the tire parameters of the test tire, the tire width is 225 mm, the tire unloaded radius is 338.2 mm, the tread depth is 7 mm, and the unloaded section height is 135 mm.

(a) SRTT used in all the tests of the test program.

(b) Pirelli used in the static tire-soil tests for the rut reconstruction.

Figure 4.2: Test tires in the test program.

Another tire tested, only in the static tire-soil tests for the rut reconstruction, is a 235/55

R19 105V M+S Pirelli Scorpion Verde all season tire (the Pirelli). As the basic parameters of this tire, the tire width is 235 mm, the tire unloaded radius is 370.55 mm, the tread depth is 8.7 mm, and the unloaded section height is 129.25 mm.

The soil tested in the test program was the same loamy sand as the one tested by Naranjo [127]. Its textural compositions and some of its physical properties are listed in Table 4.1.

Table 4.1: Physical properties of the test soil.

Soil type (USDA classification)	Clay [g.g-1] < 0.002 mm	Silt [g.g-1] 0.002 – 0.05 mm	Sand [g.g-1] 0.05 – 2 mm	Maximum bulk density [g/cm^3][a]
Loamy sand	0	16%	84%	1.93

[a] The maximum bulk density was obtained by the standard proctor test specified by ASTM [132]

4.2 Laboratory Soil Properties Test

In order to determine some of the soil properties of the test soil, the laboratory soil properties test (lab SP test) was performed. Although there are various soil properties and each of them can be characterized by several parameters, only an adequate number of soil parameters considered related to tire off-road tractive performance were chosen to be measured in the lab SP test. Bulk density reflects the soil compaction which influences the compaction resistance of a tire [14]. Water content, related to soil porosity, is reported to influence the shear stress-shear displacement relationship of soils and hence influence the tractive force of tire [1], [127]. Cone index is a soil mechanical property parameter that has been commonly used in experimental tire-soil or vehicle-soil studies and selected as a model input of some empirical models to assess off-road vehicle mobility [133]. Therefore, the soil parameters chosen to be measured in the lab SP test were bulk density, cone index, and gravimetric water content. In this section, the procedures and the results of the lab SP test are explained one after another.

4.2.1 Procedures of Laboratory Soil Properties Test

In the lab SP test, a spot of soil in the soil bin was chosen to be sampled, and measurements

of CI were taken at that spot by using the DSCP. The sampler was pushed gently and slowly into the soil by using the dead weight blow hammer included in the soil sampling kit. Next, four measurements of the CI were taken at locations very close to the merged sampler by using the DSCP (as described in Section 3.2) such that the CI of the soil inside the sampler could be approximated by the mean of the four CI measurements. Figure 4.3 illustrates the locations where the sampler was tapped inside the soil and the CI was measured at the chosen spot. Following the steps explained in Section 3.1, the sampler containing the soil was taken away, and the gravimetric water content and bulk density of the sampled soil were measured. The procedures of the lab SP test as described above were repeated until soil at a sufficiently wide range of soil compaction was tested.

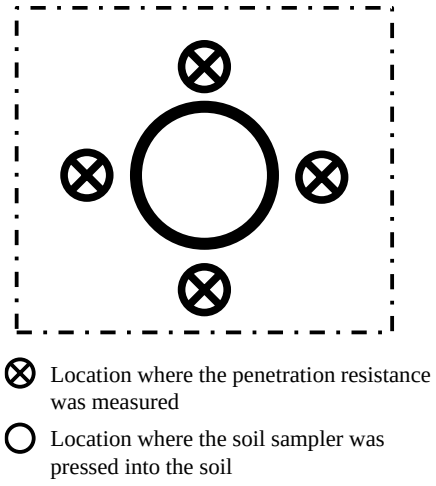

Figure 4.3: Schematic of the locations for the measurements of the CI and the merged sampler.

4.2.2 Results of Laboratory Soil Properties Tests

The measurements of the CI, the GWC, and bulk density from the lab SP tests are tabulated below. While the gravimetric water content of the test soil always remained to be very low, the CI of the test soil ranged widely from 326 kPa to 1631 kPa. The relative compaction varied from 89% to 97%. A general trend could be found that a large increase in the cone index, i.e., from a few hundred to over a thousand, results in an increase in relative compaction, which means the cone index value could reflect the soil compaction. The water content of the test soil in the soil bin of the T-rig could not be maintained at any level higher

than the low level [127]. To ensure the same level of soil water content in the static tire-soil tests and another same level of soil water content in the dynamic tire-soil tests (these two levels are close and low, as will be discussed in Section 4.5.1), the test soil was deliberately left at its driest condition, which accounts for the small values of the GWC in Table 4.2.

Table 4.2: Some soil physical and mechanical properties of the test soil in various soil conditions

Sample No.	Cone index [kPa]	Gravimetric water content [g/g]	Dry bulk density [g/cm^3]	Relative compaction [g.cm^{-3}.g^{-1}.cm^3][a]
1	518.959	0.519%	1.720	89.28%
2	822.921	0.447%	1.735	90.03%
3	326.203	0.604%	1.728	89.68%
4	1631.015	0.964%	1.870	97.02%
5	363.271	0.756%	1.771	91.90%
6	1238.088	0.991%	1.817	94.31%
7	1193.606	0.382%	1.846	95.80%
8	748.784	0.443%	1.793	93.07%
9	810.565	0.643%	1.756	91.11%
10	733.957	0.622%	1.745	90.56%
11	1289.984	0.404%	1.856	96.32%

[a] The relative compaction is the ratio of the dry bulk density over the maximum bulk density (see Table 4.1).

4.3 Static Tire Deflection Test

In the static tire deflection tests, the tire inflation pressure varied, and at each value of the tire inflation pressure, the normal load applied to the tire was increased gradually to a specified value and maintained at that value, after which the test tire could be considered statically loaded. This section introduces the procedures of the static tire deflection test first. Next, the results of the static tire deflection tests are presented, with the analysis completed to the test results from two aspects, variation in loaded radius with tire inflation pressure and variation in contact patch with tire inflation pressure and normal load.

4.3.1 Procedures of Static Tire Deflection Test

As for the static tire deflection tests conducted in November of 2016, the test levels of tire inflation pressure and normal load are displayed in Table 4.3. To start each test, the test tire was either inflated or deflated to the preset tire inflation level. Next, the normal load was

applied gradually to 5 kN, the only normal load level shown in Table 4.3. Thereafter, the measurements of loaded radius and the pressure distribution in the contact patch were taken and recorded, followed by releasing the normal load applied to the tire, which marked the end of each test. The same procedures were repeated three times for each of the ten combinations of the normal load level and the inflation pressure level.

Table 4.3: Design of experiment for the static tire deflection tests in November of 2016.

Operational parameters	Levels
Normal load [kN]	5
Tire inflation pressure [psi]/[kPa]	15/103, 18/124, 21/145, 24/165, 27/186, 30/207, 33/228, 36/248, 39/269, 42/290

(a) In the tests of November 2016. (b) In the tests of August 2019.

Figure 4.4: Pressure pad and rigid surface.

The measurement of loaded radius was accomplished by using a Bosch GLM 15 Compact Laser Measure and a retractable ruler. For each of the three tests at the same combination of the normal load level and the inflation pressure level, those two devices were utilized to measure the distance between the wheel center and the surface of the protective case containing the pressure pad shown in Figure 4.4, and this distance was taken as the loaded radius.

The measurement of the pressure distribution was completed and recorded by using the

Tekscan® pressure mapping system in accordance with the steps per Section 3.1. The measurement data were presented in the format of pressure maps, as shown in Figure 4.5, and each pressure map displays the average of the results from around 60 frames' measurements which took about 1 – 2 minutes.

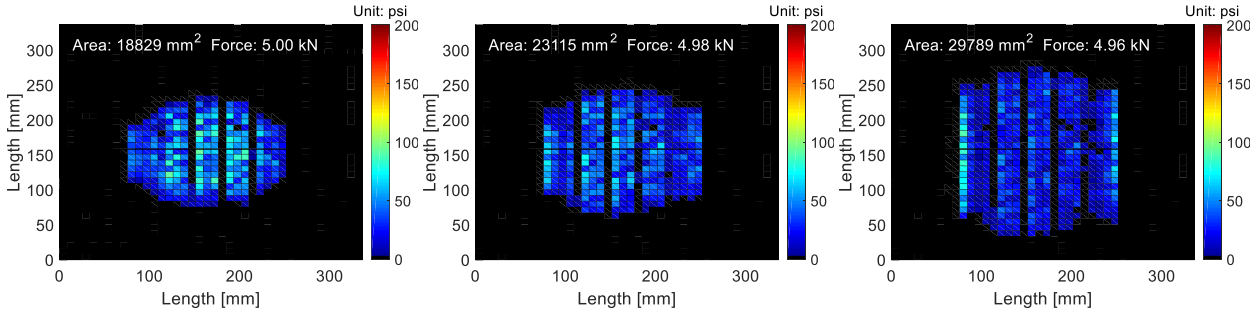

(a) 42 psi inflation pressure, 5 kN normal load.

(b) 30 psi inflation pressure, 5 kN normal load.

(c) 18 psi inflation pressure, 5 kN normal load.

Figure 4.5: Pressure map samples from the static tire deflection tests in November of 2016.

Later in 2019, with the Tekscan® pressure mapping system refurbished (a new 3150 pressure pad was purchased; software was upgraded), additional static tire deflection tests were completed to investigate the effect of normal load on the pressure distribution in the contact patch between a tire and rigid surface. The procedures of the tests were only different from that of the tests conducted in 2016 in three aspects: The normal load applied had three levels, 5 kN, 6 kN, and 7 kN, while the tire inflation pressure level was reduced to be six, ranging from 12 psi to 42 psi at an interval of 6 psi, as listed in Table 4.4; the loaded radius was not measured in each test; each of the combinations of the normal load level and inflation pressure level had two runs of tests instead of three. Tests at the 5 kN normal load and some inflation pressure levels, as listed in Table 4.3, was re-conducted in August 2019 because the pressure pad was a new one, although of the same model no., different from the one used in November 2016.

Table 4.4: Design of experiment for the static tire deflection tests in August of 2019.

Operational parameters	Levels
Normal load [kN]	5, 6, 7
Tire inflation pressure [psi]/[kPa]	12/82, 18/124, 24/165, 30/207, 36/248, 42/290

4.3.2 Results of Static Tire Deflection Tests

4.3.2.1 Loaded Radius (on Rigid Ground)

The three readings of the loaded radius by the laser measure and by the retractable ruler, from the three tests at the same tire inflation pressure level, were averaged respectively and then tabulated in the 2nd and 3rd column of Table 4.5. With the values of the unloaded radius r_f, the unloaded section height h_f, and the tread depth d_{tr} already known, the mean value of the 2nd and 3rd column were taken as the value of the loaded radius r and substituted into Equation (4.1) to calculate the percent radial deflection ρ_p.

$$\rho_p = \frac{r_f - r}{h_f - d_{tr}} \tag{4.1}$$

Table 4.5: Measurements of loaded radius and their resultant values of percent radial deflection. The measured data is from static tire deflection tests in November of 2016.

Tire inflation pressure [psi]	Loaded radius [mm]		Percent radial deflection
	Average retractable ruler reading	Average Bosch laser measure reading	
15	296.0	295.2	33.29%
18	299.8	299.7	30.04%
21	303.7	303.5	27.04%
24	307.0	307.0	24.38%
27	310.0	310.2	21.97%
30	312.2	312.3	20.27%
33	315.0	314.3	18.39%
36	316.2	315.8	17.34%
39	317.3	316.8	16.50%
42	319.0	319.0	15.00%

It can be found from Table 4.5 that 18 psi, 30 psi, and 42 psi resulted in 30%, 20% and 15% radial deflection respectively. These three values of tire inflation pressure were picked as the values of the tire inflation pressure to be tested in the lab STS test and the lab DTS test, as they led to relatively low, medium, and high radial deflection. Also, an observation can be made from Table 4.5: when the tire inflation pressure is larger than 27 psi, every time the inflation pressure is reduced by 3 psi, the percent radial deflection will increase by less than 2%. However, when the inflation pressure is lower than 27 psi, the tire deflection will

increase by a value larger than 2% and mostly around 3% every time the inflation pressure is reduced by 3 psi.

4.3.2.2 Pressure Distribution in the Contact Patch (on Rigid Ground)

The pressure maps in Figure 4.5 display some vertical black stripes that correspond to the grooves of the tire tread pattern where there was zero pressure and no tire-ground contact. Among these three pressure maps in Figure 4.5, as the inflation pressure decreases, the width of the contact patch remains unchanged while the length of the contact patch increases. Another observation worth mentioning is about the distribution of the cyan area that stands for the relatively high pressure. At 42 psi tire inflation pressure, the relatively high pressure area is primarily around the center of the contact patch. By contrast, at tire inflation pressure as low as 18 psi, the relatively high pressure area is distributed on the left and right rims of the contact patch. In addition, the acceptable repeatability of the sensel pressure measurement might be demonstrated by Figure 4.6 where the standard deviation of the three pressure readings from the three tests at the same tire inflation pressure is calculated and plotted for all the sensels in the contact patch. Most values of the standard deviation are smaller than 1.5 psi. Comparing 1.5 psi with the magnitude of the test tire inflation pressure 15 – 42 psi and assuming that the pressure distribution in the contact patch remained the same for all 3 runs, the repeatability of the pressure measurement could be found acceptable for most sensels of the pressure pad.

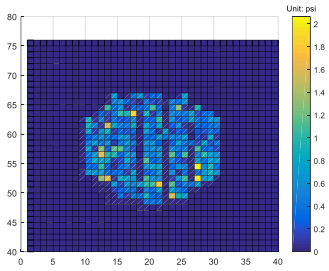

(a) 42 psi inflation pressure, 5 kN normal load

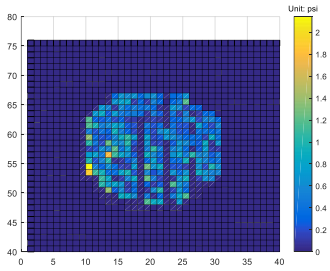

(b) 39 psi inflation pressure, 5 kN normal load

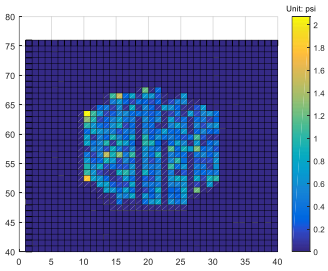

(c) 36 psi inflation pressure, 5 kN normal load

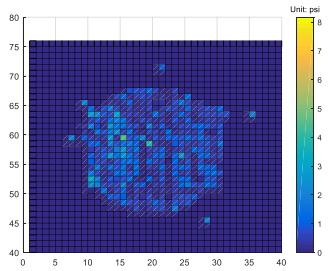

(d) 33 psi inflation pressure, 5 kN normal load

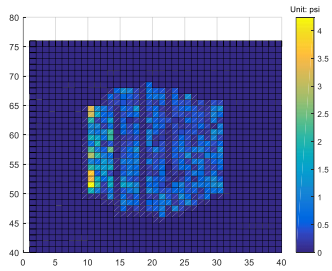

(e) 30 psi inflation pressure, 5 kN normal load

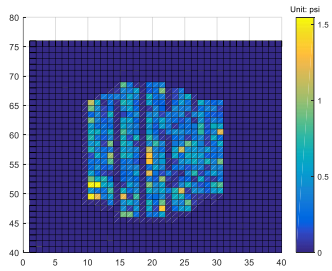

(f) 27 psi inflation pressure, 5 kN normal load

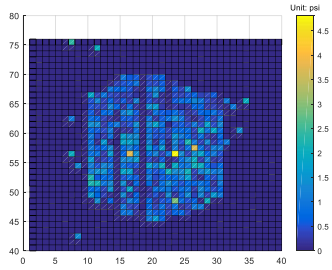

(g) 24 psi inflation pressure, 5 kN normal load

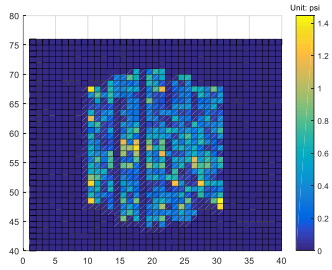

(h) 21 psi inflation pressure, 5 kN normal load

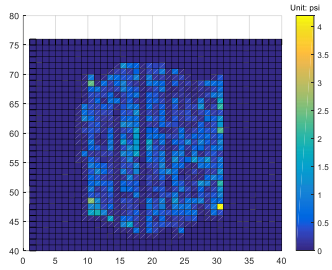

(i) 18 psi inflation pressure, 5 kN normal load

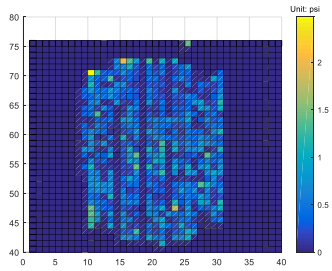

(j) 15 psi inflation pressure, 5 kN normal load

Figure 4.6: Standard deviation of sensel pressure readings for all three static tire deflection tests in November of 2016 with the same test configuration as per Table 4.3.

Tekscan® pressure mapping system recorded the area of contact patch for each pressure map. In Figure 4.5, the area of contact patch is displayed. Three pressure maps, respectively from the three tests done in November of 2016 at each tire inflation pressure level, have three contact patch area values. The average of these values was calculated and plotted against its corresponding tire inflation pressure level at each of the ten test tire inflation pressure levels, as shown by Figure 4.7. Also, the average sensel pressure reading for one pressure map can be calculated by taking the average of all the sensel pressure readings larger than 3 psi (the noise threshold of the Tekscan® 3150 pressure pad) [134] in the contact patch. The average sensel pressure reading is plotted against the tire inflation pressure in Figure 4.8. Figure 4.7 indicates that among the test tire inflation pressure levels, the contact patch area decreases

almost linearly with an increase in the tire inflation pressure. The variation in the average pressure in the contact patch with tire inflation pressure correlates with the findings of Schwanghart [135] in terms of two aspects. First, the average pressure in the contact patch increases linearly with tire inflation pressure. Second, below a certain point, which is (35 psi, 35 psi) in Figure 4.8, the average pressure in the contact patch is larger than the tire inflation pressure, while above that point, the average pressure in the contact patch is smaller than the tire inflation pressure.

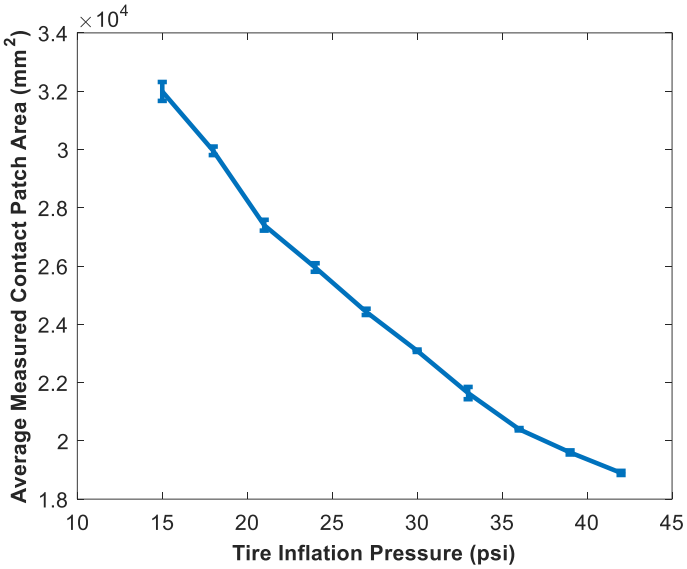

Figure 4.7: Variations of the average measured contact patch area with tire inflation pressure from the tests done in November of 2016.

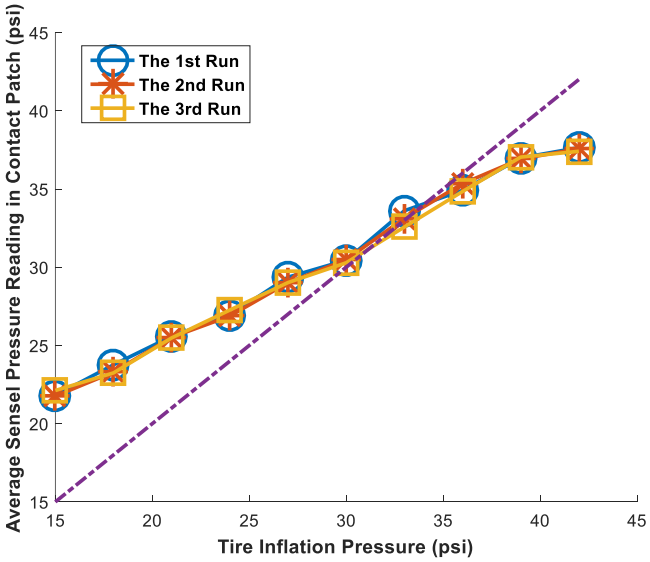

Figure 4.8: Variations of the average sensel pressure in the contact patch with tire inflation pressure from the tests done in November of 2016.

Average sensel pressure reading was obtained for the tests in August of 2019 the same way as that for the tests in November of 2016. Also, average ground pressure was calculated as the ratio of the normal load over the contact patch area. It can be seen from Figure 4.9 that the average sensel pressure reading is nearly the same in value as the average ground pressure.

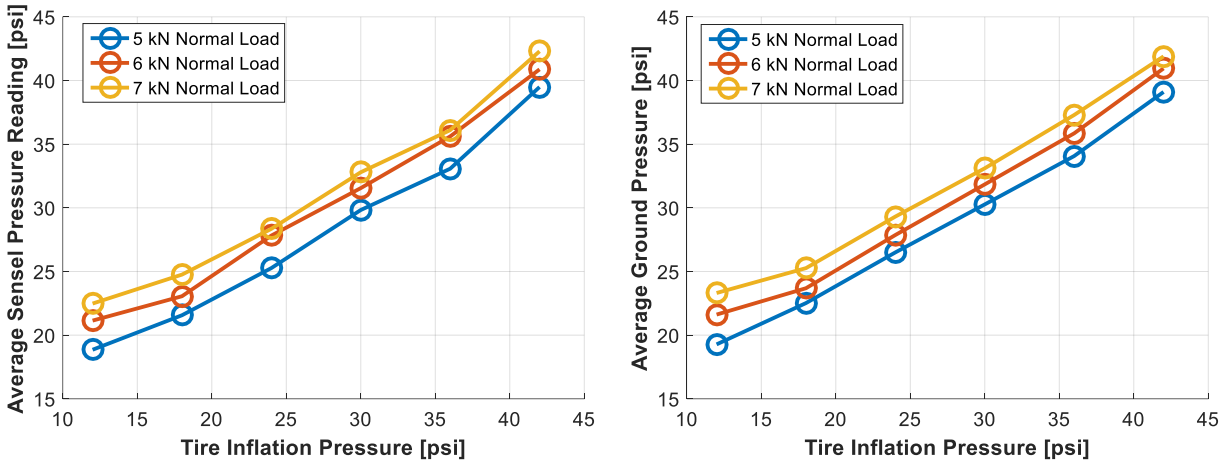

(a) Mean value of all the pressure readings of sensel in the contact patch.

(b) Average ground pressure, obtained by dividing the normal load by the contact patch area.

Figure 4.9: Variation of the average sense pressure readings and average ground pressure with tire inflation pressure and normal load from the tests done in August of 2019.

Comparing Figure 4.9a and Figure 4.8, at 5 kN normal load and at the same inflation pressure, the average sensel reading of the former is within 2 psi different from that of the latter. Such difference is considered acceptable and possibly due to: as previously mentioned, the pressure pad in the tests of 2019 was a brand new one while the pressure in the tests of 2016 was an old one, some sensels of which were blunt in response; also, in the tests of 2019, when the tire was loaded on the ground, the camber was not as perfectly zero as that in the test of 2016.

It's clear from Figure 4.9 that the trend of average sensel pressure reading or average ground pressure w.r.t the inflation pressure remains the same as Figure 4.8. Besides, the increase in average sensel pressure reading or average ground pressure with an increase in

the normal load level, i.e., 1 kN, is far smaller than the increase with an increase in the inflation pressure level, i.e., 6 psi. This might indicate that the tire inflation pressure is more influential than the tire normal load to the average ground pressure.

4.4 Laboratory Static Tire-Soil Test

The static tire-soil tests is divided into two phases: July of 2017 and October of 2019. The aim of the static tire-soil tests in July of 2017 was to estimate the rolling radius of the free-rolling test tire on the test soil at the longitudinal speed of 6 cm/s (the test rig carriage longitudinal speed). The static tire-soil tests in July of 2017 assumed that the loaded radius of a free-rolling tire moving forward at 6 cm/s on soil is the same as the loaded radius of the same non-rolling tire on the same soil in the same physical condition when the free-rolling tire and the non-rolling tire are at the same normal load and tire inflation pressure. Wong pointed out that the vertical tire stiffness decreases with an increase in the longitudinal speed of the tire [14]. However, in the lab DTS tests, 6 cm/s or equivalently 0.216 km/s is a very small value for the longitudinal speed. Therefore, the assumption here for the static tire-soil tests in July of 2017 could be reasonable.

The static tire-soil tests in October of 2019 had two aims. The first aim was to investigate the effect of normal load, inflation pressure, and initial soil condition on the loaded tire radius and rut size parameters. The second aim was to reconstruct 3-D profile of the ruts (footprint) formed by the tire rutting.

In this section, the loaded radius vs. the rolling radius relationship is explained first, then the test procedures of the static tire-soil tests are described, followed by the analysis of the results from the tests.

4.4.1 Loaded Radius and Rolling Radius

With the loaded radius and the unloaded radius of a tire known, the rolling radius of a tire on a rigid flat surface could be evaluated as [18]:

$$r_0 = \frac{\sin\left\{\cos^{-1}\left(\frac{r}{r_f}\right)\right\}}{\cos^{-1}\left(\frac{r}{r_f}\right)} r_f \qquad 4.2$$

Even though the derivation of Equation (4.2) is based on the geometry of the contact patch and the kinematics of a tire when the tire is free rolling on a rigid flat surface, it is found by the author that Equation (4.2) could also work for a free-rolling tire on deformable soil. The derivation of Equation (4.2) for a free-rolling tire on deformable soil is almost identical to the derivation for a tire on a rigid flat surface [18].

For a tire running on the deformable soil, the profile of the tire-soil interaction can be depicted as shown in Figure 4.10 [14].

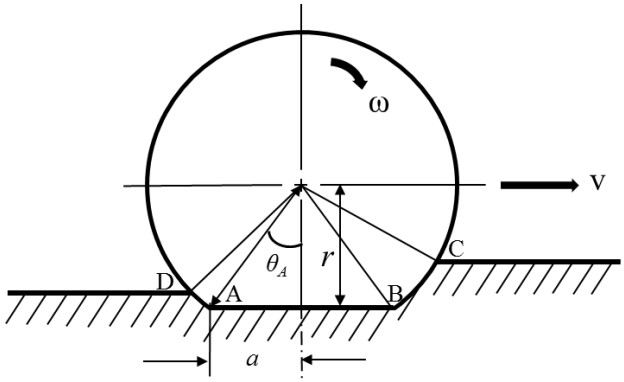

Figure 4.10: Schematic of the tire-soil interaction profile in the towing mode.

When the tire is moving in the free-rolling condition (zero driving or braking torque) on the deformable soil [22], and the wheel center travels by the distance of the contact patch length $2a$, at the same time, the rotational angle of the wheel will be $2\theta_A$, hence bringing up the following two equations:

$$V_x = r_0 \omega_w = \frac{2a}{t} \qquad 4.3$$

$$\omega_w = \frac{2\theta_A}{t} \qquad 4.4$$

Hence

$$r_0 = \frac{a}{\theta_A} \tag{4.5}$$

It is worth mentioning at the case depicted by Figure 4.10 is not restricted to the free rolling of a tire on soil, yet Equations (4.3) – (4.4) both hold for the free-rolling tire on soil. If the tire is not free-rolling on soil, Equation (4.4) will not be valid anymore.

The geometry of the Figure 4.10 indicates:

$$r = r_f \cos\left(\theta_A\right) \tag{4.6}$$

$$a = r_f \sin\left(\theta_A\right) \tag{4.7}$$

Combining Equations (4.5) – (4.7) together, the rolling radius can be expressed as a function of loaded radius and unloaded radius just like Equation (4.2).

Therefore, substituting the value of the loaded radius measured from the lab STS test of July 2017 into Equation (4.2) and assuming the loaded radius of a free-rolling tire on soil can be approximated by the loaded radius of that tire, non-rolling on the same soil, under the same normal load and at the same tire inflation pressure, the rolling radius of the test tire on the same soil at the longitudinal speed of 6 cm/s can be calculated.

4.4.2 Procedures of Laboratory Static Tire-Soil Test

Before the static tire-soil test, soil preparation was completed following the steps described in Section 3.2. To obtain the soil compaction level specified in the design of experiment for the laboratory static tire-soil test, zero trips of compacting (low soil compaction level), two trips (medium soil compaction level), and eight trips (high soil compaction level) were done.

Right before each static tire-soil test, the VWC and CI of the test soil, close to the location

where the contact patch would be formed, were measured three times following the steps as described in Section 3.1 before applying the normal load to the tire. The sequence of taking those measurements was the CI first, then the VWC because inserting the sensor rods of the HS2P into the soil to measure the VWC might change the mechanical property of the soil, and measuring the CI required an intact soil after the soil preparation. Figure 4.11 illustrates the location relative to the contact patch where the CI and VWC were measured. These measurements were not taken at the location of the prospective contact patch because the measurements required penetrations of the measurement device to the soil which would change the soil mechanical property of the prepared soil.

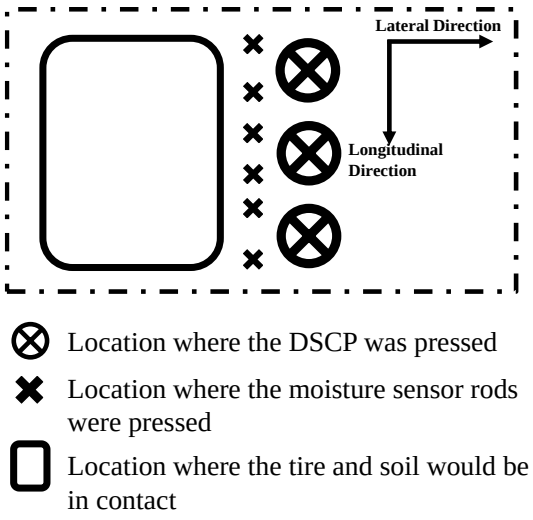

Figure 4.11: Schematic of the location for the measurements of CI and VWC.

The design of experiment (DOE) for the static tire-soil tests in July of 2017 is summarized in Table 4.6. The measurements of the CI and VWC were averaged for each soil compaction level and listed in Table 4.6. Also, as shown in Table 4.6, three tire inflation pressure levels and one normal load level were chosen to be tested in the static tire-soil test, as they resulted in 15%, 20%, and 30% of the percent radial deflection in the static tire deflection test. The average values of CI for the tests at low, medium, and high soil compaction level (zero, two, and eight trips of compacting) were 274.58 kPa, 694.69 kPa and 896.23 kPa as shown in Table 4.6.

Table 4.6: Design of experiment for the laboratory static tire-soil tests in July of 2017.

Operational parameters	Number of levels	Levels
Normal load [kN]	1	5
Tire inflation pressure [psi]/[kPa]	3	18/124, 30/207, 42/290
Soil compaction (CI [kPa], VWC [cm^3/cm^3])	3	(274.58, 1.47%), (694.69, 1.85%), (896.23, 1.88%)

In each static tire-soil test with one test configuration as per Table 4.6, i.e., one level of the normal load, one level of the tire inflation pressure, and one level of the soil compaction, the normal load applied to the tire was slowly increased to 5 kN first, after which the measurement of the distance between the wheel center and the surface of the undisturbed soil was taken by using a Bosch GLM 15 Compact Laser Measure. Next, the normal load was released and the tire was lifted up and moved to the next test location along the soil track. Finally, the rut depth was measured by using the ruler as shown in Figure 4.12, marking the end of the test. Assuming that the elastic rebound of the test soil (sandy and dry soil, as illustrated by Table 4.6 and Table 4.1) after unloading and lifting the tire is negligibly small, as explained in Section 2.1, the values of the rut depth and the distance between the wheel center and the surface of the undisturbed soil were summed up to evaluate the loaded radius of the static tire on the soil, as illustrated by Figure 2.1a. The same procedures as described above were repeated for another two tests with the same test configuration, hence totally 27 tests were performed for all the test configurations of the DOE as per Table 4.6. The average of the three values of the loaded radius that were collected from the three tests at one test configuration was substituted into Equation (4.2), and the rolling radius was obtained at the soil compaction, tire inflation pressure, and normal load specified by that test configuration.

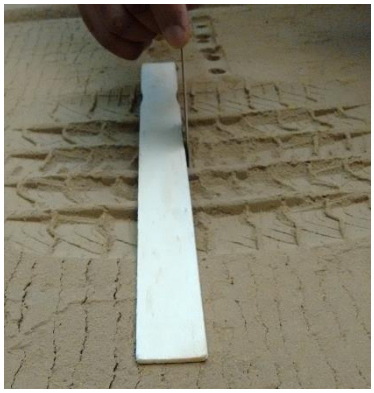

(a) Side view of the ruler.

(b) Front view of the ruler.

Figure 4.12: Measurement of the depth of the rut formed by the compaction brought by the statically loaded tire.

The design of experiment for the static tire-soil tests in October of 2019 is shown in Table 4.7. Since the loaded radius was measured at 5 kN normal load and 18, 30, and 42 psi inflation pressure in the static tire-soil tests in July of 2017, as for the loaded radius measurement tests, 5 kN normal load was excluded, and only 6 and 7 kN normal load were included. Except for the normal load levels, the tire inflation pressure levels an initial soil compaction levels remained the same as that of the tests in 2017. The rut reconstruction tests had the same normal load, tire inflation pressure, and initial soil compaction levels as that of the tests in 2017; the only difference lied in the test tire. Apart from the same SRTT, a Pirelli tire, as described in Section 4.1, was also tested.

Table 4.7: Design of experiment for the laboratory static tire-soil tests in October of 2019.

Objective	Test tire	Operational parameters	Number of levels	Levels
Loaded radius measurement	SRTT	Normal load [kN]	2	6, 7
		Tire inflation pressure [psi]/[kPa]	3	18/124, 30/207, 42/290
		Soil compaction (CI [kPa], VWC [cm^3/cm^3])	3	(224.06, 0.77%), (611.22, 0.96%), (888.00 1.09%)
Rut reconstruction	SRTT, Pirelli	Normal load [kN]	1	5
		Tire inflation pressure [psi]/[kPa]	3	18/124, 30/207, 42/290
		Soil compaction (CI [kPa], VWC [cm^3/cm^3])	3	(217.88, 0.88%), (583.21, 0.99%), (907.77, 1.11%)

It is worth mentioning that by "same initial soil compaction level", it means that the any two values of CI and VWC are at the same magnitude level respectively after the same steps of soil preparation either for low, medium, or high soil compaction level. For example, in Table 4.7, the values of CI and VWC at the low soil compaction level in the rut reconstruction tests are 217.88 kPa and 0.77%, very close to the 224.06 kPa and 0.88% at the low soil compaction level in the loaded radius measurement tests, or at the same magnitude level with the 274.58 kPa and 1.47% as listed in Table 4.6. Therefore, the initial soil compaction levels represented by these values of CI and VWC can be said to be the same.

Each static tire-soil tests in October of 2019 had almost the same procedures as that of the static tire-soil tests in July 2017, except that, in the tests for the measurement of load radius, the normal load to be reached was different, and rut length was also measured; and that

measurements of longitudinal coordinate, lateral coordinate, and rut depth were taken for several points on the rut surface or along the boundary of the rut in the tests for the rut reconstruction. One test was conducted for each of the test configurations as per Table 4.7. Therefore, totally 36 tests (runs of tests) were completed. The measured loaded radius was not substituted into Equation (4.2) to estimate the rolling radius because, in 2019, the clutch of the Terramechanics Rig was capable of being disengaged, allowing the free rolling of a tire and hence the measurement of rolling radius for a tire in towing mode (see Section 4.5.2.4).

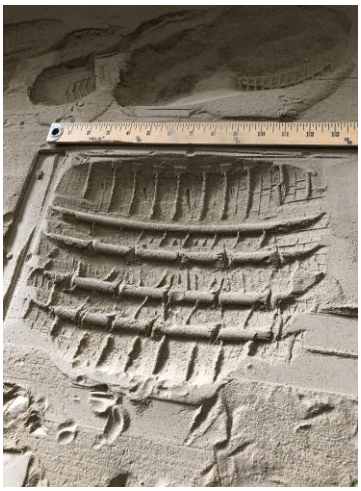

(a) Rut after the coordinates measurements were taken.

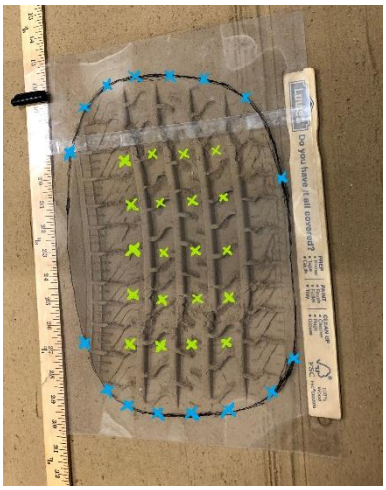

(b) Points on the rut profile of which coordinates were measured.

Figure 4.13: Measurements of longitudinal coordinates, lateral coordinates, and rut depth (vertical coordinates) for several points on the rut profile. Blue points are along the boundary of the rut (drawn on a plastic sheet); yellow points are on the surface of the rut.

The measurements of longitudinal coordinate, lateral coordinate, and rut depth (vertical coordinate) were completed by using a set of rulers. Before the coordinate measurements were taken for the points on the rut surface (the yellow points in Figure 4.13), the rut boundary was drawn on the plastic sheet in the way as described in Section 3.1. Three or four columns of points were chosen on the rut surface for the coordinate measurements; each column consisted of five points with the same lateral coordinates. Rut depth was measured for these columns of points the same way as depicted in Figure 4.12. Note that these columns of points were never chosen on the protrusion of the rut surface; the protrusion was formed in the tread pattern, as seen in Figure 4.13. Because of that, the tread pattern was not

considered in the rut reconstruction.

Drawing the rut boundary and measuring coordinates of points on the rut surface were performed in a way such that the rut was kept as intact as possible, shown in Figure 4.13a. The points along the drawn rut boundary on the plastic sheet, fourteen or sixteen of them, had zero rut depth. Only longitudinal and lateral coordinates were measured for these boundary points. The data points of longitudinal coordinate, lateral coordinate, and vertical coordinate for the aforementioned points on the rut profile were fed into a program, based on the spline interpolation, to reconstruct the 3-D rut profile.

4.4.3 Results of Laboratory Static Tire-Soil Tests

4.4.3.1 Loaded Radius and Rut Depth

The three measurements of the rut depth and loaded radius for each test configuration of the static tire-soil test in July 2017 were averaged and listed in Table 4.8. To facilitate the comparison between the results from the static tire-soil tests in July 2017 and that from the static tire deflection tests (on the rigid flat surface) in November 2016, the average measurements of loaded radius and their resultant rolling radius and percent radial deflection for both types of the tests are presented together in Table 4.8. The rolling radius of the tire on the rigid flat surface was also obtained using Equation (4.2), as Equation (4.2) was originally proposed for a tire on rigid flat surface [18].

Table 4.8: Measured loaded radius, measured rut depth and their resultant values of rolling radius and percent radial deflection. The measured data is from the static tire-soil tests in July of 2017.

Tire inflation pressure [psi]	Soil compaction	Average measured rut depth [mm]	Average measured loaded radius [mm]	Percent radial deflection [%]	Rolling radius [mm]
18	Low	28.67	310.83	21.38%	329.03
30	Low	30.33	322.83	12.01%	333.06
42	Low	28.33	328.67	7.45%	335.02
18	Medium	12.00	307.33	24.11%	327.85
30	Medium	13.67	320.67	13.70%	332.34
42	Medium	15.33	325.67	9.79%	334.01
18	High	8.00	305.50	25.55%	327.23
30	High	9.33	318.67	15.26%	331.66

42	High	9.67	324.17	10.96%	333.51
18	Rigid	N/A	299.75	30.04%	325.28
30	Rigid	N/A	312.25	20.27%	329.51
42	Rigid	N/A	319.00	15.00%	331.78

At the same inflation pressure and normal load, the deformable soil can make a difference in the tire loaded radius compared with the rigid surface. The resultant difference in percent radial deflection between the soil and the rigid surface can be as high as 8.66%, and is always larger than 4.04% for all the test levels of the inflation pressure and normal load, as displayed by Figure 4.14. From the perspective of the rolling radius, such difference in the loaded radius between the rigid surface and the soil can result in a difference in the rolling radius that ranges from 1.70 mm to 3.70 mm, which can be observed from Figure 4.15.

Soil compaction might be as influential to the rolling radius as tire inflation pressure because the difference in rolling radius, brought by the tire inflation pressure change, could be around 2.00 mm, still smaller than the 3.70 mm rolling radius difference brought by the soil compaction change. Also, it can be found from Table 4.8 and Figure 4.15 that these differences in the loaded radius and in the rolling radius between the rigid surface and the test soil tend to be more obvious as the tire inflation pressure decreases.

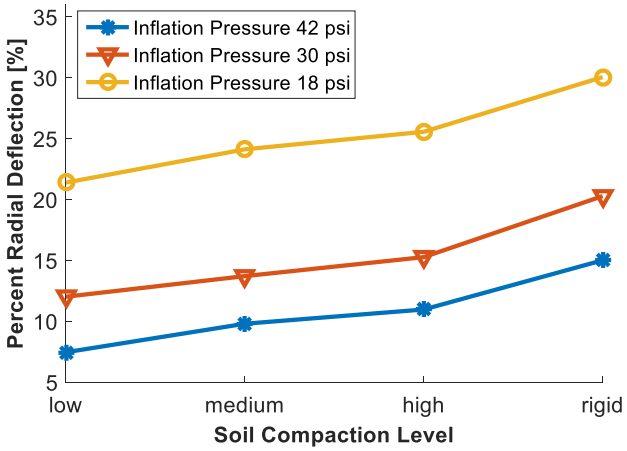

Figure 4.14: Variations of the percent radial deflection with the soil compaction level. The measured data is from the static tire-soil tests in July of 2017.

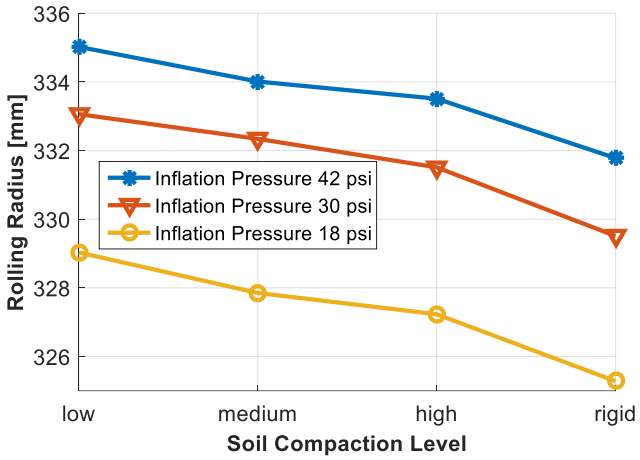

Figure 4.15: Variations of rolling radius with the soil compaction level. The measured data is from the static tire-soil tests in July of 2017.

The trend of the variations in loaded radius and in rolling radius with the soil compaction level can be summarized by analyzing the broken lines shown in Figure 4.14 and Figure 4.15. When the soil compaction increases, for all the test soil inflation pressure levels, the percent radial deflection increases, while the rolling radius decreases correspondingly. From Table 4.8 it can be found that the loaded radius at the low soil compaction level and the highest tire inflation pressure level 42 psi is the largest and the closest to the unloaded radius of the tire. This makes sense, as the tire tends to behave more like a rigid wheel on the soil when the tire inflation pressure increases and the soil compaction decreases. Table 4.8 also shows that, for the levels of initial soil compaction, inflation pressure, and normal load, the loaded radius measured in the STS tests of July 2017 was always smaller than the tire unloaded radius. Therefore, it could be reasonable to assume that the test tire, at the 5 kN normal load and at the tire inflation pressure smaller than or equal to 42 psi, is in the elastic mode of operation when running on the test soil at 6 cm/s (the test rig carriage longitudinal speed).

As for the variations in rut depth, the soil compaction plays the main role. Figure 4.16 shows the changes in rut depth among different combinations of the tire inflation pressure level and the soil compaction level. It's clear from Figure 4.16 that the lower the soil compaction level is, the higher the rut depth is. At the same tire inflation pressure level, changing the soil compaction level produces a change in rut depth of at least 4 mm, while at the same soil compaction level, changing the tire inflation pressure level results in at most a 3.33 mm change in the rut depth. Hence, it could be concluded that the rut depth varies less

with the change in the tire inflation pressure level than with the change in the soil compaction level.

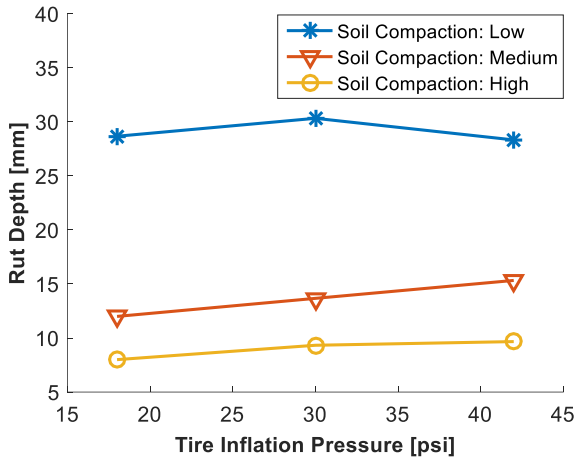

Figure 4.16: Variations of rut depth with tire inflation pressure. The measured data is from the static tire-soil tests in July of 2017.

From the static tire-soil tests in October 2019, loaded radius and rut depth were measured at the 6 and 7 kN normal load; the 18, 30, and 42 psi inflation pressure; and the low, medium, and high initial soil compaction, in addition to the measured loaded radius and rut depth from the tests in July 2017 at the 5 kN normal load and the same levels of inflation pressure and initial soil compaction. These measured data points of loaded radius for all three levels of normal load, inflation pressure, and initial soil compaction were put in one plot in Figure 4.17, so were the measured data points of rut depth in Figure 4.18.

As clearly illustrated by Figure 4.17, except for a few isolated points, the loaded radius decreases with an increase in normal load or initial soil compaction and increases with inflation pressure. Taking the top blue line in Figure 4.17b for example, if the 5 kN normal load rises to 6 kN normal load while the initial soil compaction remains the same, that top blue line moves lower than it does if the initial soil compaction rises to medium while the normal load remains the same. Similar trend happens to the top yellow line in Figure 4.17a when comparing the amount of descending between a decrease in inflation pressure at the same initial soil compaction and an increase in initial soil compaction at the same inflation pressure. Therefore, it could be concluded that the normal load and inflation pressure could be the primary influence on loaded radius, while the initial soil compaction could be the

secondary influence.

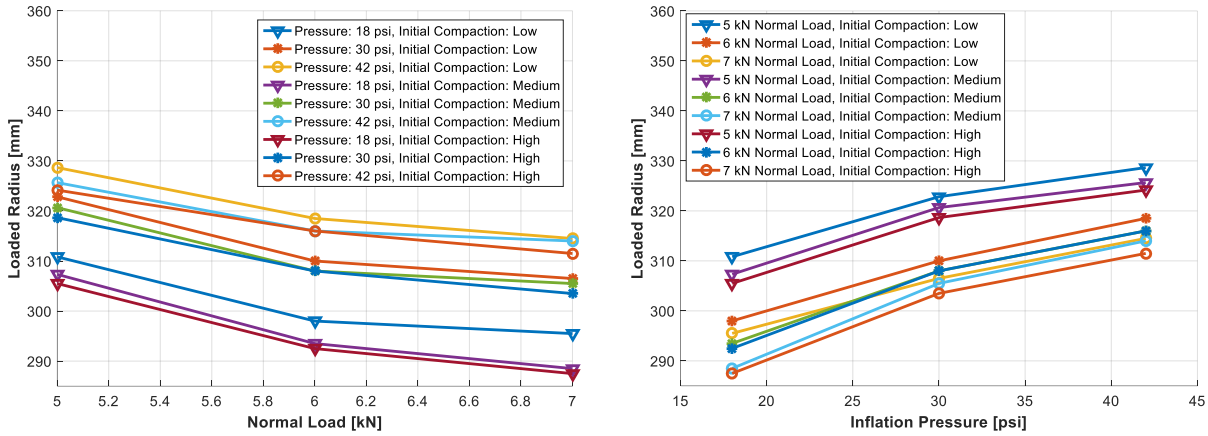

(a) Variation in loaded radius with normal load.

(b) Variation in loaded radius with inflation pressure.

Figure 4.17: Measurement data of loaded radius at 5, 6, and 7 kN normal load; 18, 40, and 42 psi inflation pressure; and low, medium, and high initial compaction. The data is from the static tire-soil tests in July of 2017 and in October of 2019.

Figure 4.18b clearly illustrates that, except for a single point, the rut depth increases with an increase in inflation pressure and a decrease in initial soil compaction. Figure 4.18a shows that, except for two points, the rut depth increases also with an increase in normal load. These exception points, all at the low initial soil compaction, are off the trend due to the soil at the low initial soil compaction was much more inhomogeneous. Analysis can be done to the top broken lines in Figure 4.18a and Figure 4.18b, similar to the analysis done to the top broken lines in Figure 4.17a and Figure 4.17b, as described in the previous paragraph. However, this time, the primary influence on the rut depth, found out of the analysis, could be the initial soil compaction, while both the normal load and inflation pressure could be the secondary influence.

Comparing the normal load and inflation pressure, the rut depth seems to be more sensitive to the latter than the former, given that the slope of the most broken lines in Figure 4.18b are slightly larger than that in Figure 4.18a. A physical explanation could be that the average ground pressure is more sensitive to inflation pressure than to normal load, similar to the trend represented by Figure 4.9; therefore, according to the Bekker's semi-empirical rut depth prediction model [14], rut depth is more sensitive to inflation pressure as the inflation

pressure influences the average ground pressure more than the normal load does.

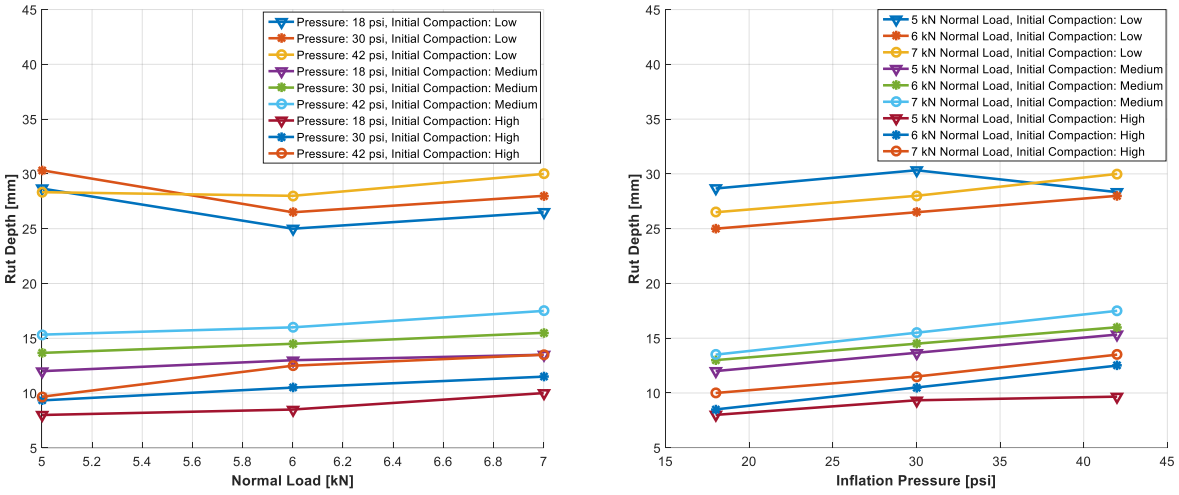

(a) Variation in rut depth with normal load.

(b) Variation in rut depth with inflation pressure.

Figure 4.18. Measurement data of rut depth at 5, 6, and 7 kN normal load; 18, 40, and 42 psi inflation pressure; and low, medium, and high initial compaction. The data is from the static tire-soil tests in July of 2017 and in October of 2019.

Rut length was also measured in the static tire-soil tests in October 2019; the measured data points are shown in Figure 4.19. It's clear from Figure 4.19 that the rut length decreases with an increase in inflation pressure or initial soil compaction and increases with normal load. The trend of rut length w.r.t. inflation pressure and normal load for the tire on soil is similar to that for the tire on hard surface; both trends result from the increase in contact patch area with an increase in normal load or a decrease in inflation pressure.

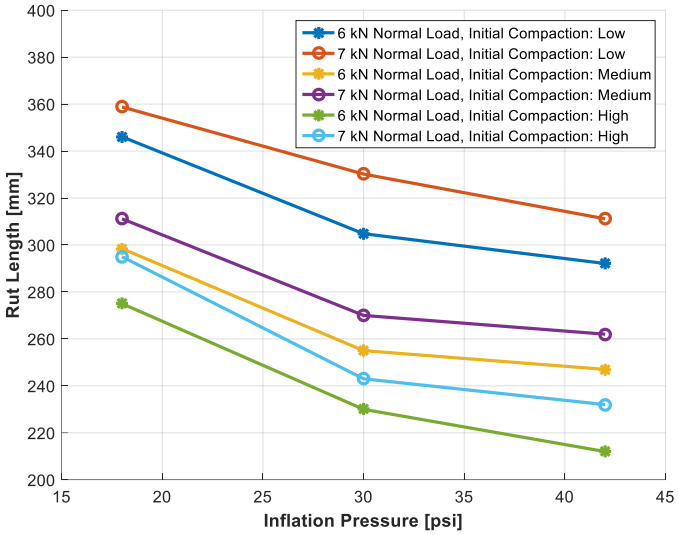

Figure 4.19: Variation in rut length with inflation pressure at 6 and 7kN normal load; 18, 40, and 42 psi inflation pressure; and low, medium, and high initial compaction. The data is from the static tire-soil tests in October of 2019.

4.4.3.2 Rut (Footprint) Reconstruction

As indicated at the end of Section 4.4.2, for each rut formed in the static tire-soil tests in October 2019, there were either 29 points (for 3 columns of points chosen on the rut surface) or 36 points (for 4 columns of points chosen on the rut surface) for which the coordinate measurements were taken. The measured longitudinal, lateral, and vertical coordinates of these 29 or 36 points (the raw data points) were fed into an interpolation program to calculate all the rest of the data points (the interpolated data points) for the rut reconstruction. An example of 36 raw data points collected is shown in Figure 4.20. The raw data points served as the basis to perform the spline interpolation which produced about 8000 interpolated data points per rut which, together with the raw data points, reconstructed a corresponding rut; the 18 ruts reconstructed this way are displayed in Figure 4.21 and Figure 4.22.

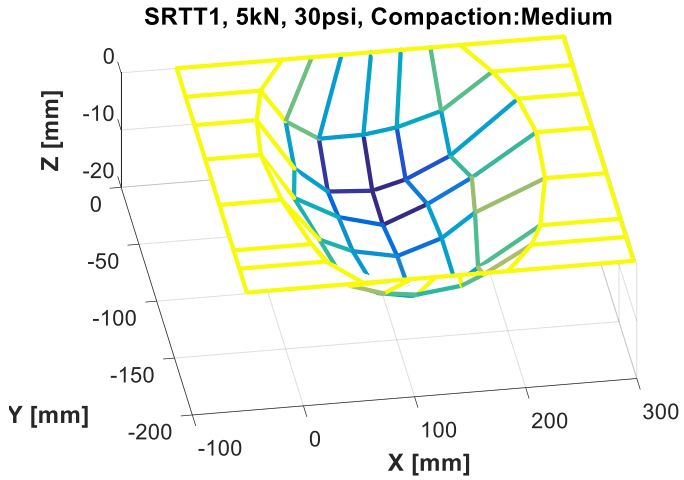

Figure 4.20: Measured data points of the longitudinal coordinate, lateral coordinate, and vertical coordinate (rut depth) of the points on the rut profile; the rut was formed by the SRTT at 5 kN normal load, 30 psi inflation pressure, and medium initial soil compaction. The data is from the static tire-soil tests in October of 2019.

Except for one or two ruts in Figure 4.21 and Figure 4.22, the trends of rut depth and rut length (the contact patch length) w.r.t inflation pressure and initial soil compaction follow the same trends as explained in Section 4.4.3.1. In addition, Figure 4.21 and Figure 4.22 indicate that the rut width, at the same inflation pressure, slightly increases with the decrease in initial soil compaction yet remained nearly the same, at the same initial soil compaction level, with the increase in inflation pressure; the former trend is due to much more sinkage and hence more area of the shoulder in contact with the soil if the initial soil compaction is reduced to the lower level. These aforementioned trends in rut length and rut width mean that the rut/footprint area (also the tire-soil contact area) tends to grow larger with a decrease in initial soil compaction level or inflation pressure when other operational parameters remain constant. At the same level of inflation pressure and initial soil compaction, the rut formed by the SRTT is smaller in width than the rut formed by the Pirelli, mainly due to the fact that the tire width of Pirelli is larger than that of the SRTT. From a few reconstructed ruts, it can be seen that these ruts are slightly unsymmetrical about the centerline in the longitudinal direction (X direction). This is due to the camber angle, occasionally, being slightly positive since 2019, although efforts were made to make the camber angle zero as it was in 2017.

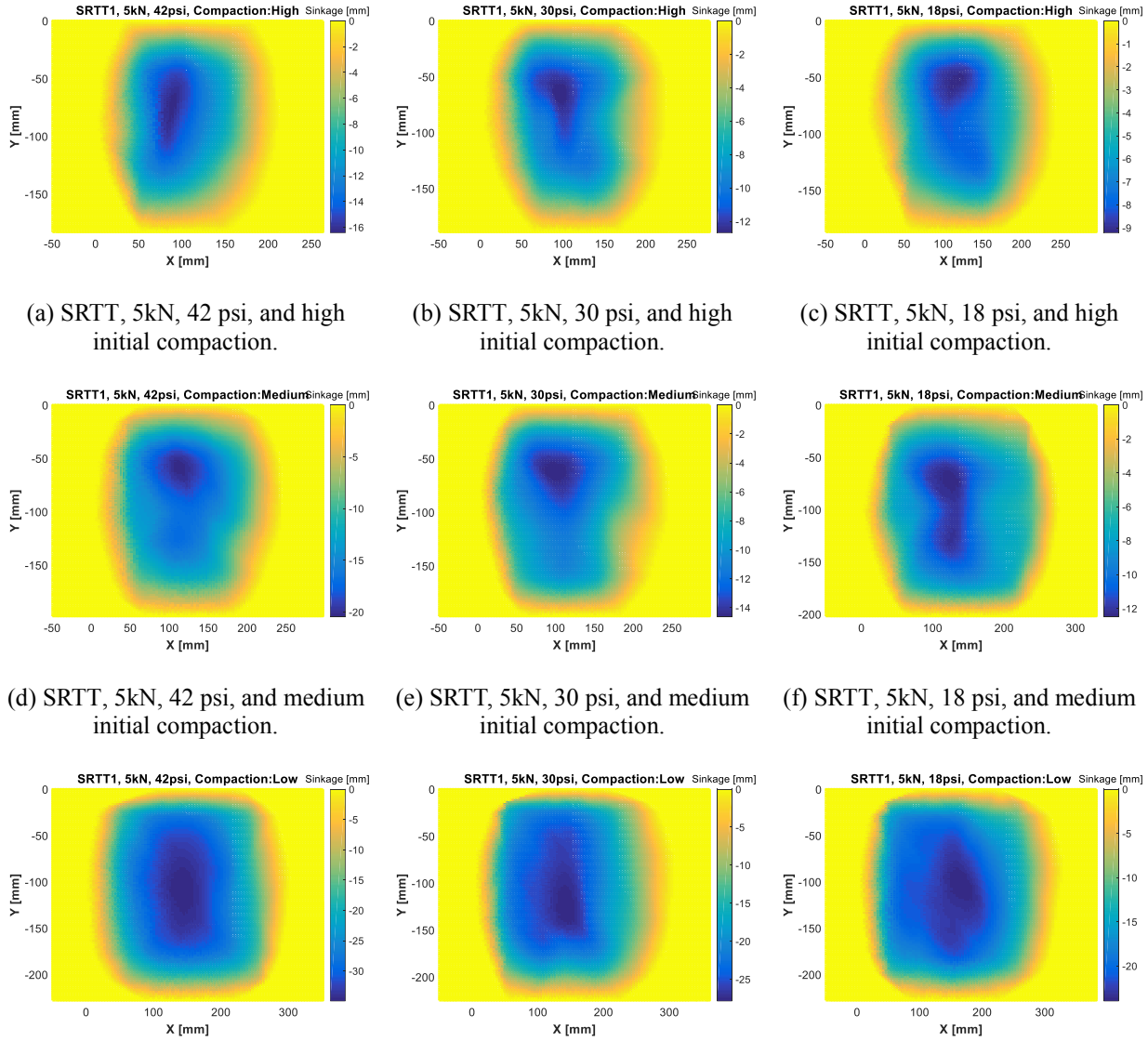

(a) SRTT, 5kN, 42 psi, and high initial compaction.

(b) SRTT, 5kN, 30 psi, and high initial compaction.

(c) SRTT, 5kN, 18 psi, and high initial compaction.

(d) SRTT, 5kN, 42 psi, and medium initial compaction.

(e) SRTT, 5kN, 30 psi, and medium initial compaction.

(f) SRTT, 5kN, 18 psi, and medium initial compaction.

(g) SRTT, 5kN, 42 psi, and low initial compaction.

(h) SRTT, 5kN, 30 psi, and low initial compaction.

(i) SRTT, 5kN, 18 psi, and low initial compaction.

Figure 4.21: Rut reconstruction for SRTT at 18, 30, and 42 psi and low, medium, and high initial soil compaction. The ruts were formed in the static tire-soil tests in October of 2019.

If only for studying the influence of inflation pressure, normal load, or initial soil compaction on the rut size parameters, it would not have been necessary to reconstruct the rut because simply measuring a few rut size parameters will be sufficient. One application of rut reconstruction is to parameterize pressure-sinkage models. As pointed out in Section 2.3.2, commonly parameterization methods that rely on plate-sinkage tests could not sufficiently represent tire-soil interaction while the rut reconstructed this way here definitely

can. A new parameterization method based on the rut reconstruction could work this way: (1) the pressure-sinkage model is substituted to each data point that reconstructs a rut and next integrated over all the data points used in the rut reconstruction; (2) for several ruts, the integration is repeated as described in (1), and the differences between the integration results and normal load are summed up as a cost function; (3) the parameters of the pressure-sinkage model are tuned such that the cost function is minimized within an acceptable error.

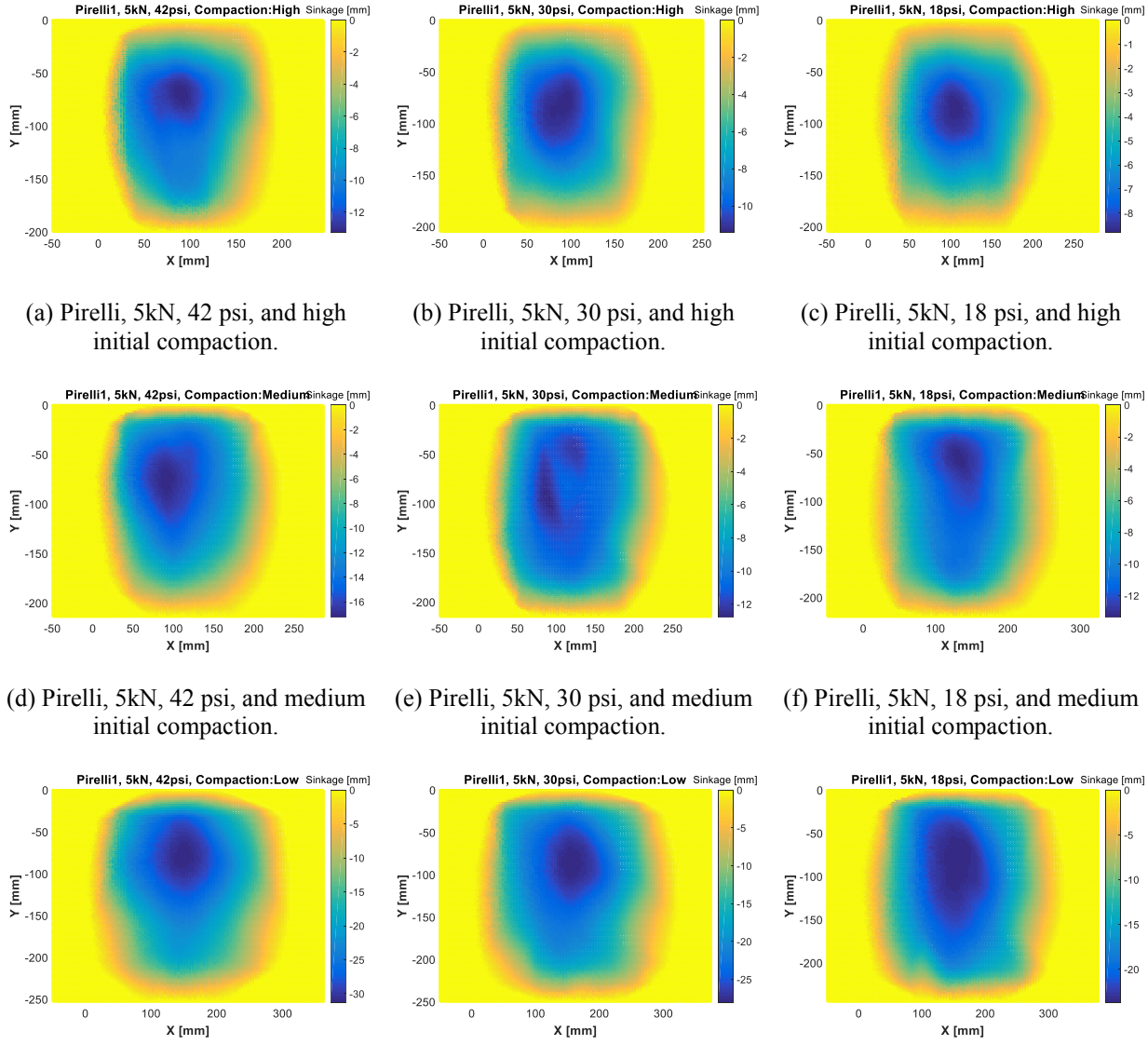

(a) Pirelli, 5kN, 42 psi, and high initial compaction.

(b) Pirelli, 5kN, 30 psi, and high initial compaction.

(c) Pirelli, 5kN, 18 psi, and high initial compaction.

(d) Pirelli, 5kN, 42 psi, and medium initial compaction.

(e) Pirelli, 5kN, 30 psi, and medium initial compaction.

(f) Pirelli, 5kN, 18 psi, and medium initial compaction.

(g) Pirelli, 5kN, 42 psi, and low initial compaction.

(h) Pirelli, 5kN, 30 psi, and low initial compaction.

(i) Pirelli, 5kN, 18 psi, and low initial compaction.

Figure 4.22: Rut reconstruction for Pirelli at 18, 30, and 42 psi and low, medium, and high initial soil compaction. The ruts were formed in the static tire-soil tests in October of 2019.

Another application of the rut reconstruction is the estimation of the pressure distribution in the tire-soil contact patch with a correctly parameterized pressure-sinkage model at hand. This can serve as an alternative estimation method to other estimation methods of the pressure distribution in the tire-soil contact patch some of which relies on miniature pressure transducers. The rut reconstruction method proposed in this section could also be considered a cheap alternative way, relative to the rut reconstruction method replying on image processing technique [15], [67]

4.5 Laboratory Dynamic Tire-Soil Test

In each laboratory dynamic tire-soil test, the tire was driven at a preset slip ratio (or preset slip ratios) or towed on the prepared flat soil from the rear to the front end of the soil bin, with the tire normal load controlled around a preset value; wheel forces and moments were measured and recorded during the movement of the tire. After the test tire reached the front end of the soil bin, several spots along the path of the tire were chosen to measure the rut geometric parameters and, occasionally, to measure the post-traffic cone index. In this section, the procedures of the lab DTS test along with the design of experiment are introduced first. Next, some of the test data is presented, followed by analyses of the data mainly in the following aspects: tire performance, soil response, and multi-pass effect.

4.5.1 Procedures of Laboratory Dynamic Tire-Soil Test

Each lab DTS test began with the soil preparation that included shoveling, tilling, leveling, and occasionally compacting the soil, following the method as described in Section 3.2. The soil preparation resulted in a flat soft soil track, with soil properties being as homogenous as possible to achieve, at low initial soil compaction level (after 0 trips of the roller compacting), medium initial soil compaction level (after 2 trips of the roller compacting), or high initial soil compaction level (after 8 trips of roller compacting). Next, CI and VWC were measured at eight evenly distributed spots along the soil track, as shown in Figure 4.23b. The CI and VWC were measured in the same way as described in Section 3.1. It is worth mentioning that in this study, the VWC was measured for the soil from the surface to

a depth of 12 cm, because of the HS2P being equipped with a pair of 12 cm sensor rods; the CI was measured up to a depth of 12 cm, and the soil was sampled from the surface to the soil depth of 10.08 cm in the lab SP test. These values of soil depth were selected by design to be very close to each other and to be in a range of 0 – 15 cm, as it was estimated that during the lab DTS test, the soil interacting with the tire (the soil of interest) would be in the soil depth of the range 0 – 15 cm based on the soil sinkage data from [127].

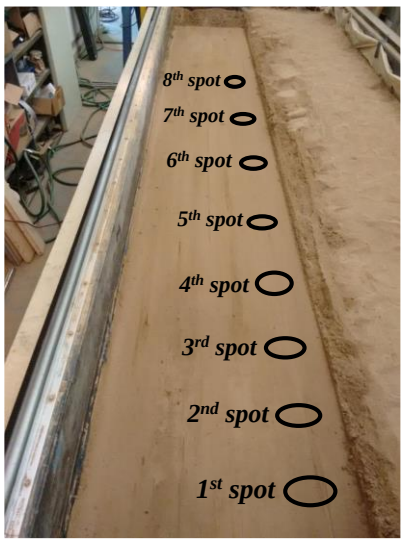

(a) All the spots for the soil parameter measurements.

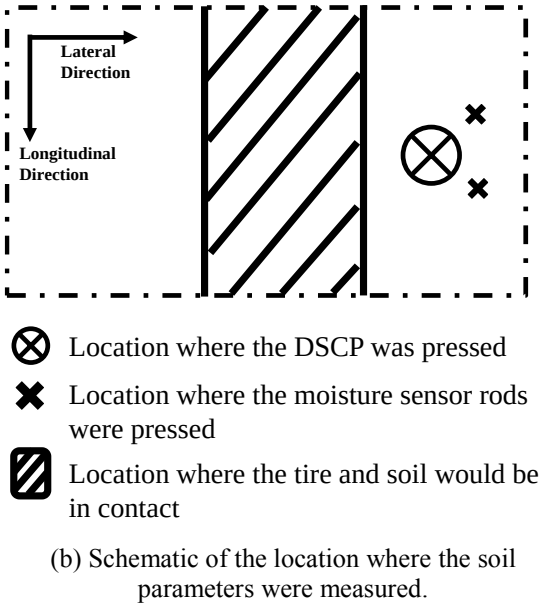

(b) Schematic of the location where the soil parameters were measured.

Figure 4.23: Soil parameter measurements along the prepared soil.

After the measurements of the soil parameters, the value of the wheel motor's revolution speed, one to one mapping to the wheel revolution speed ω_w, calculated by Equation (2.1), was set corresponding to the nominal slip ratio to be tested; this step was skipped if the tire was to be tested in the free-rolling/towing mode. The normal load was applied to the tire gradually until it reached the 5 kN nominal normal load and maintained around 5 kN.

Next, the test tire mounted onto the carriage was moved on the prepared soil in a straight line, from the rear to the front end of the soil bin. At the end of each test, measurements of rut depth were taken at eight almost evenly distributed locations along the soil track, as seen in Figure 4.23a, by using rulers in a similar way with the one shown in Figure 4.12. As for the laboratory dynamic tire-soil tests in 2017, totally, 42 tests were completed, and every one of them was for each combination of the levels of the tire inflation pressure and nominal slip

ratio, as listed in Table 4.9, while the initial soil compaction remained to be low (0 trips of the roller compacting)

Table 4.9: Design of experiment for the laboratory dynamic tire-soil tests in 2017.

Operational parameters	Number of levels	Levels
Nominal normal load [kN]	1	5
Nominal slip ratio [%][a]	14	0, 2.5, 5, 7.5, 10, 12.5, 15, 17.5, 20, 30, 40 ,50 ,60 ,70
Tire inflation pressure [psi]/[kPa]	3	18/124, 30/207, 42/290
Rolling radius [mm]	3	329.028, 333.063, 335.017
Soil compaction (CI [kPa], VWC [cm^3/cm^3])	1	(253.12, 1.21%), (247.98, 1.23%), (245.45, 1.21%)[b]

[a] Pure longitudinal slip, zero camber angle and toe angle.
[b] The first entry is for 18 psi, the second entry is for 30 psi, and the third entry is for 42 psi.

The measurements of the CI and VWC were averaged for each tire inflation pressure level and were listed in the last row of Table 4.9. In the lab DTS tests of 2017, the low soil compaction level as described in Section 4.4.2 was achieved. The prepared soil for all the three levels of the tire inflation pressure had almost the same soil compaction level, which can be demonstrated by the last row of Table 4.9 that both the CI and VWC in any pair of parentheses are close to that in other pairs of parentheses. The soil compaction and the tire inflation pressure influence the values of rolling radius. The rolling radius values in the lab DTS test of 2017 were approximated by the rolling radius values in Table 4.8, under the 18 psi, 30 psi, and 42 psi tire inflation pressure; the soil compaction level of 274.58 kPa CI and 1.47% VWC (slightly different from the soil compaction level listed in Table 4.9); and the 5 kN tire normal load. These rolling radius values in Table 4.8 were obtained from the static tire-soil tests in July of 2017. Either of these rolling radius values was plugged into Equation (2.1) to obtain the wheel motor's revolution speed required by the nominal slip ratio at the matching inflation pressure and initial soil compaction as specified in Table 4.9.

Later, in 2019, with the clutch installed onto the Terramechanics Rig, it was feasible to conduct dynamic tire-soil tests in the towing mode (the free-rolling mode), as displayed in Figure 4.24. The rolling radius, defined in the towing mode as the zero condition, could be directly measured by dividing the measured wheel longitudinal speed (6cm/s) by the measured wheel revolution speed (measured by the Kistler wheel hub). With this testing capability, laboratory dynamic tire-soil tests in towing mode (the laboratory free-rolling tire-

soil tests), additional laboratory dynamic tire-soil tests (referred to as the lab DTS tests of 2019 or similar phrases to differ with the lab DTS tests of 2017), and laboratory multi-pass dynamic tire-soil tests (the laboratory multi-pass tire-soil tests) were conducted in 2019. The DOE of these three types of tests are shown in Table 4.10, Table 4.11, and Table 4.12.

Figure 4.24: Terramechanics Rig in a laboratory free-rolling tire-soil test of 2019.

Table 4.10: Design of experiment (DOE) for additional laboratory free-rolling tire-soil tests in 2019.

Operational parameters	Number of levels	Levels
Nominal normal load [kN]	3	5, 6, 7
Tire inflation pressure [psi]/[kPa]	3	18/124, 30/207, 42/290
Soil compaction (CI [kPa], VWC [cm^3/cm^3])	3	(222.30, 0.92%), (697.71, 1.38%), (980.52, 1.37%)

The procedures of the laboratory free-rolling tire-soil tests, laboratory dynamic tire-soil tests in 2019, and laboratory multi-pass tire-soil tests were almost the same as that of the laboratory dynamic tire-soil tests in 2017, except for these following aspects:

(1) As shown in Table 4.11, the normal load tested in the free-rolling tests also included 6 kN and 7 kN; the medium and high initial soil compaction levels were also tested. Before the tire moves on the soil from the starting position in each test, the clutch (Figure 3.2b) was disengaged to ensure zero wheel torque.

(2) The additional lab DTS tests in 2019 tested tire on soil at the medium (2 trips of the

roller compacting) and high (8 trips of the roller compacting) initial soil compaction levels. Due to the limit from the schedule and the safety concern about the newly replaced wheel motor drive's capability of testing high slip ratios, seven nominal slip ratios were tested, up to 30%. Rut width was also measured in these additional lab DTS tests.

Table 4.11: Design of experiment for the laboratory dynamic tire-soil tests in 2019.

Operational parameters	Number of levels	Levels
Nominal normal load [kN]	1	5
Nominal slip ratio [%][a]	7	2, 4, 8, 12, 16, 20, 30
Tire inflation pressure [psi]/[kPa]	3	18/124, 30/207, 42/290
Rolling radius [mm][b]	6	331.90, 336.60, 339.50, 330.80, 334.30, 336.50
Soil compaction (CI [kPa], VWC [cm^3/cm^3])	2	(601.16, 1.20%), (925.93, 1.26%)

[a] Pure longitudinal slip, zero camber angle and toe angle.
[b] The 1st – 3rd entries are for 18 psi, 30 psi, and 42 psi and medium initial compaction respectively; the 4th – 6th entries are for 18 psi, 30 psi, and 42 psi and high initial compaction respectively.

(3) The rolling radius values, used to set the nominal slip ratios in both lab DTS tests in 2019 and lab multi-pass tire-soil tests, were measured directly from the lab free-rolling tire-soil tests. The levels of inflation pressure, tire normal load, and initial soil condition for the same rolling value matched between any two tests of these three types of tests, as indicated by Table 4.10, Table 4.11, and Table 4.12.It is worth mentioning that the rolling radius values in the lab DTS tests in 2017 was not obtained this way because the Terramechanics Rig didn't have the capability of free-rolling tests back then. This is why the rolling radius values in the lab DTS tests in 2017 were estimated as described earlier in this section.

Table 4.12: Design of experiment for the laboratory multi-pass tire-soil tests in 2019.

Operation mode	Operational parameters	Number of levels	Levels
Towing mode	Normal load [kN]	1	5
	Tire inflation pressure [psi]/[kPa]	3	18[a]/124, 30/207, 42/290
	Soil compaction (CI [kPa], VWC [cm^3/cm^3])	2	(265.25, 0.86%), (515.85, 1.06%)
Driving mode	Normal load [kN]	1	5
	Nominal slip ratio [%][b]	4	4, 8, 12 ,20
	Tire inflation pressure [psi]/[kPa]	1	42/290
	Number of passes	3	1, 2, 3[c]
	Rolling radius [mm]	1	339.50
	Soil compaction (CI [kPa], VWC [cm^3/cm^3])	1	(586.08, 1.06%)

[a] Tire at 18 psi inflation pressure was only tested at medium initial soil compaction not at low initial soil compaction.
[b] Pure longitudinal slip, zero camber angle and toe angle.

[c] All three passes had the same nominal slip ratios.

(4) At the end of each run of the lab DTS tests in 2019 and lab multi-pass tire-soil tests, the tire was lifted up and away from its final position. The tire left a rut (footprint) in its final position, as seen in Figure 4.25; measurements of footprint depth and footprint length were taken for both types of tests. The footprint depth was taken as the tire sinkage, based on the assumption that the soil rebound of the test, after unloading and lifting the tire, is negligibly small, as explained in Section 2.1. For the lab multi-pass tests, measurements of longitudinal and lateral coordinates were taken at several points along the footprint boundary.

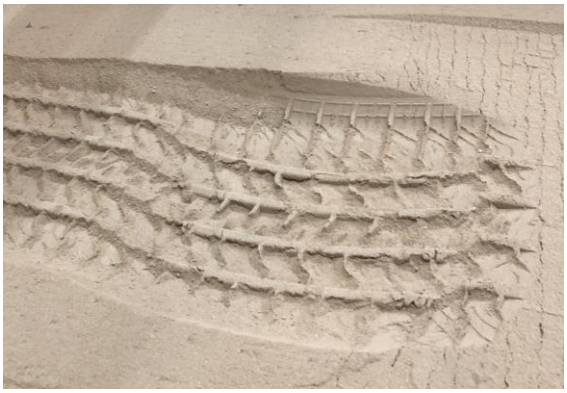

Figure 4.25: Footprint (rut) left by the tire in its final position. The footprint was formed in a static tire-soil test in October of 2019.

(5) As for the tests at the same inflation pressure, nominal slip, and initial soil compaction level, each of the three passes were conducted at the same nominal slip ratio. After each pass in the lab multi-pass tire-soil tests, three spots along the tire path were chosen for the measurement of cone index. Too much penetration of the cone penetrometer into the tire path which would change the soil mechanical property of the tire path left by the previous pass. This is why the number of cone index measurements was restricted to three. Also, rut depth and footprint depth (taken as the tire sinkage as explained in the previous bullet) were also measured. The measurement of cone index and rut depth also followed the same way as described in Section 3.1.

Totally, 27 lab free-rolling tire-soil tests, 42 additional lab DTS tests, and 9 lab multi-pass tire-soil tests were completed in 2019.

4.5.2 Results of Laboratory Dynamic Tire-Soil Tests

4.5.2.1 Initial Soil Condition

In each lab DTS test, before the test tire started to move on the soil, the CI and VWC were measured as described in Section 4.5.1. The measurement data of the CI and VWC for the prepared soil in each lab DTS test were averaged and plotted in Figure 4.26, Figure 4.27 and Figure 4.28. These plots show acceptable variations in CI and slight variations in VWC at the same initial soil compaction level. Considering the inhomogeneous soil properties of the test soil, it's difficult to repeat an identical initial soil condition for all the lab DTS tests at the same initial soil compaction level after completing the soil preparation. With such difficulty pointed out, and given the acceptable variations in CI and the slight variations in VWC, it might be reasonable to conclude that, among different lab DTS tests completed at the same initial soil compaction level, the initial soil condition (characterized by both CI and VWC) remained similar; the major influence on the variation in the parameters that characterize the tire performance and soil response could be assumed to come from a change in slip ratio, in tire inflation pressure, or in tire normal load, but not from the initial soil condition.

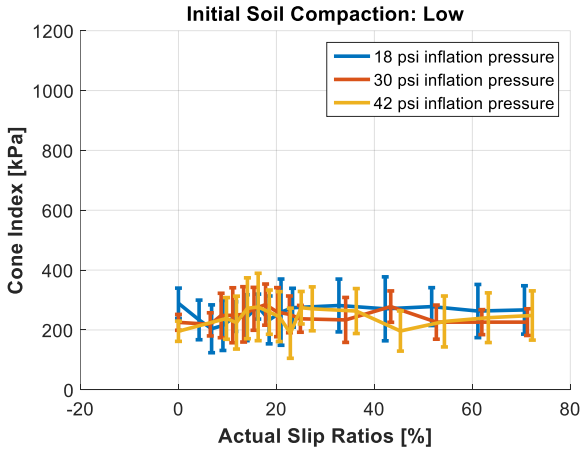

(a) CI at low initial soil compaction.

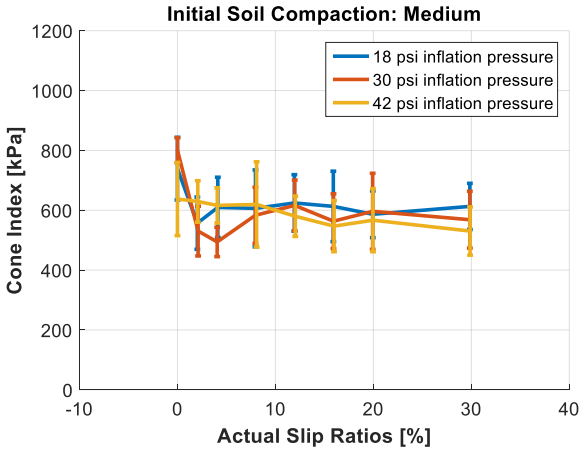

(b) CI at medium initial soil compaction

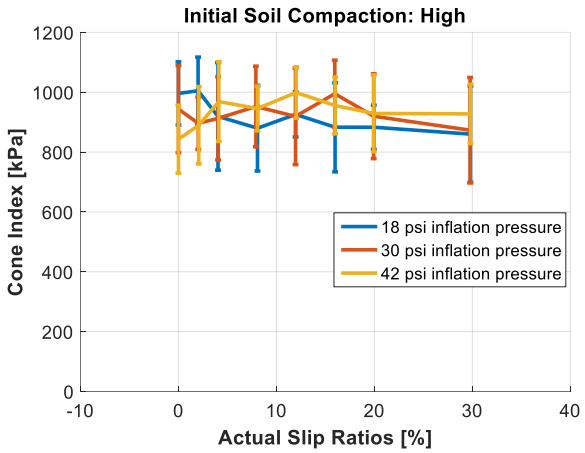

(c) CI at high initial soil compaction.

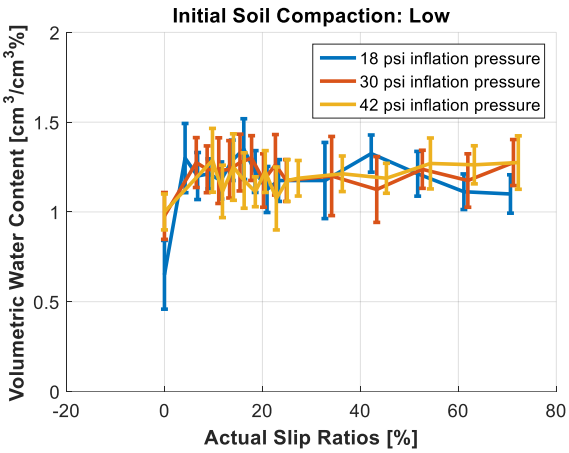

(d) VWC at low initial soil compaction.

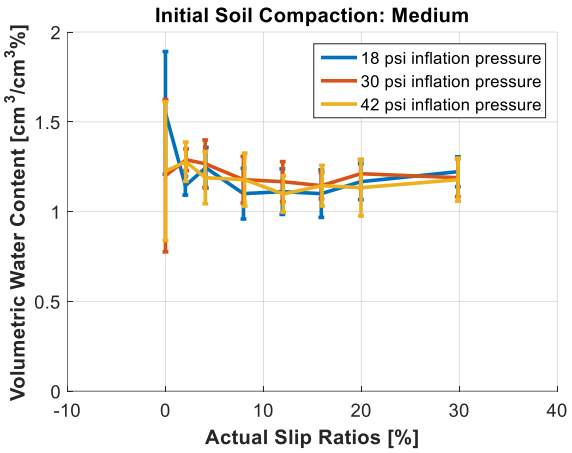

(e) VWC at medium initial soil compaction.

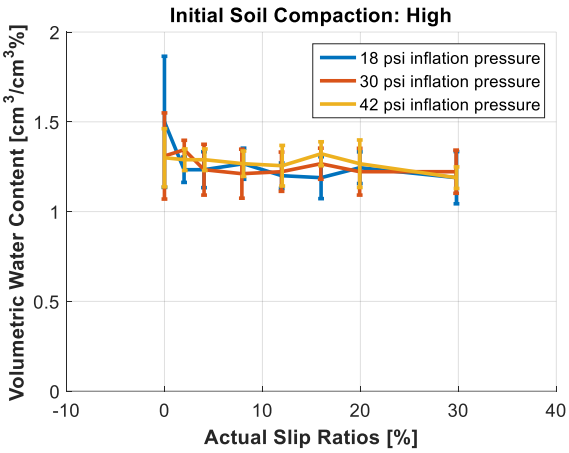

(f) VWC at high initial soil compaction.

Figure 4.26: Measured cone index and volumetric water content data from the lab DTS tests at various slips.

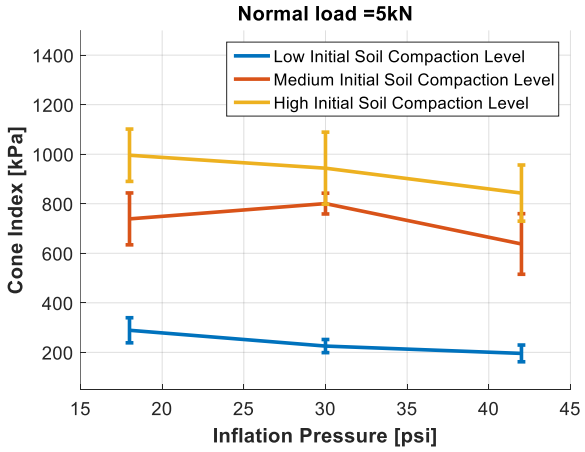

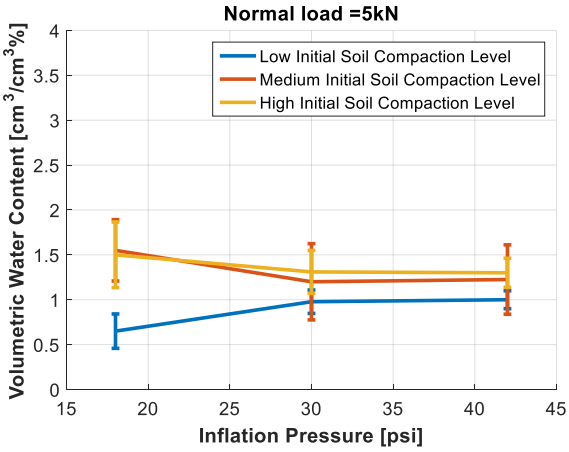

(a) CI before the tests at 5 kN normal load.

(b) VWC before the tests at 5 kN normal load.

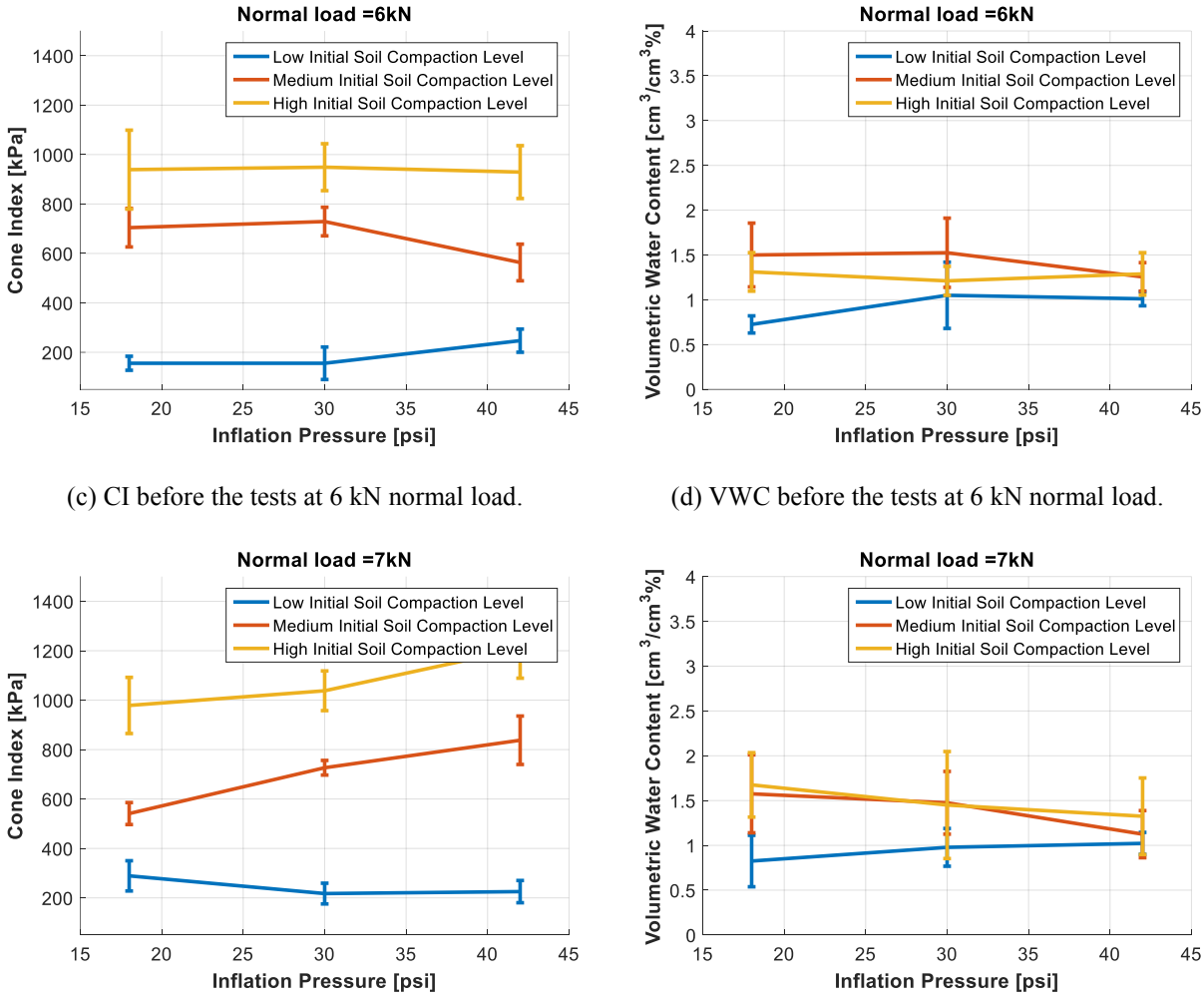

(c) CI before the tests at 6 kN normal load.

(d) VWC before the tests at 6 kN normal load.

(e) CI before the tests at 7 kN normal load.

(f) VWC before the tests at 7 kN normal load.

Figure 4.27: Measured cone index and volumetric water content data from the lab free-rolling tire-soil tests.

From Figure 4.26 and Figure 4.27, it can be seen that the cone index mean values at the low, medium, and high initial soil compaction levels fall mostly and respectively in 180 – 280 kPa, 580 – 750 kPa, and 850 – 100 kPa; while the volumetric water content mean value stayed between 0.7% and 1.5% mostly as the soil was deliberately kept dry. As for the multi-pass tests, the measured cone index data right after the soil preparation was plotted together with that after each of the three passes to illustrate the multi-pass effect, as it will be shown in Section 4.5.2.6. The soil tended to be more homogeneous at medium or high initial soil compaction level than it did at low initial soil compaction level as soil was compacted by the roller in the former case yet not in the latter case. Since the soil was more inhomogeneous,

which is not reflected in the plots about the measured CI and VWC data, it occurred more that the tire performance and soil response had larger variation in the test at low initial soil compaction level. This can be illustrated, for example, by Figure 4.35c, Figure 4.38a, and Figure 4.38c and by looking at the error bars that denote standard deviations.

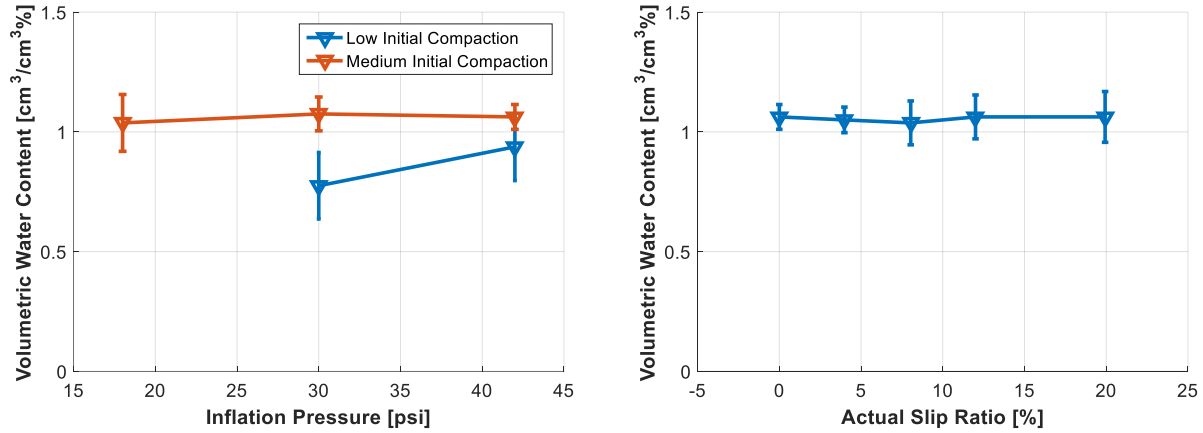

(a) Variation in volumetric water content in the multi-pass tests in the towing mode.

(b) Variation in volumetric water content in the multi-pass tests at multiple slip ratios.

Figure 4.28: Measured volumetric water content data from the laboratory multi-pass tire-soil tests.

4.5.2.2 Performance of the Slip and Normal Load Controllers

For each DTS test, the raw data from around 10,000 measurements of parameters was collected by the KISTLER system and LMS Test. Lab. The parameters measured included wheel force/moments, wheel angular position and velocity, etc. The parameter measurement for each test took about 60 seconds. A considerable portion of the raw data about the parameters of interest was extracted based on two criteria: (1) the measurement was taken when the carriage was in translation at the longitudinal velocity of 6 cm/s, and the tire was in steady-state behavior, i.e., the drawbar pull and wheel torque were around a constant value and not surging or declining drastically; and (2) the values of the actual normal load and actual slip ratio from the measurement were in the vicinity of the nominal values. This extracted data was used to produce plots about the tire performance in the Section 4.5.2.4, 4.5.2.5 and 4.5.2.6.

As for the lab DTS tests in 2017, slip ratio can be obtained by plugging in Equation (2.1) the values of the wheel revolution speed recorded by Kistler wheel hub, the rolling radius presented in Table 4.9, and the wheel longitudinal speed (6 cm/s as described in Section 3.1). Each value of the actual slip ratio in Figure 4.29 was determined by calculating the mean of the slip ratios that were obtained by using Equation (2.1) and the measured wheel revolution speed from the extracted data. The actual slip ratio and the nominal slip ratio (the target slip ratio) are displayed in Figure 4.29 for each lab DTS test in 2017.

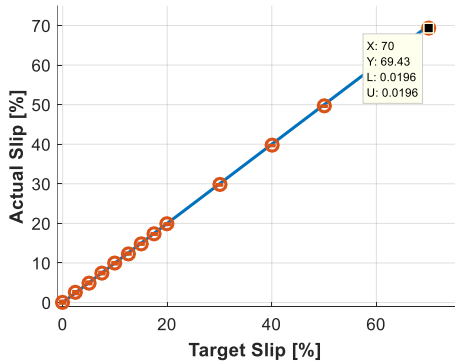

(a) Comparison between the target slip and actual slip at 42 psi inflation pressure.

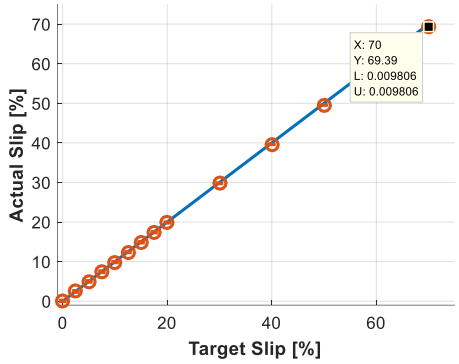

(b) Comparison between the target slip and actual slip at 30 psi inflation pressure.

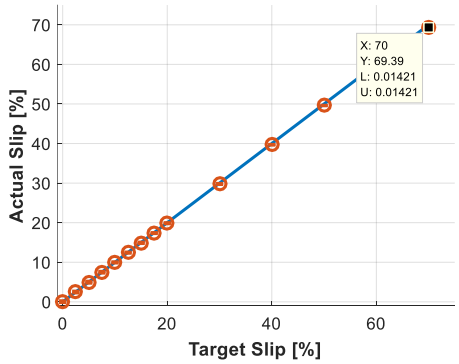

(c) Comparison between the target slip and actual slip at 18 psi inflation pressure.

Figure 4.29: Performance of the tire slip controller in the lab DTS tests of 2017 at low initial soil compaction.

Similarly, the measurement data of the actual normal load from the aforementioned extracted data was averaged at each level of the nominal slip ratio (target slip). These average values of the actual normal load measurement data, together with their corresponding standard deviations, are plotted against the actual slip ratios, as shown in Figure 4.30.

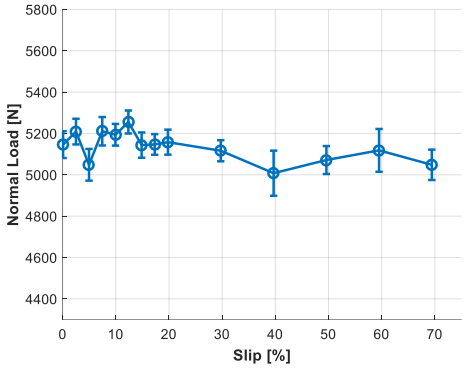

(a) Average normal load at 42 psi inflation pressure.

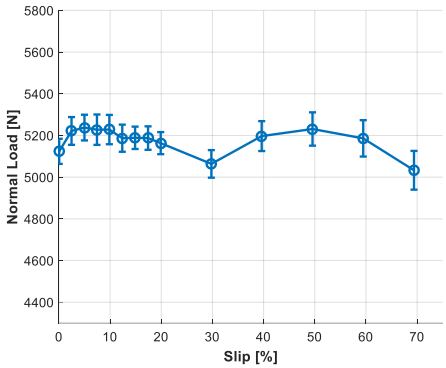

(b) Average normal load at 30 psi inflation pressure.

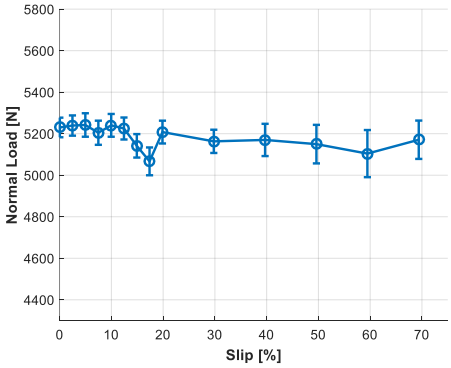

(c) Average normal load at 18 psi inflation pressure.

Figure 4.30: Performance of the tire normal load controller in the lab DTS tests of 2017 at low initial soil compaction.

Figure 4.29 and Figure 4.30 both indicate that the nominal slip ratio and the nominal normal load were tracked at acceptable errors, as the actual slip ratio was almost equal to the

nominal slip ratio, and the average of the actual normal load measurement data was always kept within a ± 0.3 kN deviation from the 5 kN nominal normal load, the latter of which means that given the good performance of the normal load controller, the actual tire normal load, unlike the slip ratio and tire inflation pressure, had negligibly minor influence on the variations in the tire performance parameters or soil response parameters among different tests at the same nominal normal load.

4.5.2.3 Rut Profile Observation

Some observations have been made about the rut formed by the tire-soil interaction that occurred in the lab DTS tests of 2017. The rut shoulder was flat at low levels of slip ratio, as shown in Figure 4.31c, while at high levels of slip ratio, for example, it can be seen from Figure 4.31a that the rut shoulder protruded above the original undisturbed flat soil surface. The protrusion of the rut shoulder at high slip ratios might be explained by the corresponding more severe bulldozing effect of the tire sidewall. The slip sinkage increases with the slip ratio, which contributes to the increase in the tire sinkage. As a result, the sidewalls of the tire have a larger area in contact with the soil at high slip ratios, hence intensifying the bulldozing effect of the tire sidewall.

(a) Rut shoulder at the sides of the rut. (b) Rut bottom profile at a high slip ratio. (c) Rut bottom profile at a low slip ratio.

Figure 4.31: Rut brought by the tire motion on the soft soil in some of the laboratory dynamic tire-soil tests of 2017. The initial soil compaction was low.

Also, it was found that at medium or high slip ratios, the rut bottom surface became wavy, unlike the relatively flat rut bottom surface at low slip ratios, which is illustrated by Figure

4.31b and Figure 4.31c. Comparing Figure 4.31a and Figure 4.31c, it can be seen that the amplitude of fluctuation (fluctuation amplitude), i.e., the vertical distance between a peak and its following trough, is larger in case of a high slip ratio than that in case of a low slip ratio. Besides, the rut at high slip ratio has a higher frequency of fluctuation (fluctuation frequency), i.e., the number of the peaks or the troughs in the rut, than that does at low slip ratio, as shown in Figure 4.31a and Figure 4.31c. The fluctuation in the rut was also observed in the dynamic rigid wheel soil test, and the fluctuation was accounted for by a vibration term in addition to the classical Bekker pressure-sinkage model [136]. However, no physical explanation was given in [136] about the fluctuation of the pressure in the wheel-soil interface. In some paper on the wheel-soil interaction, such fluctuation in the rut bottom surface was referred to as "ripple" [137]; the ripple formation was successfully simulated in the FEM environment [138]. When the slip ratio is sufficiently large, the tip of the local shear failure zone, in proximity to the soil moved by the wheel, spreads to the soil surface, and the soil is moved in a way that a ripple forms [138].

Not only the rut profile but also the variation in drawbar pull with time was featured with fluctuation in the DTS tests of 2017. The variations of DP with time at four levels of slip ratio is shown in Figure 4.32. Fluctuation can be seen in the DP. At high inflation pressure (42 psi), the fluctuation amplitude of DP at small slip ratios looks larger than that at large slip ratios in Figure 4.32a, which, however, doesn't occur at small inflation pressure (18 psi) in Figure 4.32c.

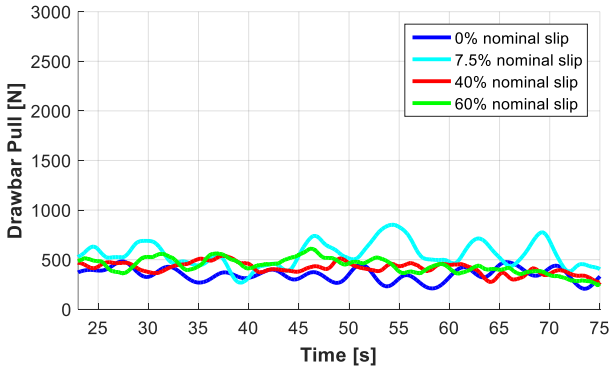

(a) Variations of DP with time at 42 psi inflation pressure.

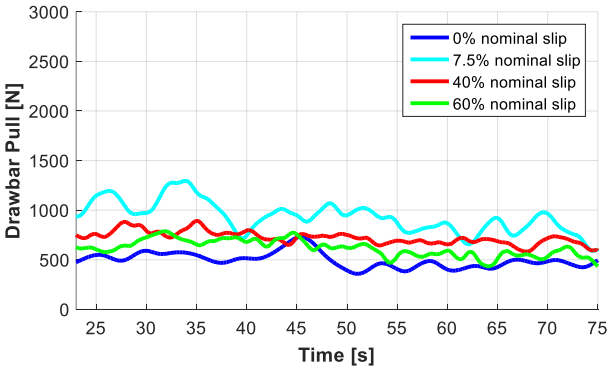

(b) Variations of DP with time at 30 psi inflation pressure.

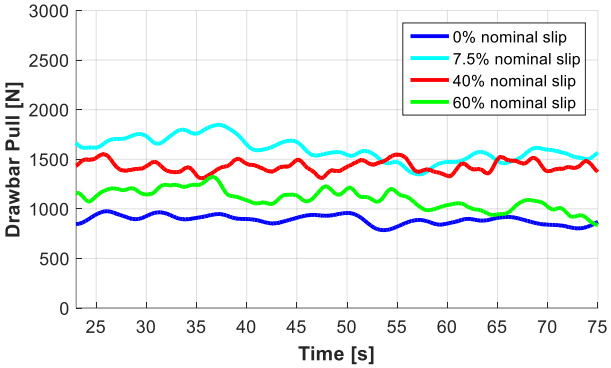

(c) Variations of DP with time at 18 psi inflation pressure.

Figure 4.32: DP vs. time in several lab DTS tests of 2017 at low initial soil compaction.

At medium or high initial soil compaction level, the wavy, layered rut bottom surface was also observed in some of the lab DTS tests of 2019. Picture evidences are provided in Figure A. 1 – Figure A. 6, Appendix. The trend of the fluctuation amplitude and fluctuation frequency w.r.t. slip ratio is the same as that for the lab DTS tests at low initial soil compaction level: the fluctuation amplitude becomes larger at higher slip ratios, and the fluctuation frequency increases with slip ratio. Figure A. 1 – Figure A. 6 display that the rut fluctuation appears when the slip ratio is larger than a certain value between 8% and 12 %; at 8% slip ratio, the rut bottom surface can still be considered flat; at 12% slip ratio, the rut bottom surface is already wavy. Although no rut fluctuation is seen at low slip ratios smaller than 8% in the lab DTS tests of 2019 (at medium and high initial soil compaction), fluctuation in drawbar pull coefficient with tiny fluctuation amplitude can be found in Figure 4.33 at low slip ratios such as 2% and 4%.

However, unlike Figure 4.32a and Figure 4.32b in which the fluctuation amplitude of DP at small slip ratios can be relatively large, in Figure 4.33, the fluctuation amplitude of DPC

, at small slip ratios, i.e., 2% or 4%, is small and smaller than that at medium slip ratios, i.e., 12%, 20%, or 30%. A possible explanation for that is: it seems that the low initial compaction could bring out relatively a large fluctuation amplitude in DP or DPC, especially at 42 psi inflation pressure, while the medium or high initial soil compaction could not, possibly and partly due to the soil being more inhomogeneous at low initial compaction. This explanation is possibly supported by Figure 4.34.

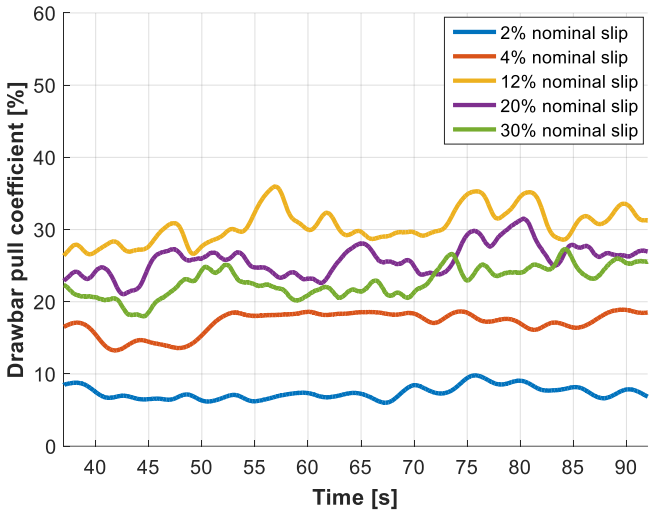

(a) Medium initial soil compaction, 30 psi inflation pressure.

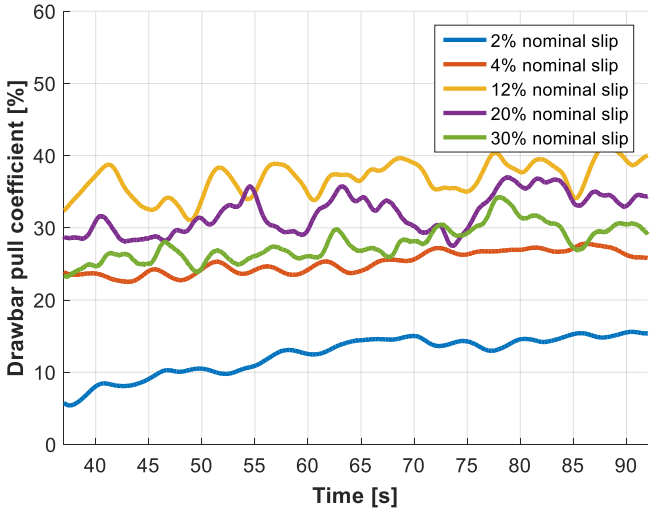

(b) High initial soil compaction, 30 psi inflation pressure.

Figure 4.33: DPC vs. time in several lab DTS tests of 2019 at 30 psi inflation pressure.

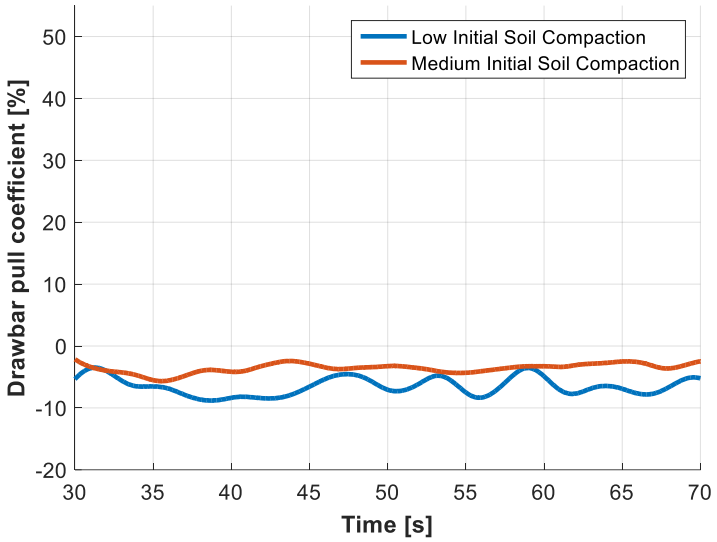

(a) Low and medium initial soil compaction, 30 psi inflation pressure, and 5 kN normal load.

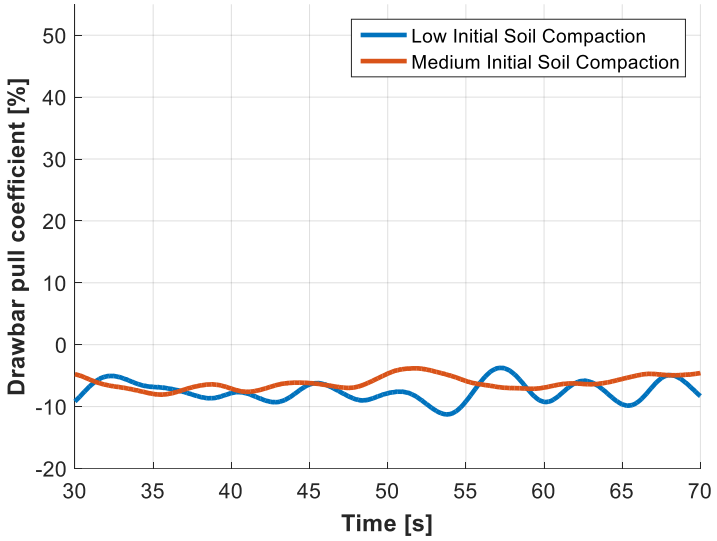

(b) Low and medium initial soil compaction, 42 psi inflation pressure, and 5 kN normal load.

Figure 4.34: DPC vs. time in several lab free-rolling tire-soil tests of 2019. DPC is negative because the tire is free rolling on soil and bearing motion resistance.

From Figure 4.34 it can be seen that the fluctuation amplitude at low initial soil compaction level is higher than that at medium initial soil compaction for both 30 psi and 42 psi inflation pressure in the towing mode. The fluctuation (ripple) of tire drawbar pull (coefficient) and rut bottom remains to be a complex phenomenon; the variation in soil condition and shearing properties of soil might combine to affect such fluctuation. More

experiments and modeling need to be completed to investigate this phenomenon.

4.5.2.4 Tire Performance and Soil Response in Towing Mode

The extracted measured data of motion resistance (the drawbar bull if being negative), normal load, wheel rotation angle, wheel longitudinal velocity, rut depth, from the laboratory free-rolling tire-soil tests in 2019, was post-processed. Motion resistance coefficient was obtained by dividing the measured motion resistance by the normal load measured at the same moment. Rolling radius was calculated as the ratio of the wheel longitudinal velocity over the wheel rotation angular speed which was computed by using the wheel rotation angle and sampling time. Motion resistance coefficient, motion resistance, rolling radius, and rut depth were plotted against the operation parameters, as displayed in Figure 4.35, Figure 4.36, Figure 4.37, and Figure 4.38.

As shown in Figure 4.35a, Figure 4.35c, and Figure 4.35e, by increasing the inflation pressure, motion resistance coefficient increases slightly while maintaining the same normal load and same initial soil compaction. The increase in tire inflation pressure leads to more penetration of the tire into the soil (larger tire sinkage) and hence leads to larger contact pressure (reaction pressure) from the soil. Also, larger tire sinkage could result in a bigger area of the soil being compacted in front of the lowest point of the tire-soil contact area, which, together with the larger reaction pressure from the soil, will increase the compaction resistance.

Figure 4.36a, Figure 4.36c, and Figure 4.36e illustrate the effect of inflation pressure on the tire rolling radius. It can be found that rolling radius tends to increase with inflation pressure. In [18] there is a positive correlation between the rolling radius and the loaded radius in on-road conditions. This correlation could also hold for a tire on soft soil according to [11]. Assuming this positive correlation between the rolling radius and loaded radius, the loaded radius increases with inflation pressure at the same initial soil compaction, so the rolling radius increases as well.

Figure 4.36 clearly shows that, at low initial soil compaction, the rolling radius is larger

than the unloaded radius, and that, at medium initial soil compaction, the rolling radius is only larger than the unloaded slightly at 42 psi inflation pressure. Comparing the measured rolling radius in Figure 4.36 with the estimated rolling radius in Table 4.8, at the high and medium initial soil compaction and 5 kN normal load, the error of estimation is around 3 mm (around 0.9% relative error) and 4.6 mm (1.36% relative error); at the low initial soil compaction, the estimation completely goes too much off the measured value which is larger than the unloaded radius, while Equation (4.2) gives an estimated rolling radius smaller than the unloaded radius. It can be concluded that the estimation method for rolling radius works acceptably for the high and medium initial soil compaction, 5kN normal load, and low tire longitudinal speed and tends to give more accurate estimation as the soil gets more compacted (harder). This could be due to the fact that the schematic about the geometry of tire-soil contact patch in Figure 4.10 is more like the real geometry of tire-soil contact patch as the soil gets harder. However, the estimation method is totally incapable at the low initial soil compaction possibly because the schematic in Figure 4.10 cannot represent the real geometry of tire-soil contact patch at the low initial soil compaction.

Figure 4.38 shows the influence of tire inflation pressure on the rut depth: the rut depth increases with the inflation pressure. Average ground pressure on soil increases with the inflation pressure, similar to the hard ground case, which could be imagined as the soil at infinitely high soil compaction level, represented by Figure 4.9; as a result, the larger average ground pressure leads to a higher value of tire sinkage and hence a higher value of rut depth.

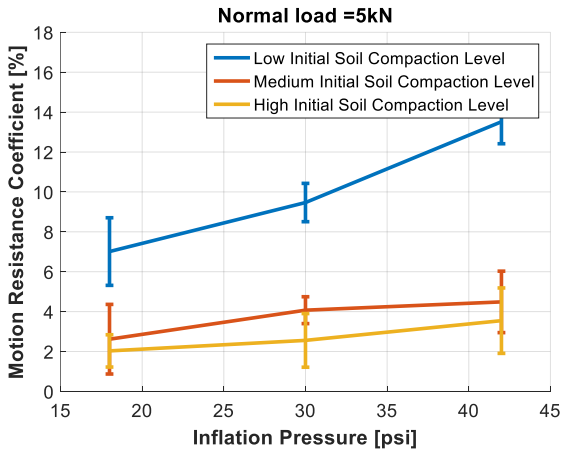

(a) Motion resistance coefficient at 5 kN normal load.

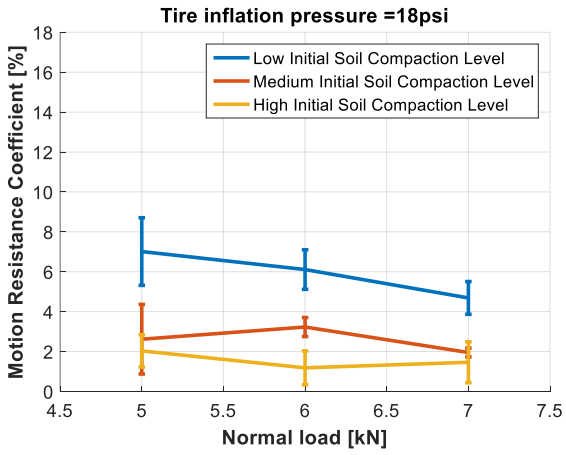

(b) Motion resistance coefficient at 18 psi inflation

pressure.

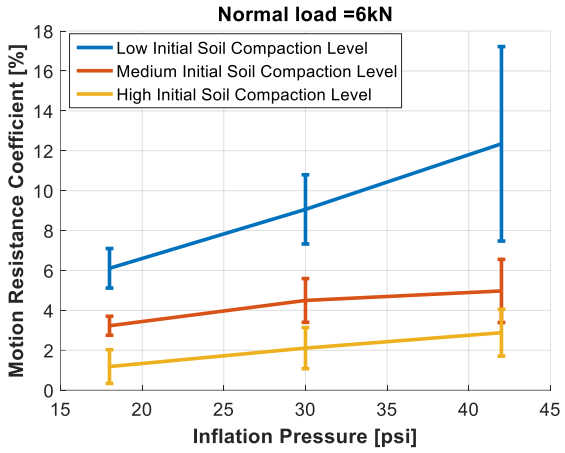

(c) Motion resistance coefficient at 6 kN normal load.

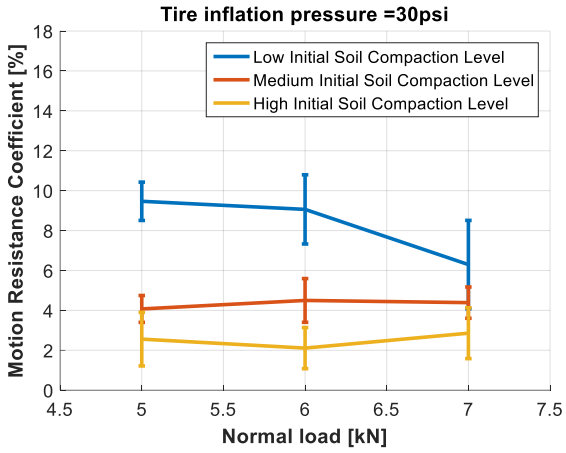

(d) Motion resistance coefficient at 30 psi inflation pressure.

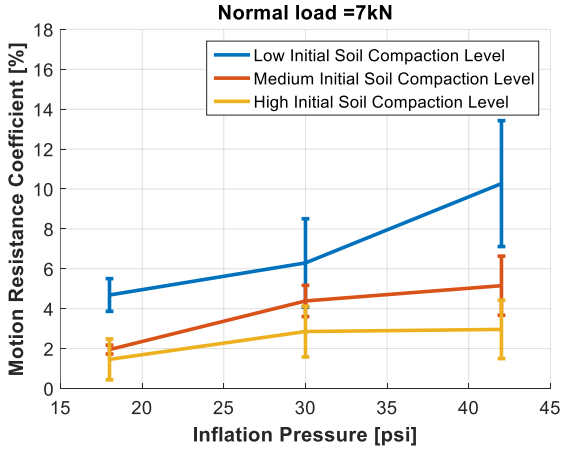

(a) Motion resistance coefficient at 7 kN normal load.

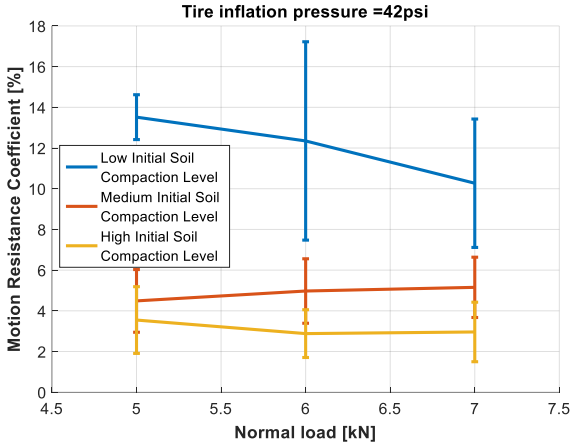

(b) Motion resistance coefficient at 42 psi inflation pressure.

Figure 4.35: Measurement data of motion resistance coefficient from the lab free-rolling tire-soil tests.

A coupling effect of initial soil compaction and inflation pressure can also be seen from Figure 4.35, Figure 4.37, and Figure 4.38. Compared with the soil at the medium or high level of initial compaction, the increase in tire inflation pressure at low initial soil compaction results in a larger increase in motion resistance coefficient. Also, as the initial soil compaction decreases, with the same increase in inflation pressure, the rise in rolling radius or rut depth becomes larger. This coupling effect is possibly due to the fact that, when the soil is more compacted, the soil tends to be less susceptible to more tire penetration and to more hinder the tire loaded radius (and hence the rolling radius) from going larger

(remember the positive correlation between the loaded radius and rolling radius as described previously).

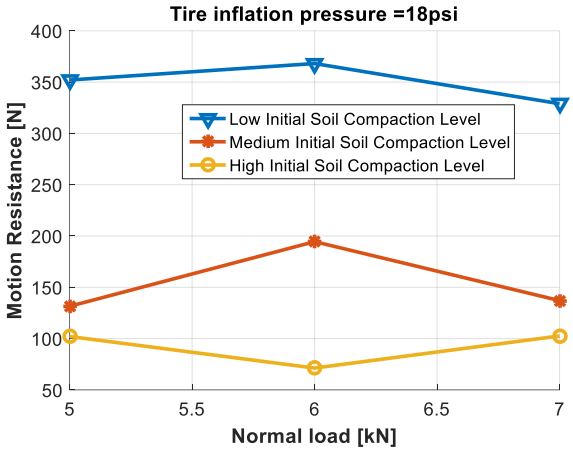

(a) Motion resistance at 18 psi inflation pressure.

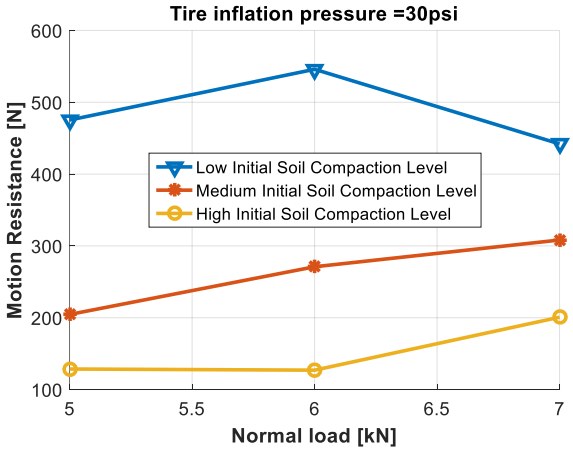

(b) Motion resistance at 30 psi inflation pressure.

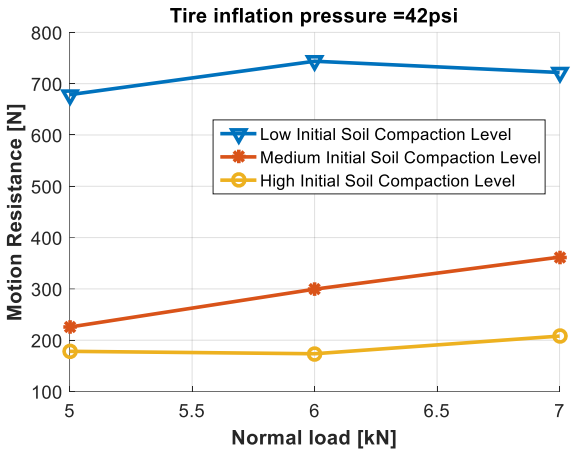

(c) Motion resistance at 42 psi inflation pressure.

Figure 4.36: Measurement data of motion resistance from the lab free-rolling tire-soil tests.

There is a reduction in the rolling radius when changing the initial soil compaction from the low to high level (see Figure 4.37). The amount of reduction in the rolling radius is much larger from the low initial soil compaction level to the medium one than that from the medium to the high compaction level. From Figure 4.35, the motion resistance coefficient decreases with an increase in the initial soil compaction. Similar to the effect of initial soil compaction level on the tire rolling radius, there is a larger difference between the motion resistance coefficients when the initial soil compaction changes from the low to medium level than changing from the medium to high level. A similar decreasing trend in the change of rut depth can be also observed from Figure 4.38 when the initial soil compaction level increases.

An explanation about the decreasing trend in the rolling radius, motion resistance coefficient, and rut depth when the initial soil compaction level changes is as follows: as the initial soil compaction increases, at the same inflation pressure and normal load, the tire is more like running on hard ground. As a result, the tire loaded radius is reduced, so are the rut depth and compaction resistance. With the aforementioned positive correlation between the loaded radius and rolling radius, the rolling radius decreases with the increase in initial soil compaction level. Also, a reduction in compaction resistance results in a decrease in motion resistance coefficient.

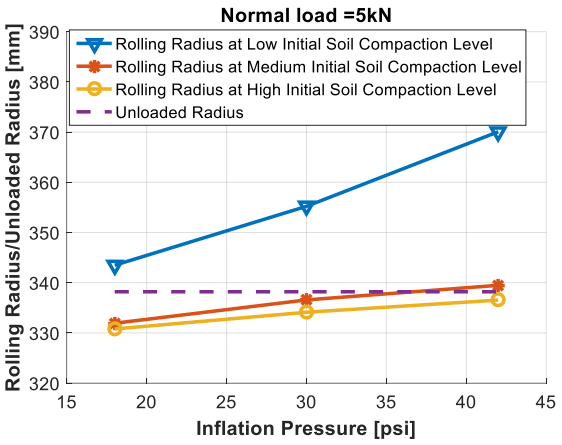

(a) Rolling radius at 5 kN normal load.

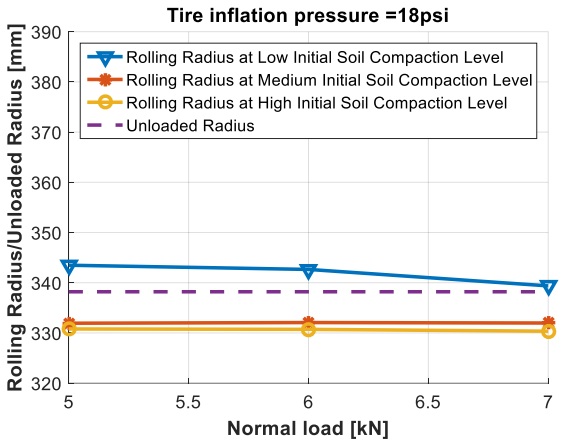

(b) Rolling radius at 18 psi inflation pressure.

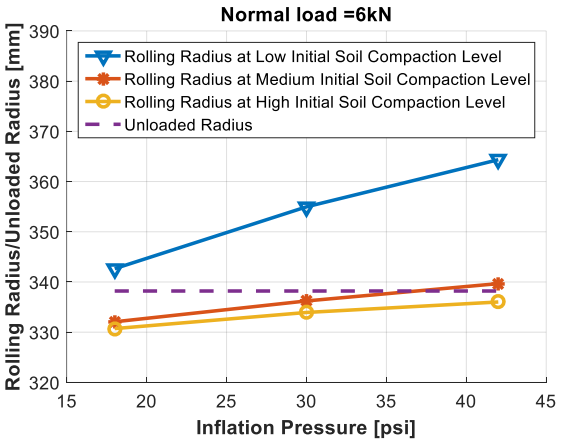

(c) Rolling radius at 6 kN normal load.

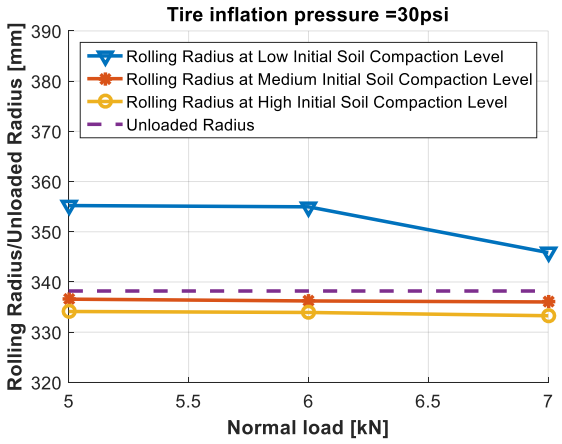

(d) Rolling radius at 30 psi inflation pressure.

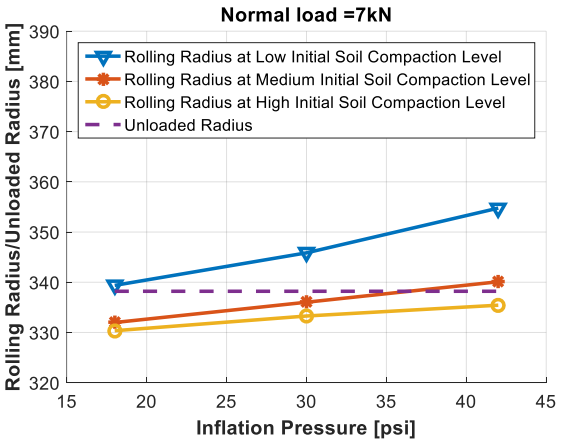

(a) Rolling radius at 7 kN normal load.

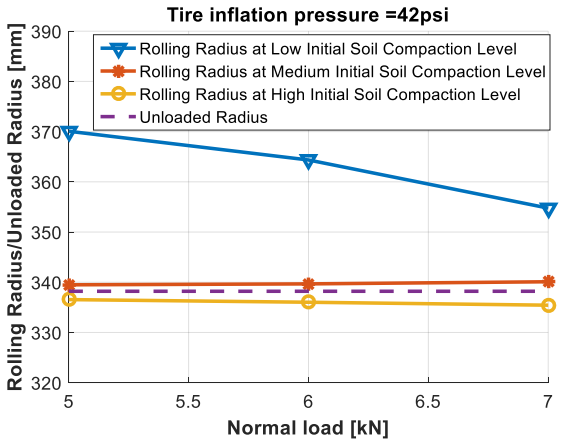

(b) Rolling radius at 42 psi inflation pressure.

Figure 4.37: Measurement data of rolling radius from the lab free-rolling tire-soil tests.

It is illustrated in Figure 4.37 and Figure 4.38 that an increase in normal load leads to a slight increase or no change in rut depth and a slight decrease (at low initial soil compaction level) or no change (at medium or high initial soil compaction level) in rolling radius. The reason for the former trend in rut depth is possibly that the average ground pressure on soil could increase very faintly with normal load, similar to the hard ground case in Figure 4.9. Such small increase in average ground pressure with normal load hardly or slightly raises the tire sinkage and hence the rut depth. As a result, the area of the soil being compacted in front of the lowest point of the tire-soil contact area hardly or slightly grows bigger with the increase in normal load, which leads to small increase or no change in motion resistance and hence no change or small decrease (at low initial soil compaction) in motion resistance coefficient, illustrated by Figure 4.36 and Figure 4.35 respectively.

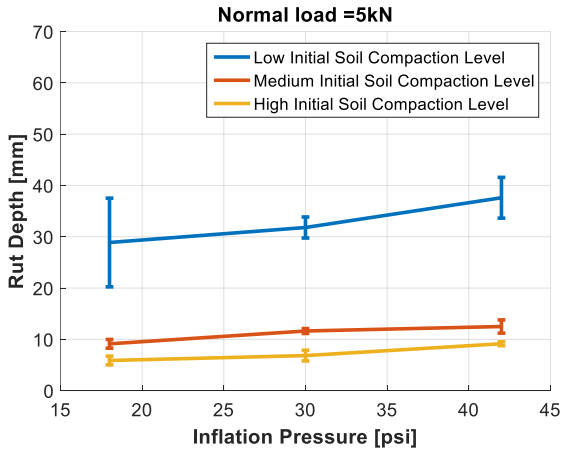

(a) Rut depth at 5 kN normal load.

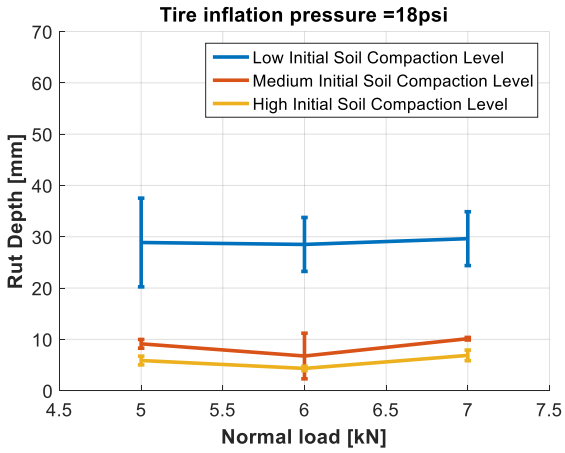

(b) Rut depth at 18 psi inflation pressure.

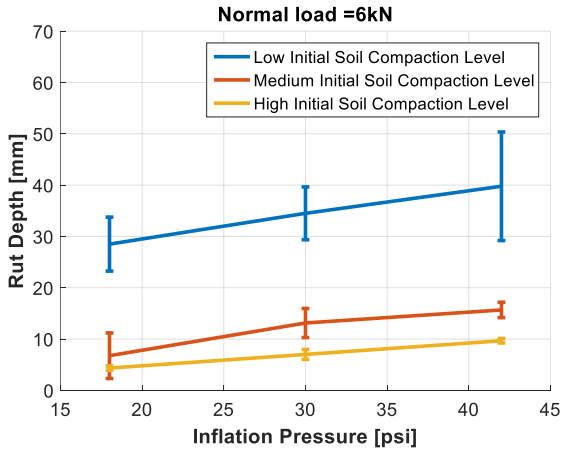

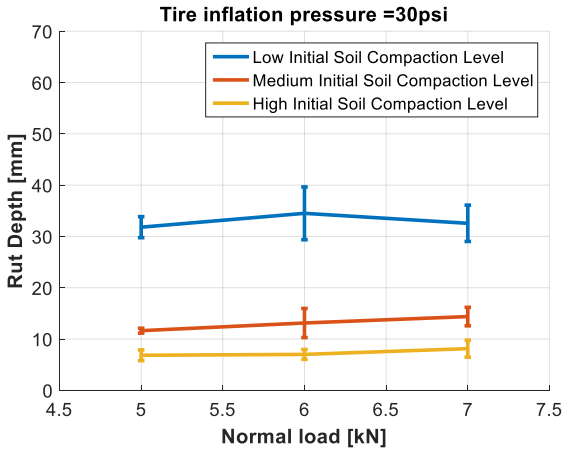

(c) Rut depth at 6 kN normal load.

(d) Rut depth at 30 psi inflation pressure.

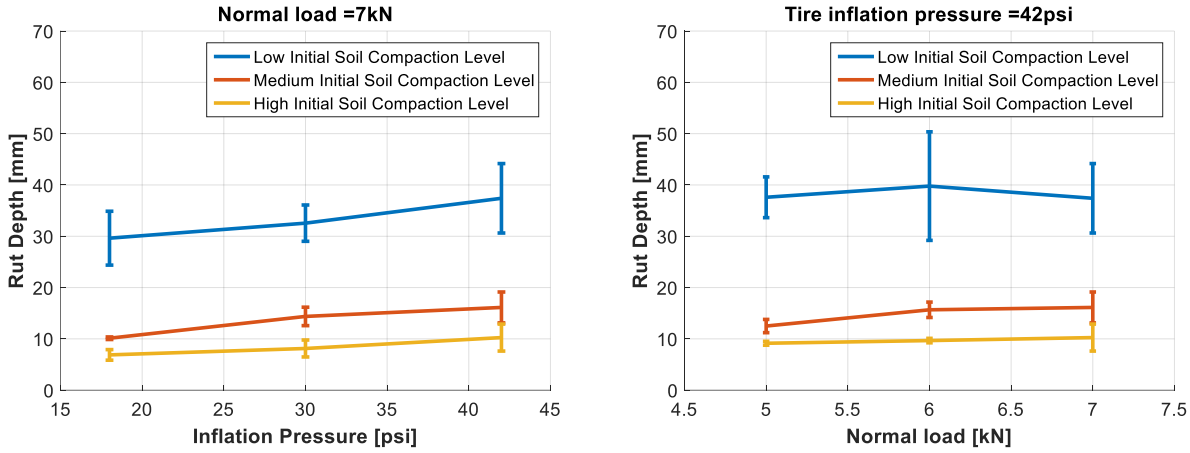

(a) Rut depth at 7 kN normal load.

(b) Rut depth at 42 psi inflation pressure.

Figure 4.38: Measurement data of rut depth from the lab free-rolling tire-soil tests.

As a short summary, the effect of tire normal load seems minor compared with the effect of tire inflation pressure, though both seemed secondary to the effect of initial soil compaction. Clear and uniform trend in the change of motion resistance coefficient, rut depth, and rolling radius w.r.t. initial soil compaction and inflation pressure can be found from Figure 4.35, Figure 4.37, and Figure 4.38, while as for the change of motion resistance coefficient, rut depth, and rolling radius, no clear and uniform trend can be found from those figures. The change in tire normal load marginally changes the tire average ground pressure which heavily influences the rut depth and motion resistance coefficient, while the change in inflation pressure changes more. This could make the normal load less influential, compared with the tire inflation pressure.

4.5.2.5 Tire Tractive Performance and Soil Response in Traction Mode

The extracted measured data of drawbar pull, normal load, and rut depth, from the laboratory dynamic tire-soil tests in 2017, was post-processed. The measured DP was divided by the measured actual normal load to obtain drawbar pull coefficient (DPC). The actual slip ratios were calculated in the way as described in Section 4.5.2.2. All the values of the DPC and actual slip ratios were averaged for each test, i.e., for each combination of the nominal slip ratio level and tire inflation pressure level. The average values of the DPC were plotted

against the average values of their corresponding actual slip ratios, as shown in Figure 4.39.

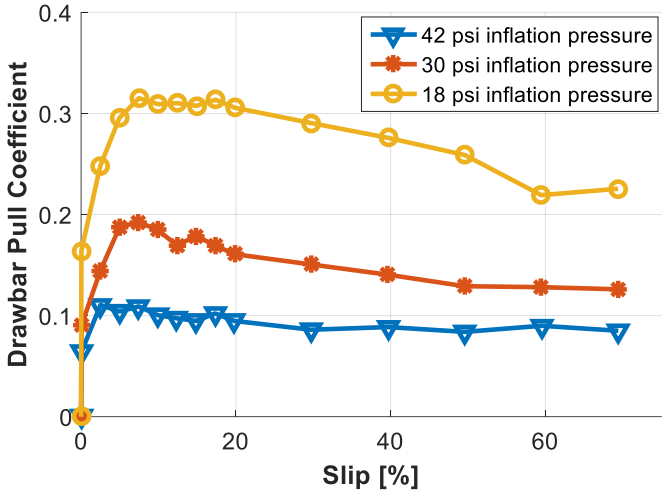

Figure 4.39: Variations in DPC with slip. The measured data is from the lab DTS tests of 2017.

In the unstable region (the region to the right of the maximum DP), DPC decreases slightly with the slip, possibly due to the increase in the compaction resistance and in the bulldozing resistance with the slip ratio. A higher slip ratio leads to a higher tire slip sinkage, hence a higher tire sinkage. The higher tire sinkage might lead to larger bulldozing effect, as there would be more soil being in contact with the front arc of the tire and pushed forward. This might result in a larger bulldozing resistance. On the other hand, the higher dynamic tire sinkage might mean more vertical work done to push the soil in contact with the tire downward, which might bring a larger compaction resistance. The gross tractive force might saturate at a high slip ratio according to some tire off-road traction model [78]. Therefore, the saturation of the gross tractive force, the increase in the compaction resistance with slip, and the increase in the bulldozing resistance with slip all together cause the slight decrease in the DPC with the increase in slip ratio. The trend of the experimental DPC vs. slip relationship observed in the lab DTS tests of 2017 is similar to the trend of the curve out of Magic Formula tire model (seen in [81], [85]) with a certain set of model parameters and the trend of DP vs. slip curve for moist loam [13] obtained by using the Sanatore and Sandu semi-empirical tire model.

Theoretically, at zero slip, assuming zero gross tractive force, the DP should be negative because of the compaction resistance, bulldozing resistance, and internal motion resistance.

However, in the lab DTS tests of 2017, at zero nominal slip ratio, Figure 4.39 shows that the drawbar pull was positive, this means the rolling radius evaluated in the lab STS tests of July 2017 was smaller than the rolling radius of the test tire in the lab DTS tests of 2017 (the former was taken as the approximate of the latter, as described in Section 4.5.1). Even though the CI and VWC of the test soil in the lab DTS tests of 2017 is close to that of the test soil at the low soil compaction level in the lab STS tests of 2017 (see Table 4.6 and Table 4.9), due to the inhomogeneous property of the soil and the difficulty in repeating the same soil condition by the adopted soil preparation method, there could be slight differences in the soil condition between the lab DTS tests of 2017 and the lab STS tests of 2017, especially at low initial soil compaction level. Also, there is a difference between the true tire-soil contact patch and the one depicted by Figure 4.10 based on which the loaded radius-rolling radius relationship was derived. These aforementioned differences caused the rolling radii evaluated in the lab STS tests of 2017 to be smaller than the ones in the lab DTS tests of 2017. The rolling radius used in a field DTS test conducted by Lee and Kim was also smaller than the true rolling radius, as the tractive coefficient (DPC) measured at zero slip was also very small but positive [27], like the ones shown in Figure 4.39.

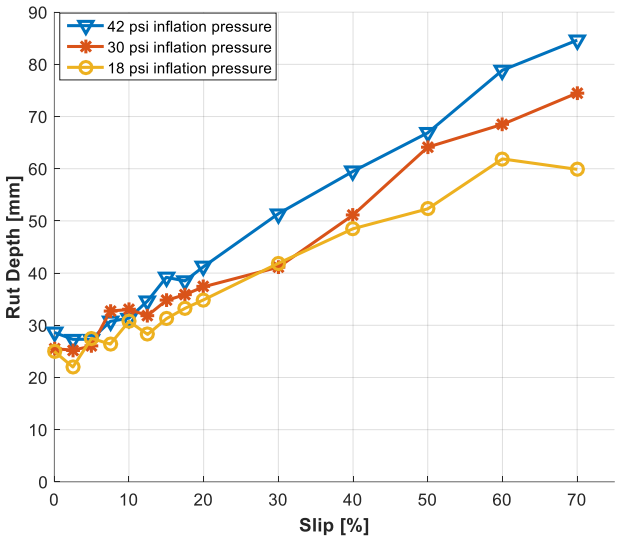

Figure 4.40: Variations of rut depth with slip for all three levels of tire inflation pressure. The measured data is from the lab DTS tests of 2017.

The influence of tire inflation pressure on DPC is illustrated by Figure 4.39d and Figure 4.41a. At the same slip ratio, the higher the tire inflation pressure, the lower the DPC is. This

trend might be related to the possible increase in the tire-soil contact patch area with a decrease in the tire inflation pressure that boosts the tractive effort developed in the contact area and hence the drawbar pull. Also, a decrease in tire inflation pressure leads to a decrease in tire sinkage as well as in the area of the tire-soil contact patch portion just in front of the lowest point of the tire, as explained in Section 4.5.2.4. Because of this, the bulldozing resistance and the compaction resistance both could decrease, which boosts the drawbar pull as well.

The eight measurements of the rut depth as mentioned in Section 4.5.1 were averaged to obtain the rut depth for each nominal slip ratio level. The rut depth vs. nominal slip ratio , obtained from the lab DTS tests of 2017, was plotted in Figure 4.40. According to Figure 4.40, except for a few isolated points, the rut depth increases with the slip ratio, in accordance with the trend predicted theoretically by [26], and at the same slip ratio, it also increases with the tire inflation pressure. The latter trend can be more clearly seen in Figure 4.41b where the vertical coordinate of each point is the average of the vertical coordinates of all the points along the corresponding broken line in Figure 4.40. When the tire inflation pressure goes higher, with the normal load remaining the same, the tire behaves more like a rigid wheel and hence might bring larger tire sinkage. This contributes to the increase in the rut depth with tire inflation pressure.

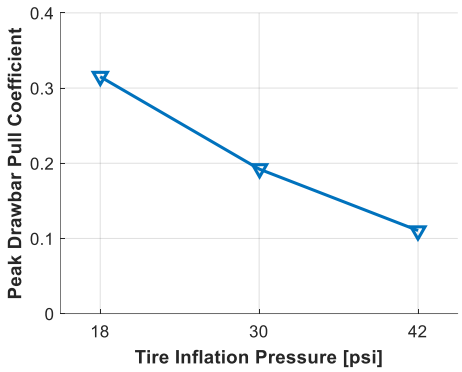

(a) Peak DPC vs. tire inflation pressure.

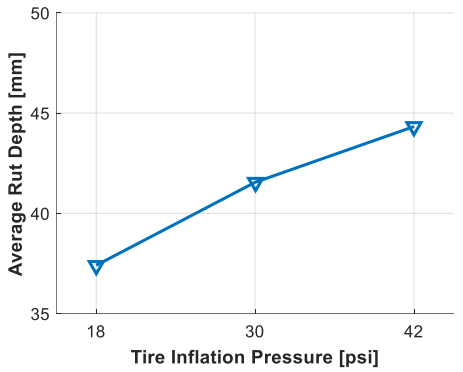

(b) Average rut depth vs. tire inflation pressure.

Figure 4.41: Influence of tire inflation pressure on the rut depth and tire peak drawbar pull coefficient at low initial soil compaction level. The measured data is from the lab DTS tests of 2017.

It's worth mentioning that the rut depth measured in the lab DTS tests of 2017 refers to the vertical distance between the rut shoulder and the nearest local trough of the rut at the

location of the measurement. Also, rut depth is not necessarily equal to tire sinkage, although, like the rut depth, the tire sinkage is found to also increase with slip ratio experimentally [127]. In the tire or wheel off-road dynamic modeling, the tire sinkage or the wheel sinkage is slightly larger than the rut depth, occasionally, the former is deemed equal to the latter [87], [14].

Also, the extracted measured data of drawbar pull, normal load, wheel torque, wheel rotation angle, rut depth, rut width, and tire sinkage, from the laboratory dynamic tire-soil tests in 2019, was post-processed. The means values of DPC and rut depth were obtained the same way as that for the lab DTS tests of 2017; similarly, the mean values of rut width was obtained. The measured data of wheel torque, drawbar pull, and wheel rotation speed (computed from the wheel rotation angle) was substituted into Equation (4.8) to obtain drawbar efficiency. Note that T is motor torque which should be slightly higher than the measured wheel torque, so the drawbar efficiency obtained this way (in which the motor torque is approximated by the wheel torque) should be slightly higher than the true value. Actual slip ratios were calculated by using the Equation (2.1), the measured wheel rotation speed, and the rolling radius presented in Table 4.11. Mean values of these tire performance parameters and soil response parameters are plotted against their corresponding mean values of actual slip ratios in all the figures that will come next in this section.

$$\eta = \frac{DP \cdot V_x}{T \cdot \omega_w} \tag{4.8}$$

As discussed in Section 4.5.2.4, the rolling radius estimation method proposed in Section 4.4.1 didn't work well for the low initial soil compaction level. However, back to 2017, there was no better choice than applying this estimation method for the lab DTS tests of 2017 as the Terramechanics Rig was not capable of testing a tire in towing mode. To correct the strayed slip ratios obtained by using the result of this estimation method, the rolling radius (see Figure 4.37), measured at the 5 kN normal load; 18, 30, and 42 psi inflation pressure; and low initial soil compaction level, was used to recalculate the actual slip ratios for the lab DTS tests of 2017. These corrected slip ratios are presented in Figure 4.42a, Figure 4.43a, and Figure 4.44a.

The DPC vs slip curves for all three levels of initial soil compaction share the same trend, when the inflation pressure changes, as described in the 4th paragraph of this section. At the same inflation pressure and normal load, DPC tends to rise with an increase in initial soil compaction level. When the initial soil compaction level increases at the same inflation pressure, the tire dynamic sinkage is reduced, similar to that if the inflation pressure decreases while the initial soil inflation pressure remains the same; consequently, the compaction resistance and bulldozing resistance decrease as explained previously. So the motion resistance drops down. On the other hand, the contact area decreases with the increase in initial soil compaction level, similar to the trend of rut area in Section 4.4.3.2; given the same normal load, as a result, the average ground pressure increases. Also, with our soil being the sandy and dry soil, the soil cohesion and friction angle could increase with the initial soil compaction [139], which, together with a boosted average ground pressure, leads to a larger shear strength. According to shear stress-shear displacement model, such as Equation (2.27), the tractive effort, computed as the integration of the longitudinal component of shear over the contact area, could increase because of a larger shear strength, although the contact area decreases. So the boosted tractive effort and reduced motion resistance cause the DP or DPC to rise when the initial soil compaction level increases at the same normal load and inflation pressure.

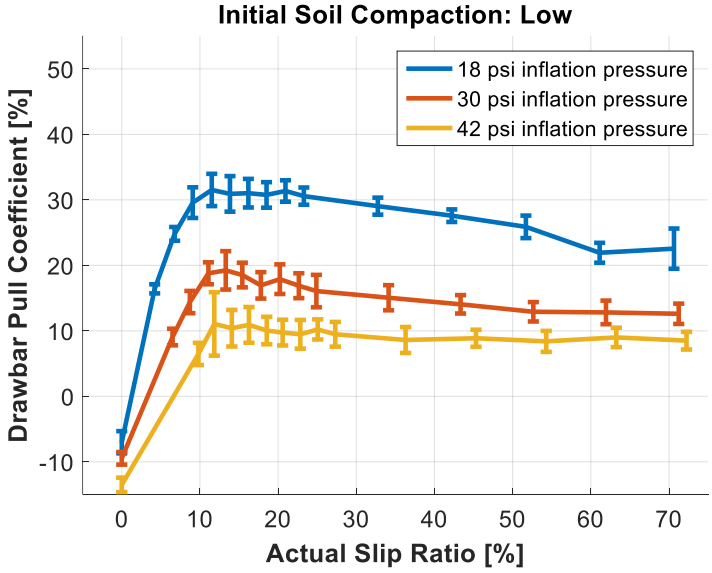

(a) DPC vs. slip at low initial soil compaction. The actual slip here was calculated using the rolling radius obtained from the lab free-rolling tire-soil tests, different from that in Figure 4.39. Except for the data points from

the lab free-rolling tire-soil tests, the rest of the data points here have the same DPC values as the corresponding data points in Figure 4.39.

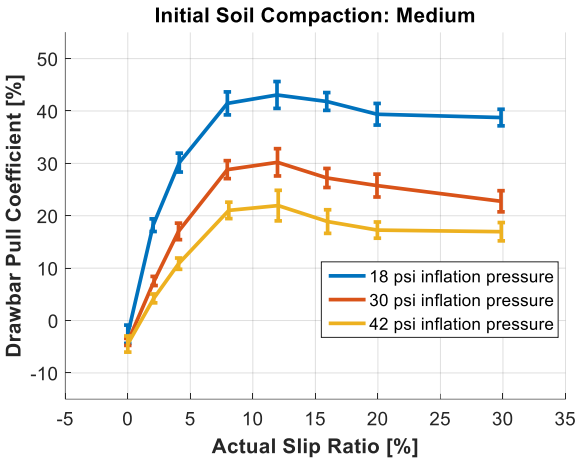

(b) DPC vs. slip at medium initial soil compaction.

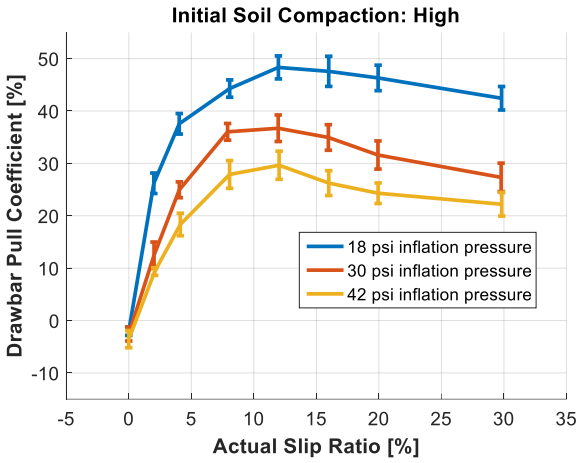

(c) DPC vs. slip at high initial soil compaction.

Figure 4.42: Variations in drawbar pull coefficient with slip ratio at 5 kN normal load; 18, 30, and 42 psi inflation pressure; and low, medium, and high initial soil compaction. The measured data is from the lab DTS tests of 2017 and 2019.

Also, clearly seen from Figure 4.42, if the initial soil compaction is higher, while the inflation pressure and normal load remain constant, the initial slope of the DPC vs slip curve in the stable region, peak drawbar pull coefficient, and the asymptotic drawbar pull coefficient are higher. This feature of DPC vs slip curves for various levels of initial soil compaction could be applied to develop algorithms for the estimation of soil compaction, similar to the slip-slope based approach to friction estimation [140], [18]

Figure 4.42 shows that the optimal slip ratio for the peak DPC is around 12%, regardless of initial soil compaction level and inflation pressure level. By contrast, the optimal slip ratio for the peak DE, smaller than the 12% optimal slip ratio for the peak DPC, shifts to the left with a decrease in inflation pressure or an increase in initial soil compaction level, as shown in Figure 4.43. It seems that a decrease in motion resistance leads to an increase in drawbar efficiency because less proportion of the motor input power is wasted in getting over the motion resistance. This explains why the drawbar efficiency is boosted when the inflation pressure is lowered with the same initial soil compaction; or when the initial soil compaction is increased from the low to the medium with the same inflation pressure.

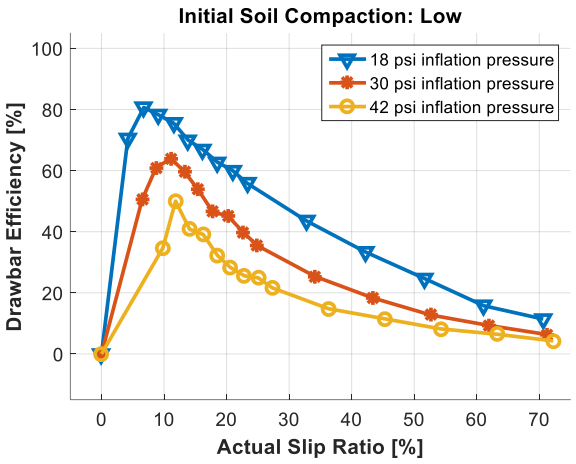

(a) Drawbar efficiency vs. slip at low initial soil compaction.

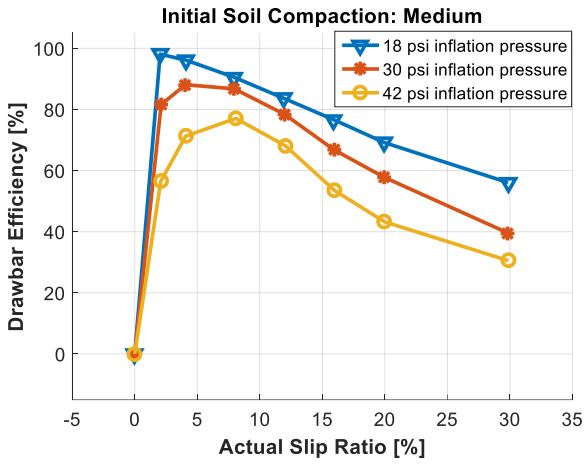

(b) Drawbar efficiency vs. slip at medium initial soil compaction.

Figure 4.43: Variations in drawbar efficiency with slip ratio at 5 kN normal load; 18, 30, and 42 psi inflation pressure; and low and medium initial soil compaction. Drawbar efficiency is assumed to be zero at zero slip ratio. The measured data is from the lab DTS tests of 2017 and 2019.

Except for a few isolated points, the rut depth vs slip curves in Figure 4.44 share the same trend, as described in the 5th paragraph of this section, when the inflation pressure changes at the same slip ratio and initial soil compaction level; the same trend also applies to the tire sinkage vs slip curves in Figure 4.45. At positive slip ratios, both of the rut depth and tire sinkage increases with slip ratio, which results from the slip sinkage effect.

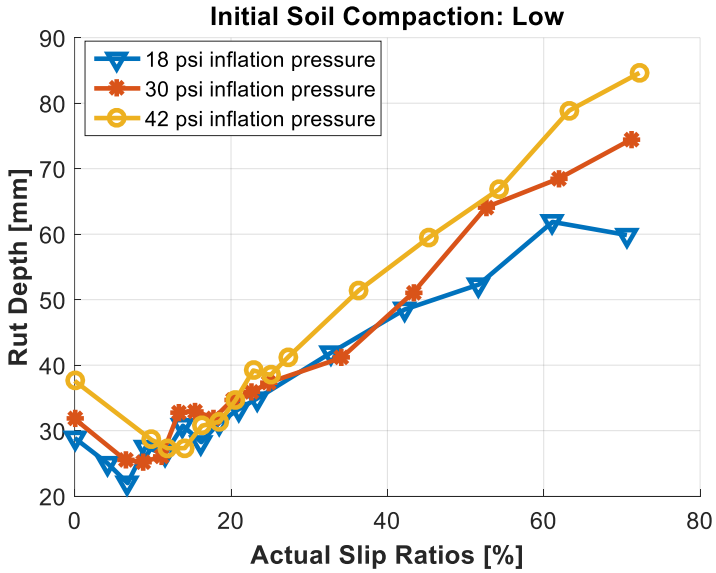

(a) Rut depth vs. slip at low initial soil compaction. The actual slip here was calculated using the rolling radius

obtained from the lab free-rolling tire-soil tests, different from that in Figure 4.40. Except for the data points from the lab free-rolling tire-soil tests, the rest of the data points here have the same rut depth values as the corresponding data points in Figure 4.40.

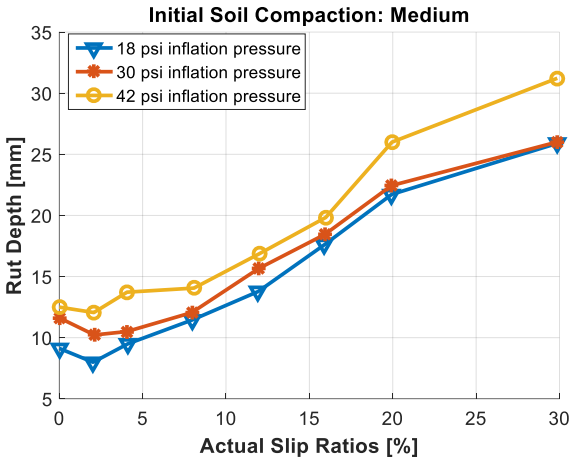

(b) Rut depth vs. slip at medium initial soil compaction.

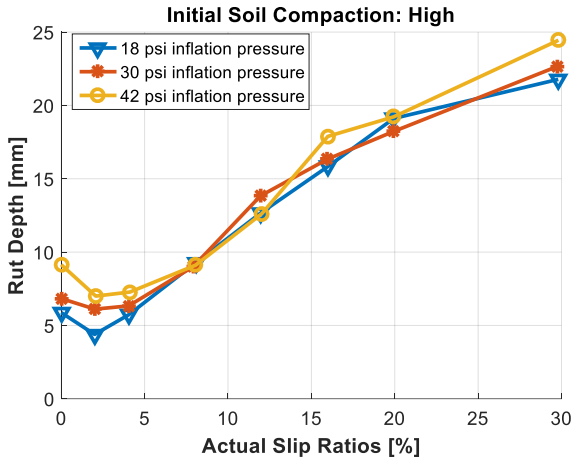

(c) Rut depth vs. slip at high initial soil compaction.

Figure 4.44: Variations in rut depth with slip ratio at 5 kN normal load; 18, 30, and 42 psi inflation pressure; and medium and high initial soil compaction. The measured data is from the lab DTS tests of 2017 and 2019.

Also, due to the slip sinkage effect, as the slip ratio goes higher, the tire dynamic sinkage increases, meaning a larger area of tire-soil contact patch in both longitudinal and lateral directions; hence, the contact patch length and rut width also increases with the slip ratio, as illustrated in Figure 4.46 and Figure 4.47.

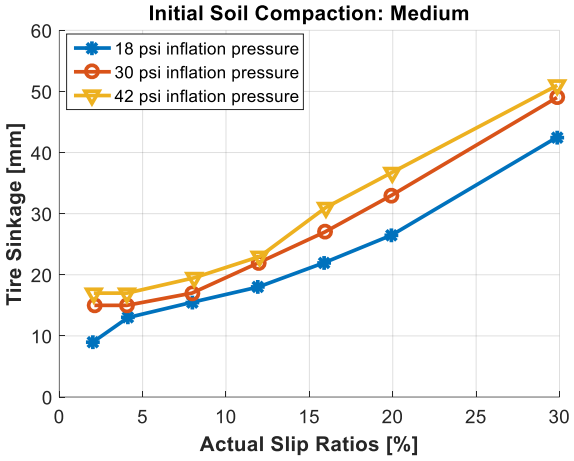

(a) Tire sinkage vs. slip at medium initial soil compaction.

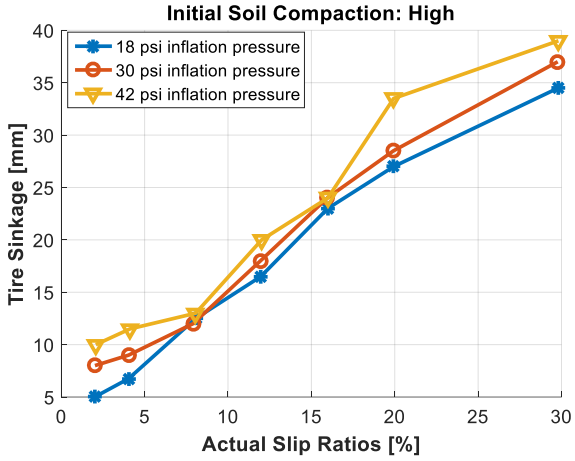

(b) Tire sinkage vs. slip at high initial soil compaction.

Figure 4.45: Variations in tire sinkage with slip ratio at 5 kN normal load; 18, 30, and 42 psi inflation pressure; and medium and high initial soil compaction. The measured data is from the lab DTS tests of 2019.

Comparing the rut depth at zero slip (in the free-rolling mode) with the rut depth at next few slip ratios after zero in Figure 4.44, a convex valley can be found of the variation in rut depth with an increase in slip ratio. A possible explanation for this convex valley is stated here. When the slip ratio rises from zero and yet is still small, the slip sinkage effect is not dominant; some soil is displaced by the tire to the rear of the tire due to the shearing in the tire-soil contact patch, and hence the depth of the rut formed at the back of the tire decreases first with the increase of slip ratio. When the slip ratio gradually becomes sufficiently big, the slip sinkage effect is dominant; consequently the tire sinkage is reduced considerably. Although the soil keeps being displaced to the rear of the tire where the rut forms, the reduced soil sinkage cannot be compensated, and hence depth of the rut increases with the slip ratio next.

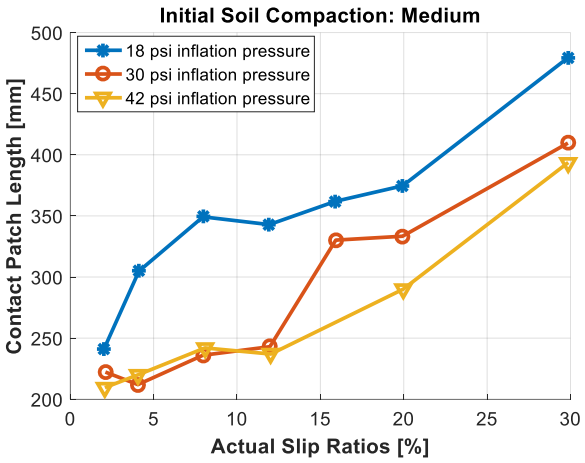

(a) Contact patch length vs. slip at medium initial soil compaction.

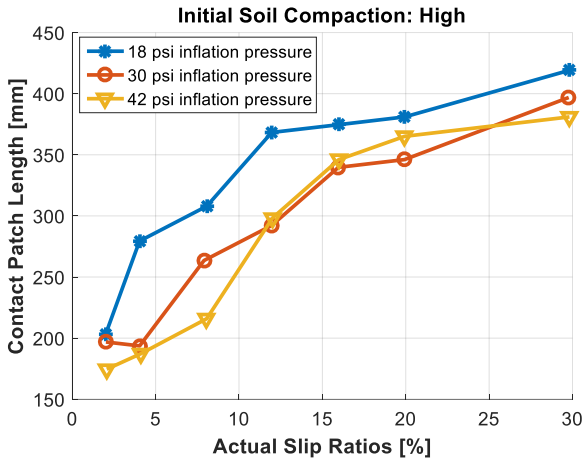

(b) Contact patch length vs. slip at high initial soil compaction.

Figure 4.46: Variations in contact patch length with slip ratio at 5 kN normal load; 18, 30, and 42 psi inflation pressure; and medium and high initial soil compaction. The measured data is from the lab DTS tests of 2019.

Except for a few isolated points, Figure 4.46 and Figure 4.47 show that the contact patch length increase with a decrease in inflation pressure, which could be explained with the reason that accounts for the same trends in Section 4.4.3.2. Unlike the trend of the rut width in Section 4.4.3.2, the rut width at positive slip ratios rises with a reduction in inflation pressure. This trend only happens in the dynamic tire-soil tests not in the static tire-soil tests

because of the slip sinkage effect in the former. Under the slip sinkage effect, the sinkage is relatively larger compared with the sinkage in the static tire-soil tests; as a result, the sidewall is in touch with the soil. The sidewall tends to bulge laterally as the inflation pressure is lowered, which increases the rut width. The rut depth, tire sinkage, contact patch length, and rut width are reduced if the initial soil compaction level rises, the same trends as that in Section 4.4.3.2, due to less sinkage and less contact area of the tire tread, shoulder, side wall, and soil allowed by the more compacted soil.

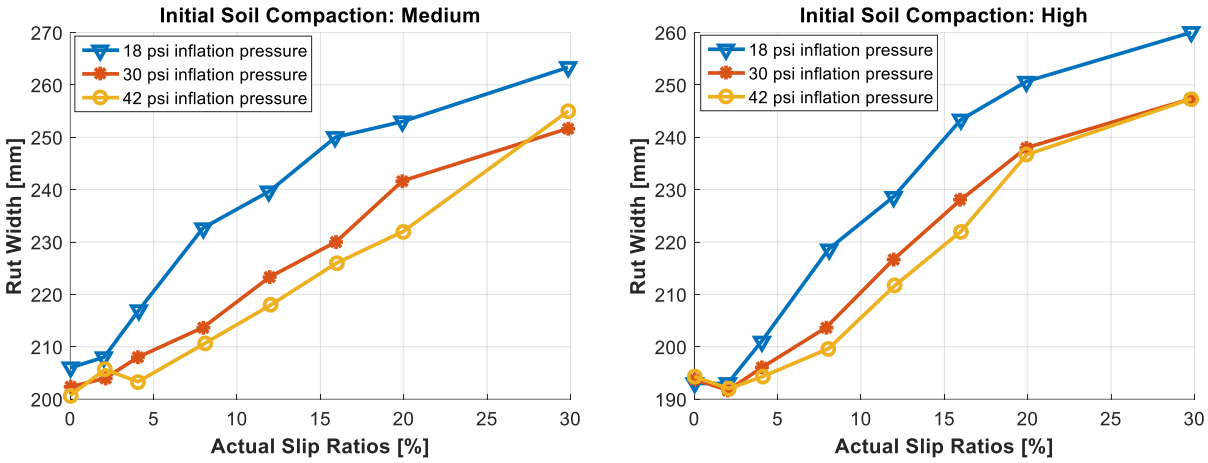

(a) Rut width vs. slip at medium initial soil compaction.

(b) Rut width vs. slip at high initial soil compaction.

Figure 4.47: Variations in rut width with slip ratio at 5 kN normal load; 18, 30, and 42 psi inflation pressure; and medium and high initial soil compaction. The measured data is from the lab DTS tests of 2019.

4.5.2.6 Multi-Pass Effect

The extracted measured data of drawbar pull, normal load, wheel torque, wheel rotation angle, rut depth, tire sinkage, and cone index, from the laboratory multi-pass tire-soil tests in 2019, was post-processed. The lab multi-pass tire-soil tests are divided into the tests in the towing mode and the tests in the traction mode. The extracted measured data from these two types of multi-pass tests was post-processed in the same ways as explained in Section 4.5.2.4 and 4.5.2.5. The tire performance parameters and soil response parameters of interest are plotted against the number of passes for the tests in towing mode and against the actual slip ratios for all three passes of the tests in traction mode, as shown in the figures that will show

up next in this section

Figure 4.48 clearly indicates that the motion resistance coefficient and rolling radius decrease after each pass, at rates that lowers down with the increase in number of passes. The soil could become less susceptible to the compaction brought by the tire traffic one pass after another, which possibly accounts for the decreasing reduction rate of motion resistance coefficient or rolling radius w.r.t. number of passes.

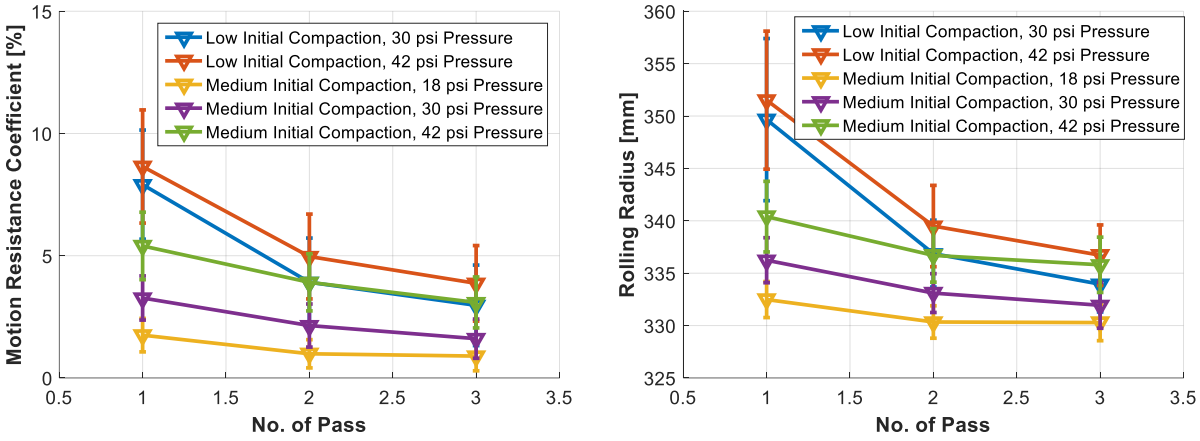

(a) Variation in motion resistance coefficient with number of passes.

(b) Variation in rolling radius with number of passes.

Figure 4.48: Multi-pass effect on the tire performance in the towing mode.

By contract, from Figure 4.49, the cone index, rut depth, and tire sinkage increase with the number of passes. At the same inflation pressure and initial soil compaction level, the growth rate of cone index, rut depth, or tire sinkage w.r.t. the number of passes seems fairly constant. At low initial soil compaction level, the growth rate of cone index w.r.t. the number of passes is larger than that at medium initial soil compaction level, as illustrated by Figure 4.49a; this could be due to the fact that the soil in the former case has more space among soil particles to be compacted than the soil in the latter case does.

The trend for the motion resistance coefficient, cone index, rut depth when the number of passes increases is in general agreement with classical studies on the multi-pass effect such as [141], [142].

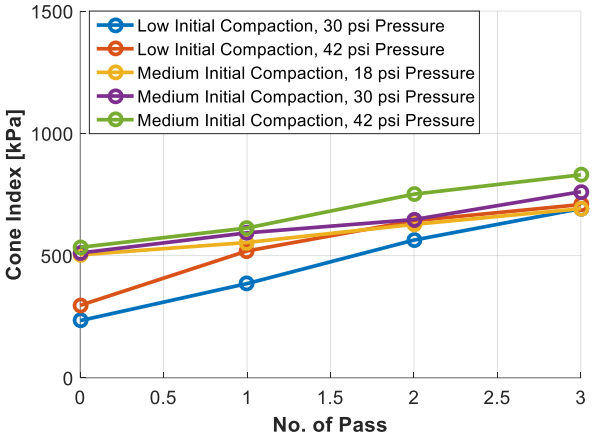

(a) Variation in cone index with number of passes.

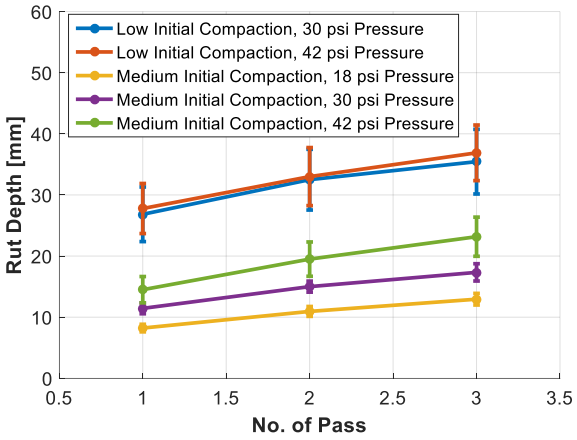

(b) Variation in rut depth with number of passes.

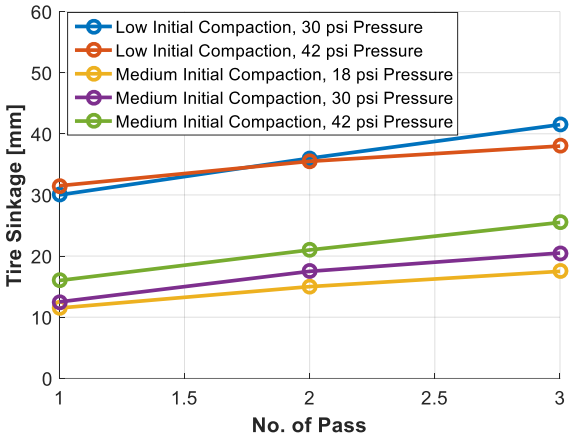

(c) Variation in tire sinkage with number of passes.

Figure 4.49: Multi-pass effect on the soil response when the tire was in the towing mode.

Figure 4.50 plots the typical tractive performance parameters such as drawbar pull coefficient and drawbar efficiency against their corresponding actual slip ratios. Note in Figure 4.48b, at medium initial soil compaction level and 42 psi inflation pressure, the rolling radius drops slightly down after each pass. However, because measuring the rolling radius (in the towing mode) and testing the tire in traction mode on the same soil could not be done simultaneously for each pass, the actual slip ratios in Figure 4.50 was calculated by using the same value of rolling radius 339.5 mm (listed in Table 4.12), nearly the same as the value of the point at the 1st pass, 42 psi inflation pressure, and medium initial soil compaction in Figure 4.48b. From Figure 4.50, it can be seen that the actual slip ratios vary slightly and

negligibly from the nominal slip ratios between different passes of the tests in traction mode.

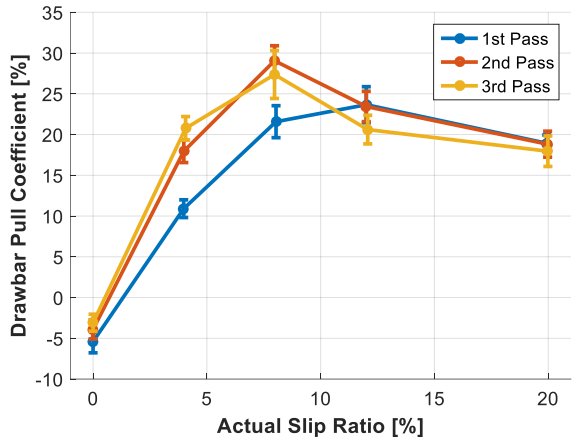

(a) Variation in drawbar pull coefficient with slip ratio for all three passes.

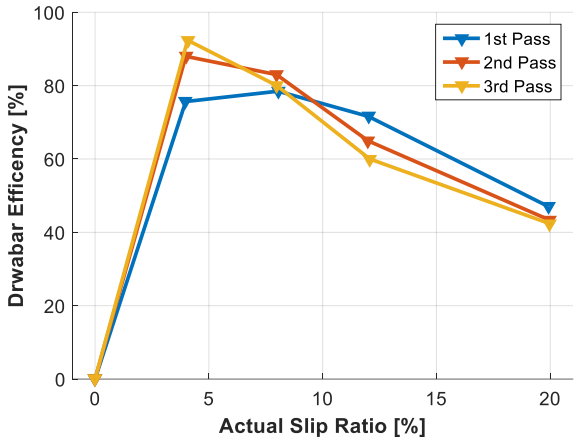

(b) Variation in drawbar efficiency with slip ratio for all three passes. Drawbar efficiency is assumed to be zero at zero slip ratio

Figure 4.50: Multi-pass effect on the tire tractive performance at multiple slip ratios. The inflation pressure is 42 psi, the initial soil compaction level is medium, and the normal load is 5 kN.

When the nominal slip ratio is either 0 or 4%, the DPC increases with number of passes, following the same trend as previously described for the tests in towing mode, also in an agreement with the classical studies on the multi-pass effect [141], [142], [13]. However, at the 8% nominal slip ratio, the DPC first rises from the 1st pass to the 2nd pass and yet decreases from the 2nd pass to the 3rd pass. Further, at the 12% or 20% nominal slip ratio, the DPC decreases slight slightly from the 1st pass to the 2nd pass and decrease a little more from the 2nd pass the 3rd pass. The trend of DE (ignoring the DE at zero slip) is nearly the same as the trend of DPC when the number of passes changes. Such trends observed from the Figure 4.50 is very different from the studies [141], [142], [13], [138] and even opposite at 12% or 20% nominal slip ratio to the trends described in these studies.

Figure 4.51 demonstrates that the cone index, rut depth, and tire sinkage increases with the number of passes, which is generally in accordance with the aforementioned trends for the tests in towing mode and the trends from the studies [141], [142]. Also seen from Figure 4.51, the growth rate of rut depth and tire sinkage slows down at positive slip ratios as the number of passes increases.

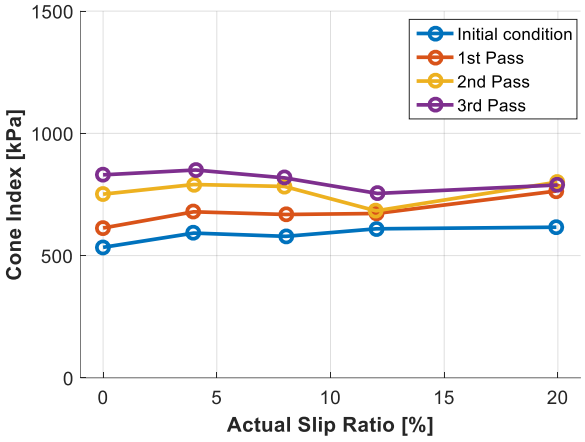

(a) Variation in cone index before the first pass and after each of the three passes.

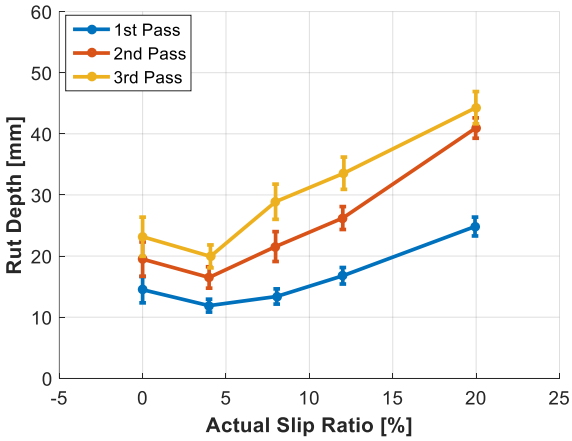

(b) Variation in rut depth with slip ratio for all three passes.

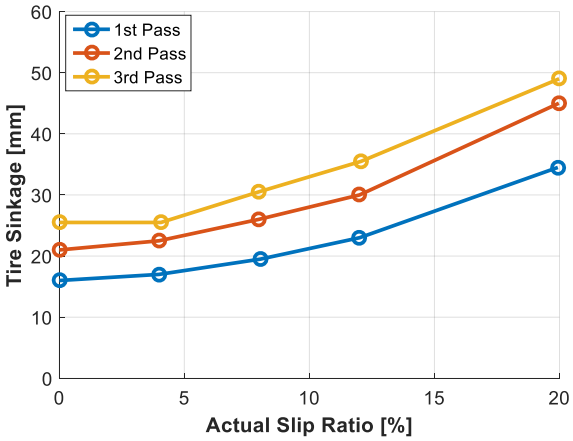

(c) Variation in tire sinkage with slip ratio for all three passes.

Figure 4.51: Multi-pass effect on the soil response at multiple slip ratios. The inflation pressure is 42 psi, the initial soil compaction level is medium, and the normal load is 5 kN.

A rough explanation is stated here on the trend of DPC at different slip ratios and number of passes. When the slip ratio is as low as 0 or 4%, each pass of the tire compacts the soil more, and importantly, the soil has not failed. This can be reflected by the variation of cone index and DPC with the number of passes. The cone index increases after each pass. As explained in detail in Section 4.5.2.5, the shear strength of the soil rises as the soil gets more compacted, and hence the tractive effort increases despite of the reduction in contact area, which, together with the reduction in motion resistance, leads to a larger DP and hence DPC at the constant normal load. The same mechanism works for the 1st pass at 8% slip ratio and

explains why the DPC in the 2nd pass at 8% slip ratio is higher than that in the 1st pass at 8% slip ratio. However, the mechanism fails to explain why the DPC in the 3rd pass at 8% slip ratio is lower than that in the 2nd pass at 8% slip ratio. The reason is that soil failure has happened during the 2nd pass as the rut fluctuation (ripple) occurs and some part of the rut bottom surface gets layered, as shown in Figure 4.52b; consequently, the shear strength of the soil doesn't increase after the 2nd pass at 8% slip ratio but decreases, which leads to the lowered DPC in the 3rd pass at 8% slip ratio. When the slip ratio is either 12% or 20%, after the 1st pass, the ripples has occurred, e.g., as shown in Figure 4.52c, and after the 2nd and 3rd, more and more ripples has formed, meaning that more and more soil close to the surface has failed; consequently, the shear strength decreases over each pass, which leads to lower DPC one pass after another despite of possibly reduced motion resistance. Note that only the soil in proximity of the surface where the local shear failure zone spans (the sheared soil) has gone through failure; the shear strength of this part of soil is reduced. However, there is soil beneath (the soil at greater depth) this part of soil which could get more compacted after each pass and which could get penetrated by the cone penetrometer when measuring the cone index after each pass. Because of that, the cone index gets bigger after each pass, which cannot reflect the reduction in shear strength of the sheared soil, and the increase in rut depth and tire sinkage is reduced with an increase in the number of passes.

(a) 1st pass, 8% slip. No ripple is formed.

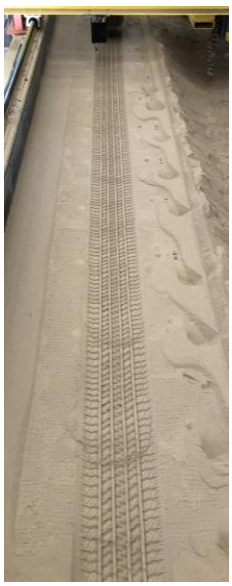

(b) 2nd pass, 8% slip. Ripples are formed.

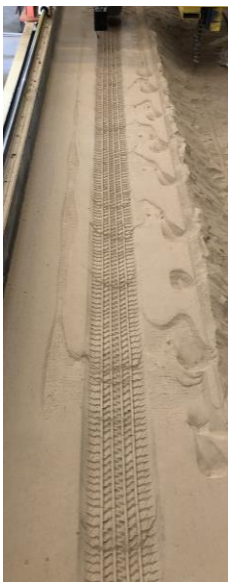

(c) 3rd pass, 8% slip. More ripples than the 2nd pass.

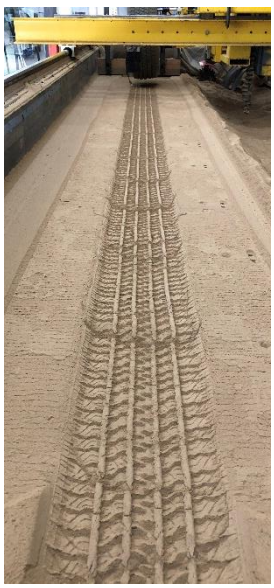

(d) 1st pass, 12% slip. Ripples are formed.

Figure 4.52: Rut formed after some pass of the lab multi-pass tire-soil tests at 42 psi inflation pressure and 5 kN.

Chapter 5

Model Parameterization

This chapter includes materials from [12] *by R. He, C. Sandu, and J. E. Osorio, with the permission from Elsevier, and the agreement attached.*

The test data collected from the tests has been analyzed in Chapter 4. Chapter 4 and this chapter together present parameterization methods for terramechanics models and the Magic Formula tire model. The experimental part of the parameterization methods, i.e., the series of tire tests, soil tests, and tire-soil test, has been explained in detail in Chapter 4. In this chapter, how the test data was fed into optimization program to evaluate model parameters is explained.

This chapter is structured as follows: Section 5.1 deals with the parameterization of a bulk density estimation model using the test data from the lab soil properties tests (lab SP tests). Section 5.2 provides an algorithm to parameterize the Magic Formula tire model, parameterization results, and the inclusion of tire inflation pressure and cone index as the model inputs. In Section 5.3, a parameterization method based on the static tire deflection tests and laboratory dynamic tire-soil tests is proposed for the modified Bekker's pressure-sinkage model.

5.1 Parameterization of a Bulk Density Estimation Model

Soil bulk density can be measured by the direct method, e.g., sampling, drying, and weighing, as described in Section 4.2.1, or by the indirect method, e.g., using the nuclear density device. Both direct and indirect methods can be laborious and time-consuming [143]. The soil bulk density estimation method can be faster and more convenient than the direct and indirect methods in evaluating bulk density because it is based on the formulas that relate soil bulk density to other soil parameters that can be quickly measured. It has been shown that applying a certain empirical formula parameterized by the data from the laboratory and

field tests can achieve field bulk density estimation with a relative error around 10% [143]. In this study, the test data from the lab SP tests was used to parameterize a bulk density estimation model that aims to be used for the on-site soil compaction evaluation in the dynamic tire-soil tests.

The benefits of using the bulk density estimation model in the on-site soil compaction evaluation are as follows. Once the bulk density estimation model is parameterized, after the soil preparation for the lab tire-soil test, the water content and cone index of the prepared soil are measured, and the measurement data is fed to the bulk density estimation model to compute the bulk density of the prepared soil. This whole process takes less time than the direct method to measure bulk density. Besides, as described in Section 4.4.2 and 4.5.1, in the lab DTS test or lab static tire-soil test (STS test), the measurements of CI and VWC were taken for the prepared flat soil track, if the direct method were applied, and the prepared soil were sampled close to the location where the CI and VWC were measured, the flat surface of the prepared soil would be ruined, which negates the soil preparation. In contrast, using the bulk density estimation model to evaluate the bulk density of the prepared soil means that the prepared flat soil track where the tire will transverse remains nearly intact. The prerequisite for those benefits is the bulk density estimation model can predict bulk density within an acceptable error; as will be explained later, this prerequisite is met given the prediction error of the selected bulk density estimation model is less than 3%.

The values of CI, bulk density, and water content can be used to make sure the soil condition remains almost the same in the lab tire-soil tests that aim at studying the influence of factors other than the soil condition, to compare the soil condition in the tests with the soil condition in other relevant research, and to be fed into tire off-road traction models, such as the Upadhyaya et al. semi-empirical traction model [78], or other models that require the values of these soil parameters.

There are numerous models that were proposed to estimate bulk density using the measurements of other soil parameters [144]. The bulk density estimation model that has a small number of equations and parameters was preferred in this study because the parameterization of such a model would be easier. Also, the test soil in this study couldn't

maintain gravimetric water content larger than 8.8% [127], [48]; therefore, the bulk density estimation model chosen for the test soil is supposed to work at low levels of gravimetric water content. The model proposed by Ayers and Perumpral [145] was selected to be the bulk density estimation model in this study, as it can work in a wide range of water content and capture the peak cone index that occurs at low levels of water content, and its parameterization can be completed through nonlinear regression [146]. This model given below is an empirical model that relates bulk density γ_d to cone index CI and gravimetric water content θ_g.

$$\gamma_d = \left\{ \left(CI / C_1 \right) \left[C_2 + \left(\theta_g - C_3 \right)^2 \right] \right\}^{1/C_4} \tag{5.1}$$

With the corresponding bulk density known, gravimetric water content can be used to obtain volumetric water content θ_v. Therefore, Equation (5.1) can be manipulated into:

$$CI = \frac{A_1 {\gamma_d}^{A_2}}{A_3 + \left(\theta_v / \gamma_d - A_4 \right)^2} \tag{5.2}$$

Both Equation (5.1) and Equation (5.2) can estimate bulk density. While plugging the measurement data of gravimetric water content and cone index into Equation (5.1) can easily evaluate bulk density, feeding the measurement data of volumetric water content and cone index into Equation (5.2) cannot. In Equation (5.2), the bulk density is neither an explicit function in terms of volumetric water content and cone index and nor can be such an explicit function after manipulating Equation (5.2). After the measurement data of volumetric water content and cone index are input to Equation (5.2), Equation (5.2) needs to be numerically solved to evaluate bulk density.

Nonlinear regression was carried out in MATLAB to Equation (5.1) and the measurement data of bulk density, cone index, and gravimetric water content from the lab SP tests. The curve fitting of Equation (5.1) to the measurement data points is presented in Figure 5.1.

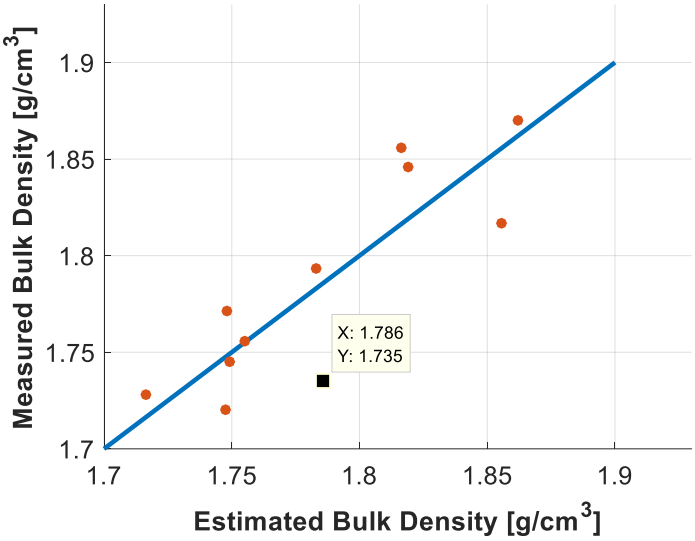

Figure 5.1: Curve of bulk density estimation model vs. the measurements of bulk density.

Table 5.1 presents the part of the nonlinear regression analysis results, including the values of the model parameters of Equation (5.1) computed in the nonlinear regression. The value of R^2 is found to be 0.731 for Equation (5.1) in the regression analysis. Although this value doesn't look perfect, i.e., it is not very close to 1, the largest relative estimation error, as indicated by the point highlighted in black in Figure 5.1, is calculated to be 2.94%. Given this small estimation error, the model proposed by Ayers and Perumpral [145] could be considered a good choice of the bulk density estimation model in the on-site soil compaction evaluation for the test soil in this study. To further validate this model for the test soil, the data from more soil property tests is needed, the measurements of bulk density will need to be compared with the bulk density predicted by using Equation (5.1) at the model parameters $C_{i,\ i\ =\ 1,\ 2,\ 3,\ 4}$ shown in Table 5.1.

Table 5.1: Nonlinear regression analysis outputs describing the relation between the model output, bulk density, and the model inputs: cone index and gravimetric water content.

Coefficient	Value
C_1	5.934e-10
C_2	0.022
C_3	0.609
C_4	42.996
R^2	0.731
RMSE	0.0282

5.2 Parameterization of the Magic Formula Tire Model

The measurement data of drawbar pull from the laboratory dynamic tire-soil tests of 2017 were used to determine the parameters of the Magic Formula tire model by two methods. The first method is based on geometric features of the MFTM, and the second method is based on a genetic algorithm. In this section, the geometric features of the MFTM is introduced first. Next the genetic algorithm and how the algorithm works in an optimization program to compute the model parameters of the MFTM are explained, followed by the parameterization results of applying the two methods. Finally, details are given about the proposed and validated dependency of MFTM model parameters on the tire inflation pressure and cone index.

5.2.1 Geometric Features of the Magic Formula Tire Model

In cases of pure longitudinal slip, the Magic Formula tire model [85] is given by the set of equations below [18]. It can be seen that the main formula Equation (5.3) is highly nonlinear.

$$y(x) = D\sin\left[C\arctan\left\{Bx - E\left(Bx - \arctan(Bx)\right)\right\}\right] \tag{5.3}$$

with

$$Y(X) = y(x) + S_v \tag{5.4}$$

$$x = X - S_h \tag{5.5}$$

The values of some MFTM model parameters influence the geometry of the MFTM curve, as illustrated by Figure 5.2. Based on such geometric features, some model parameters of MFTM are correlated to the optimal model input, the maximum model output, and the slope at the origin, and the asymptotic model output by [20]:

$$B = \frac{\tan\theta}{CD} \tag{5.6}$$

$$C = 2 - \frac{2}{\pi}\arcsin\frac{y_s}{D} \tag{5.7}$$

$$D = y_m \tag{5.8}$$

$$E = \frac{Bx_m - \tan\frac{\pi}{2C}}{Bx_m - \arctan(Bx_m)} \tag{5.9}$$

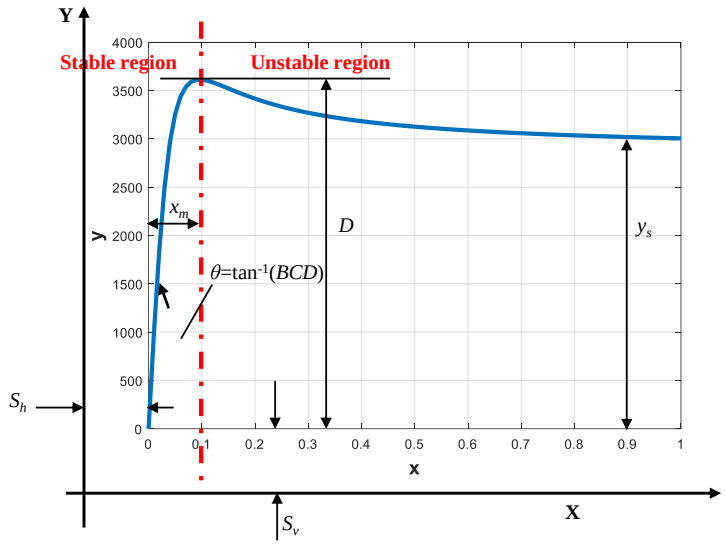

Figure 5.2: Geometric interpretation of the MFTM model parameters.

If the optimal model input, the maximum model output, and the slope at the origin, and the asymptotic model output are found on the broken line of the DP versus slip ratio measured in the lab DTS tests, the model parameters of the MTFM can be determined. However, in this parameterization method, only part of the test data is used to evaluate the parameters correlated to the model parameters of the MFTM. Therefore, it is possible that not all the test

data will fit the curve of the MFTM at the parameters determined by this parameterization method. Still, this parameterization method remains to be a valid method to check the suitability of test data for the parameterization of the MFTM and to compute the initial guess of the MFTM model parameters required by some optimization algorithm that has the capability to parameterize the MFTM, e.g., the algorithm for the nonlinear regression performed in MATLAB as mentioned in Section 5.1.

5.2.2 Genetic Algorithm

Some optimization algorithms commonly used in the model parameterization, e.g., the Gauss-Newton algorithm and the Levenberg-Marquardt algorithm, require a reasonable initial guess of model parameters [147], while the genetic algorithm (GA) has a looser requirement for the initial guess of model parameters, yet possibly at the cost of computational speed [83]. Because of that, it has been used in the optimization for parameterizing highly nonlinear tire models with model parameters for which it is difficult to estimate the reasonable initial guess [84], [148], [149].When the MFTM model parameters are set to be functions of tire inflation pressure or normal load, as described in Section 5.2.4, it can be hard to obtain a proper initial guess of the coefficients of these functions; for this reason, a genetic algorithm was utilized in this study.

The genetic algorithm applied in this study is modified from [83]. The MFTM input X and output Y are set to be slip ratio and drawbar pull or drawbar pull coefficient respectively. Based on the genetic algorithm, an optimization program was written in MATLAB. The optimization program uses the test data collected from the lab DTS tests of 2017 and aims to compute the best model parameters of the MFTM so as to reduce the value of the cost function to an acceptable value; the cost function is the sum of the squared differences between the values of drawbar pull computed by the MFTM and the measurements of drawbar pull DP for all the fourteen test slip ratio levels at one test inflation pressure level:

$$\sum_{i=1}^{14}\left[Y_i(X_i)-DP_i(X_i)\right]^2 \qquad 5.10$$

The genetic algorithm has three main parts for each iteration of a loop in the optimization

program, selection, reproduction, and mutation. Before the iteration starts, an initial population is generated; the population has *NP* individuals. The individual (chromosome) is formed by the model parameters of the MFTM to be tuned in the optimization, and each model parameter is seen as a gene that is expressed by a base-ten real number. A number that falls in a guess interval is randomly assigned to each gene. The guess interval can be loose, preferably containing the optimum, and based on the experience from the existing literature,. As the iteration proceeds, the population updates; each iteration has its corresponding generation of the population. The best chromosome of each generation of the population has the best fitness: after substituting the parameters represented by all the chromosomes of one generation to the cost function, the best chromosome corresponds to the smallest value of the cost function.

Each iteration of the optimization loop starts with the selection: the best chromosome and the two chromosomes $X_{r,1}$, $X_{r,2}$ randomly selected under the uniform distribution make up a disturbing vector, as defined below:

$$\begin{aligned} & X_{p,i} : i \in [1, NP] \\ & V = X_{best} + F \cdot \left(X_{r,1} - X_{r,2} \right) \end{aligned} \tag{5.11}$$

Next, the iteration comes to the stage of reproduction: the disturbing vector is crossed with several chromosomes of one generation $X_{p,i}$ to produce descendants, and this operation is called crossover; the crossover is performed at a probability *CP*. The reproduction is followed by the mutation: randomly chosen genes of some descendants increases or decreases their values by a random number Δ that falls in the aforementioned guess interval; the mutation happens at a probability *MP* that is normally smaller than *CP*. After going through the reproduction and mutation, one descendant is compared with its parent that has crossed with the disturbing vector. If the descendant has better fitness than its parent, the descendant replaces its parent and goes to the next generation of population, otherwise the parent goes to the next generation. After the next generation of population is formed, a new best chromosome will be selected, followed by the beginning of a new iteration. The loop repeats itself until the cost function at the best chromosome of some generation reaches an acceptable value; that best chromosome represents the best MFTM model parameters solved

by this optimization program.

Table 5.2 lists the values of the aforementioned genetic algorithm parameters in the optimization program. The maximum number of iterations is 4000; as it will be shown later in the next sub section, for the three test tire inflation pressure levels, the number of iterations in the optimization program doesn't reach 4000.

Table 5.2: Main genetic algorithm parameters in the optimization program for the MFTM model parameterization.

Algorithm parameter	Value
F	0.4
CP	0.6
MP	0.1
NP	50
Itermax	4000

5.2.3 Parameterization Results of the Magic Formula Tire Model

As explained in Section 2.1 and 4.5.2, the rolling radius, estimated in the lab STS tests of July 2017 and later used to define the slip ratio in the lab DTS tests of 2017, is smaller than the true value; as a consequence, the actual slip deviates from the true value. To offset such deviation, the zero slip ratio is no longer defined under the free-rolling condition but is defined under the self-propelled (zero drawbar pull) condition on the test soil, in agreement with one of the zero conditions defined in [22], [150], [21]. Under this zero slip ratio definition, the actual slip ratios obtained in the lab DTS tests of 2017 are now shifted by a distance to the right such that the drawbar pull at the zero slip is zero, and the stable region keeps linear. The shift distance was obtained through extrapolation from the points at nominal slip ratios of 0 and 2.5% in the DPC vs slip plot (Figure 4.39). Such shift doesn't influence the trend of the experimental DPC vs. slip curve, and is in accordance with the definition of slip ratio for off-road vehicles [22].

Using Equations (5.6) – (5.9) (based on the geometric features of the MFTM) and part of the test data from the lab DTS tests of 2017, the model parameters of the MFTM and the sum

of the squared differences were calculated, as shown in Table 5.3.

Table 5.3: Parameters of the MFTM determined by using the geometric features of the MFTM and part of the test data from the lab DTS tests of 2017.

Tire inflation pressure [psi]	B	C	D	E	Sv	Sh	Final value of the cost function
18	0.0540	1.4743	1.6397	-15.1235	0	0	0.1721
30	0.0566	1.5664	1.0058	-14.0852	0	0	0.0220
42	0.0943	1.4476	0.5740	-13.1655	0	0	0.0214

The curves of the MFTM at the parameters listed in Table 5.3 together with the measurements of drawbar pull are displayed in Figure 5.3. These curves fit the measurement data points of drawbar pull pretty well for the 30 psi and 42 psi inflation pressure and acceptably for the 18 psi inflation pressure; because of that, the test data from the lab DTS tests of 2017 has good suitability for the parameterization of the MFTM. Since the geometric features of the MFTM are part of the MFTM's mathematical nature, the parameterization method based on them can serve as a benchmark method for the parameterization of the MFTM. In contrast, the parameterization method based on the genetic algorithm doesn't use any of the MFTM's mathematical nature.

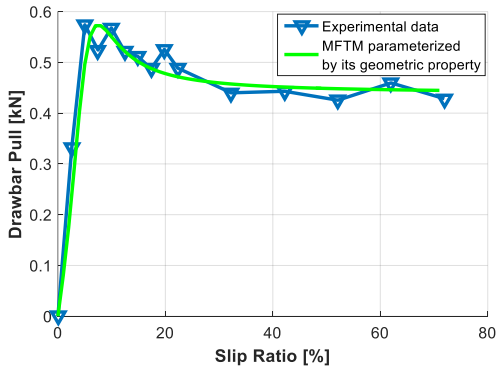

(a) MFTM vs. slip at 42 psi inflation pressure.

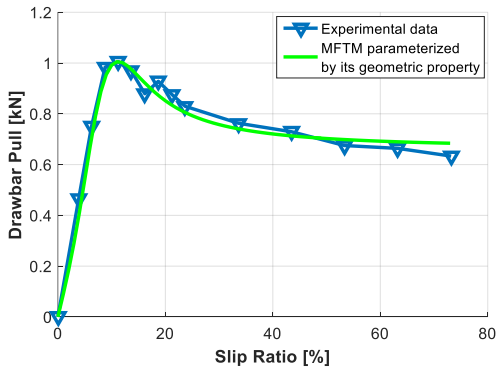

(b) MFTM vs. slip at 30 psi inflation pressure.

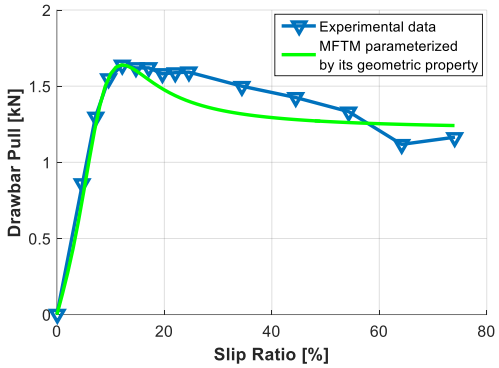

(c) MFTM vs. slip at 18 psi inflation pressure.

Figure 5.3: Curve of the MFTM parameterized by using its geometric features vs. the measurements of the DP from the lab DTS tests of 2017.

Table 5.4 lists the model parameters that were computed by the optimization program as described in Section 5.2.2. The model parameters D, which stands for the peak drawbar pull, and C, the shape factor, were computed to be almost the same that were calculated by the parameterization method based on the geometric features of the MFTM. Also, Table 5.4 and Table 5.3 show that both parameterization methods yield very close final values of the cost function.

Table 5.4: Parameters of the MFTM determined by the genetic algorithm and the test data from the lab DTS tests of 2017.

Tire Inflation Pressure [psi]	B	C	D	E	S_v	S_h	Final value of the cost function
18	0.0794	1.5619	1.6480	-0.1026	0	0	0.0485
30	0.0713	1.5685	1.0071	-6.0844	0	0	0.0091
42	0.1265	1.4802	0.5954	-8.1747	0	0	0.0083

During the running of the optimization program, the cost function value decreases with the number of iteration, as indicated by Figure 5.4. For the 18psi, 30 psi and 42 psi tire inflation pressure, the cost function converges to an acceptable value before the 4000^{th} iteration. However, the cost function for the 18 psi tire inflation pressure doesn't have a final value smaller than that for the 30 psi and 42 psi. The reason is that the test data at the 30 psi and 42 psi tire inflation pressure has better suitability for the parameterization of the MTFM than the test data at the 18 psi: as illustrated by Figure 5.3c and Figure 5.5c, the curvature of experimental DP broken line in the unstable region cannot be captured by the MFTM regardless of the values of the model parameters.

The curves of the MFTM at the parameters listed in Table 5.4 together with the measurements of drawbar pull are displayed in Figure 5.5. Comparing Figure 5.5 with Figure 5.3, it is concluded that both parameterization methods produce very similar MFTM curves at the same tire inflation pressure. Therefore, with the parameterization method based on the geometric features of the MFTM as a benchmark method, the capability of the parameterization method based on the genetic algorithm for the MFTM is demonstrated.

Because the benchmark method is based on the mathematical nature of the MFTM, if the model parameters of the MFTM are set to be functions of tire normal load or other parameters of interest, the benchmark method might not be used for the model parameterization in this situation, while the genetic algorithm-based method, not restricted to the mathematical nature of the MFTM, can still be used, as shown in [83]. The parameterization of a model using test data is actually modeling the test data, which is supposed to account for all the test data. The benchmark method doesn't use all the test data, while the GA-based method does; this explains why the final value of the cost function computed by the GA-based method can be smaller than that by the benchmark method.

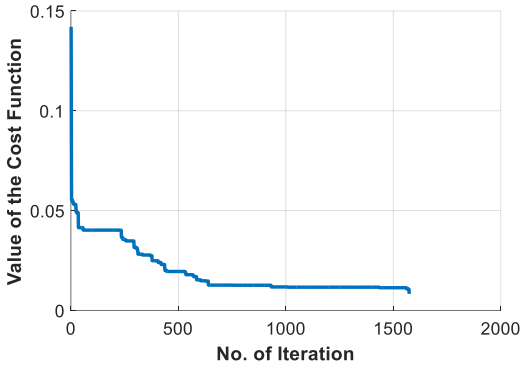

(a) Value of the cost function vs number of iterations at 42 psi inflation pressure.

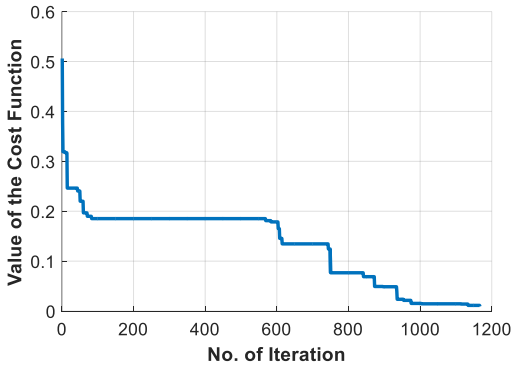

(b) Value of the cost function vs number of iterations at 30 psi inflation pressure.

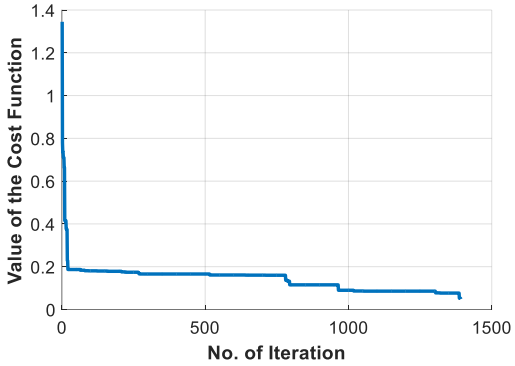

(c) Value of the cost function vs number of iterations at 18 psi inflation pressure.

Figure 5.4: Variations in the cost function value with iteration.

Both Figure 5.5 and Figure 5.3 indicate acceptable fittings of the MFTM to the measurement data points of the DP from the lab DTS tests of 2017. For all the tire inflation pressure levels, the measured peak drawbar pull and its corresponding slip ratio are captured by the MFTM curve; also, the MFTM curve can approximate the asymptotic part of the drawbar pull measurement data points. Except for the unstable region at the 18 psi inflation pressure, the curvature of the MFTM curve at both stable and unstable regions is similar to that of the DP measurements.

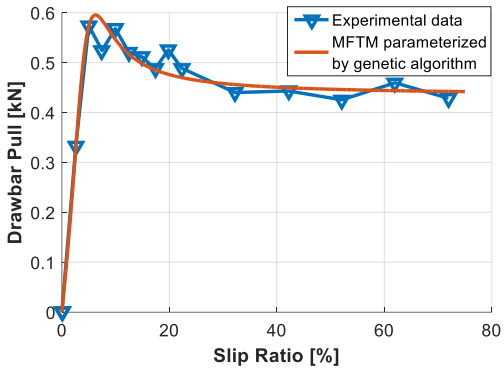

(a) MFTM vs. slip at 42 psi inflation pressure.

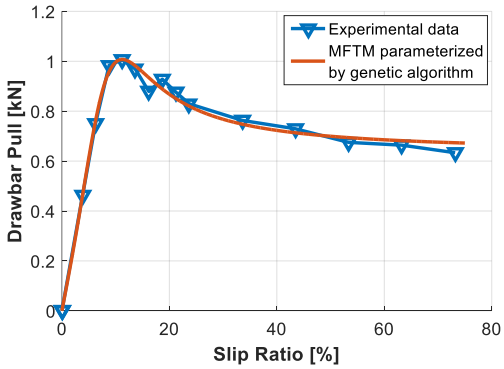

(b) MFTM vs. slip at 30 psi inflation pressure.

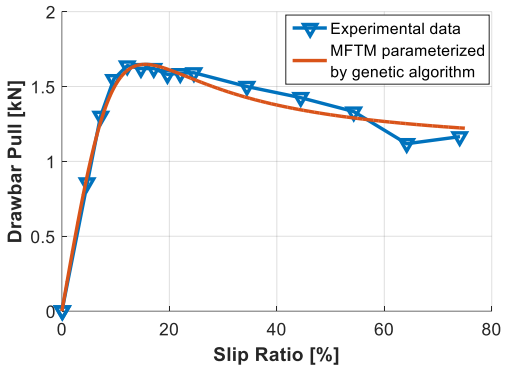

(c) MFTM vs. slip at 18 psi inflation pressure.

Figure 5.5: Curve fitting of the MFTM to the measurements of the DP from the lab DTS tests of 2017.

5.2.4 Parameters as Functions of Inflation Pressure

The MTFM model parameters were found to be influenced by tire normal load and tire inflation pressure and hence were set to be the functions of tire normal load and tire inflation pressure [124], [125]. When the tire normal load remains constant, the functions proposed in [124], [125] can be modified to the functions below which are only dependent on the dimensionless change in tire inflation pressure dp_i. The maximum tire pressure $p_{i,\ max}$ is obtained from the ASTM standard [151].

$$dp_i = \frac{p_{i,\max} - p_i}{p_{i,\max}} \tag{5.12}$$

$$B = \frac{c_4 + c_5 p_i + c_6 p_i^2}{CD} \tag{5.13}$$

$$C = c_0 \tag{5.14}$$

$$D = c_1 + c_2 p_i + c_3 p_i^2 \tag{5.15}$$

$$E = c_7 + c_8 p_i + c_9 p_i^2 \tag{5.16}$$

Using the genetic algorithm with the same parameter values as that in Table 5.2, all the drawbar pull-slip data collected from the lab DTS tests of 2017, and the cost function Equation (5.17), an optimization program was developed to parameterize the MFTM with two model inputs: slip ratio and tire inflation pressure. The cost function value needs to be reduced to an acceptable value such that the satisfactory curve fitting of the MFTM to the drawbar pull-slip data at the 18 psi, 30 psi, and 42 psi tire inflation pressure is achieved.

$$\sum_{j=1}^{42} \left[Y_j(X_j, dp_{i,j}) - DP_j(X_j) \right]^2 \tag{5.17}$$

The coefficients in Equations (5.13) – (5.16) and the final values of the cost function were computed by the optimization program and listed in Table 5.5. The cost function value after each iteration of the loop in the optimization program is plotted against the number of iteration in Figure 5.6; as the loop in the optimization program continues, the cost function value decreases intermittently.

Table 5.5: Coefficients relating the MFTM model parameters to tire normal load and tire inflation pressure determined by the genetic algorithm and the test data at the 18 psi, 30 psi, and 42 psi tire inflation pressure from the lab DTS tests of 2017.

Coefficients	c_0	c_1	c_2	c_3	c_4	c_5
Values	1.58	0.52	1.08	1.44	0.19	-0.55
Coefficients	c_6	c_7	c_8	c_9	Final value of Equation (5.17)	
Values	0.98	1.78	-40.69	61.58	6.61e-2	

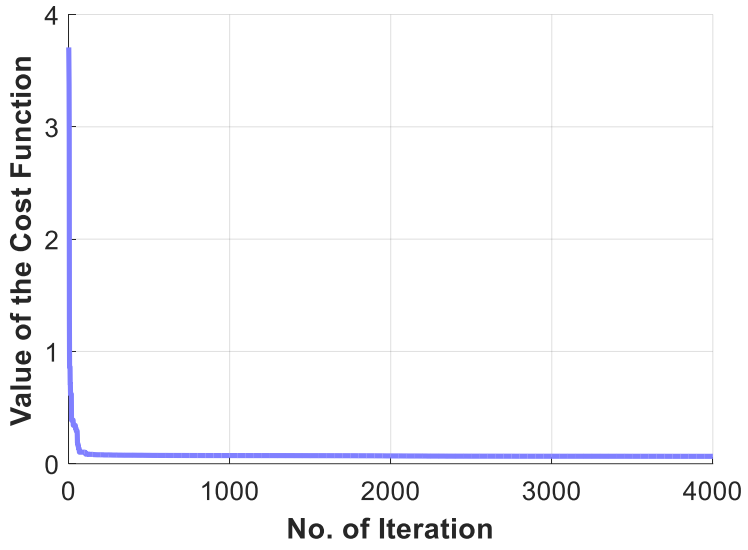

Figure 5.6: Variations in the cost function value in parameterizing the MTFM that accounts for the influence of tire inflation pressure.

Using the coefficient values listed in Table 5.5, the MFTM with its model parameters dependent on tire inflation pressure fits the measurement data points of the DP from the lab DTS tests in 2017 agreeably, as shown in Figure 5.7. The drawbar pull measurements' peak drawbar pull, asymptotic drawbar pull, and curvature in both the stable and unstable regions are captured by the MFTM and Equations (5.13) – (5.16) in a way almost the same as shown in Figure 5.5. The MTFM model parameters are the quadratic functions of tire inflation pressure as Equations (5.13), (5.15) – (5.16). Determining a quadratic function requires three different points. Therefore, when values of the MFTM model parameters B, D, and E are fixed, three different levels of tire inflation pressure are needed to determine the coefficients of Equations (5.13), (5.15) – (5.16). To further validate the MFTM and Equations (5.13) – (5.16) that models the drawbar pull as functions of tire inflation pressure and slip ratio in the off-road condition, measurements of drawbar pull and slip ratio at levels of tire inflation pressure other than the 18 psi, 30 psi, and 42 psi are needed.

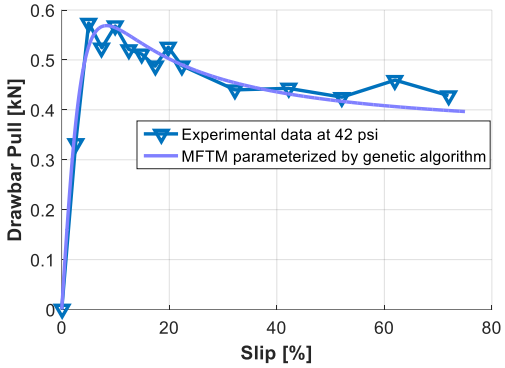

(a) MFTM vs. slip at 42 psi inflation pressure.

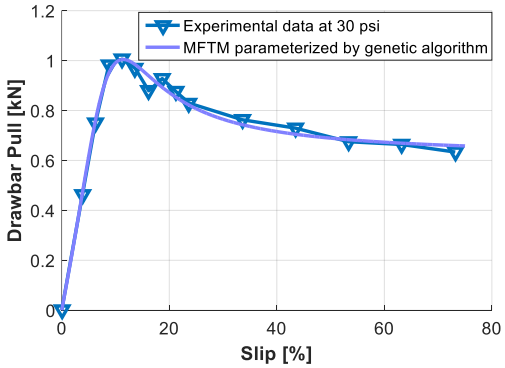

(b) MFTM vs. slip at 30 psi inflation pressure.

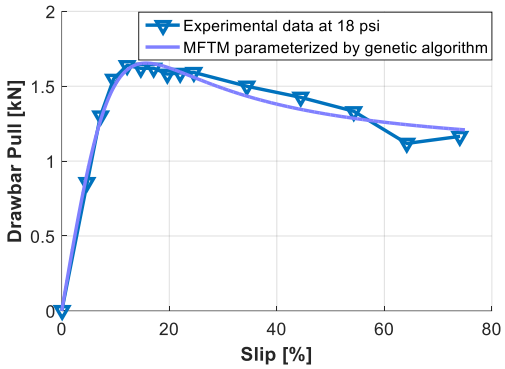

(c) MFTM vs. slip at 18 psi inflation pressure.

Figure 5.7: Curve fitting of the MFTM accounting for the tire inflation pressure influence to the measurements of the DP from the lab DTS tests of 2017.

5.2.5 Parameters as Functions of Cone Index and Inflation Pressure

It's clear from Figure 4.42 that not only the tire inflation pressure but also the initial soil compaction influences the drawbar pull or drawbar pull efficient. Because of such influence from the initial soil compaction on the drawbar performance of tire on soft soil, the model parameters of the Magic Formula tire model are proposed to be the functions of tire inflation

pressure and cone index in this dissertation, as shown by Equations (5.19) – (5.23). As for the dry soft soil, the water content remains to be low at around a constant value, as illustrated by Figure 4.26d – f; given the relationship of water content, bulk density, and cone index, characterized by Equation (5.1), the soil compaction can be characterized by the cone index alone. Therefore, only the cone index is chosen as the only soil parameter incorporated into the Magic Formula such that the influence of the soil compaction of the dry soft soil on the tire drawbar performance is accounted for.

In Equation (5.18), the maximum cone index value of the soil CI_{max} is obtained from the lab soil properties test. This value is listed in Table 4.2 (1631.015 kPa for the sample no. 4).

$$dCI = \frac{CI}{CI_{\max}} \tag{5.18}$$

The cone index and inflation pressure, after non-dimensionalized by Equation (5.18) and Equation (5.12) respectively, are set to be the variables of the Magic Formula model parameters.

$$B = \frac{e_1 + e_2 \cdot dp_i + e_3 \cdot dCI + e_4 \cdot dCI \cdot dp_i + e_5 \cdot dp_i^2 + e_6 \cdot dCI_i^2}{C \cdot D} \tag{5.19}$$

$$C = e_0 \tag{5.20}$$

$$D = e_7 + e_8 \cdot dp_i + e_9 \cdot dCI + e_{10} \cdot dCI \cdot dp_i + e_{11} \cdot dp_i^2 + e_{12} \cdot dCI_i^2 \tag{5.21}$$

$$E = e_{13} + e_{14} \cdot dp_i + e_{15} \cdot dCI + e_{16} \cdot dCI \cdot dp_i + e_{17} \cdot dp_i^2 + e_{18} \cdot dCI_i^2 \tag{5.22}$$

$$S_v = e_{19} + e_{20} \cdot dp_i + e_{21} \cdot dCI + e_{22} \cdot dCI \cdot dp_i + e_{23} \cdot dp_i^2 + e_{24} \cdot dCI_i^2 \tag{5.23}$$

The Magic formula with Equations (5.19) – (5.23) has the drawbar pull coefficient as the

model output Y, assumes zero S_h, and assumes a small variation in normal load and hence negligible influence of the normal load on DPC

$$\sum_{j=1}^{93}\left[Y_j(X_j, dp_{i,j}, dCI_{i,j}) - DPC_j(X_j)\right]^2 \qquad 5.24$$

The measured drawbar pull coefficient and slip ratio, their corresponding inflation pressure, and their corresponding cone index, all from the lab DTS tests (shown in Figure 4.42), were fed into an optimization program based on the genetic algorithm. This time, most of the genetic algorithm main parameters have the same value as listed in Table 5.2 except that the maximum number of iterations *Itermax* is 400000. The cone index values substituted into Equation (5.18) were calculated by averaging the measured cone index, as shown in Figure 4.26a – c, at the three initial soil compaction levels respectively. This optimization program reduced the value of the cost function Equation (5.24) to an acceptable value, computed the corresponding coefficients of Equations (5.19) – (5.23), and hence parameterized the MFTM that sets slip ratio, tire inflation pressure, and cone index. These computed coefficients are listed in Table 5.6.

Table 5.6: Coefficients relating the MFTM model parameters to tire inflation pressure determined by the genetic algorithm and the test data from the lab DTS tests at the 18 psi, 30 psi, and 42 psi inflation pressure; low, medium, and high initial soil compaction; and 5 kN normal load.

Coefficients	e_0	e_1	e_2	e_3	e_4	e_5	e_6	e_7	e_8	e_9
Values	1.53	0.63	-3.94	10.80	12.04	17.70	-3.75	18.33	15.91	20.56
Coefficients	e_{10}	e_{11}	e_{12}	e_{13}	e_{14}	e_{15}	e_{16}	e_{17}	e_{18}	e_{19}
Values	5.56	21.65	2.01	-2.80	0.85	2.29	-2.60	6.63	-0.05	-17.09
Coefficients	e_{20}	e_{21}	e_{22}	e_{23}	e_{24}	Final value of Equation (5.24)				
Values	-0.11	46.83	-6.39	11.33	-38.58	112.31				

The cost function Equation (5.24) is the sum of the squared errors between the measured drawbar pull coefficient from the lab DTS tests (shown in Figure 4.42) and the drawbar pull coefficient predicted by the MFTM; the variation in cost function value with the iteration number in the optimization program can be found in Figure 5.8. The final value of the cost function is listed in Table 5.6; it's satisfactory because, averagely speaking, each error is around 1.1%.

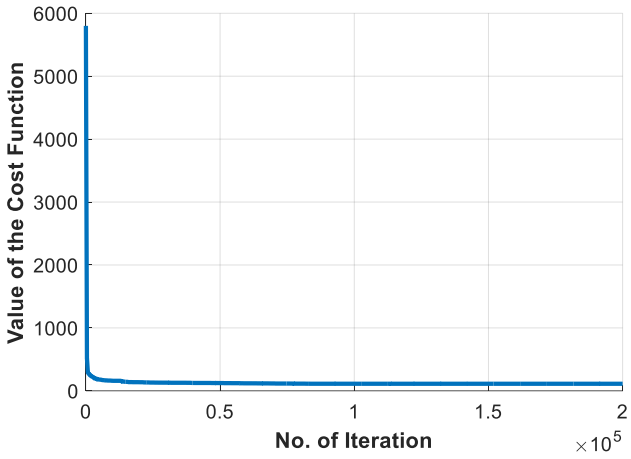

Figure 5.8: Variations in the value of the cost function Equation 5.24 in parameterizing the MTFM that accounts for the influence of initial soil compaction and tire inflation pressure.

With the coefficient values listed in Table 5.6 plugged into Equations (5.19) – (5.23), the MFTM, with its model parameters proposed to be functions of tire inflation pressure and cone index, fits the measured DPC from the lab DTS tests satisfactorily, as displayed in Figure 5.9. In most cases, the experimental data points of the peak drawbar pull coefficient, optimal slip ratio, initial slope in the stable region, and asymptotic drawbar pull coefficient match closely with the model prediction, indicating an acceptable model parameterization.

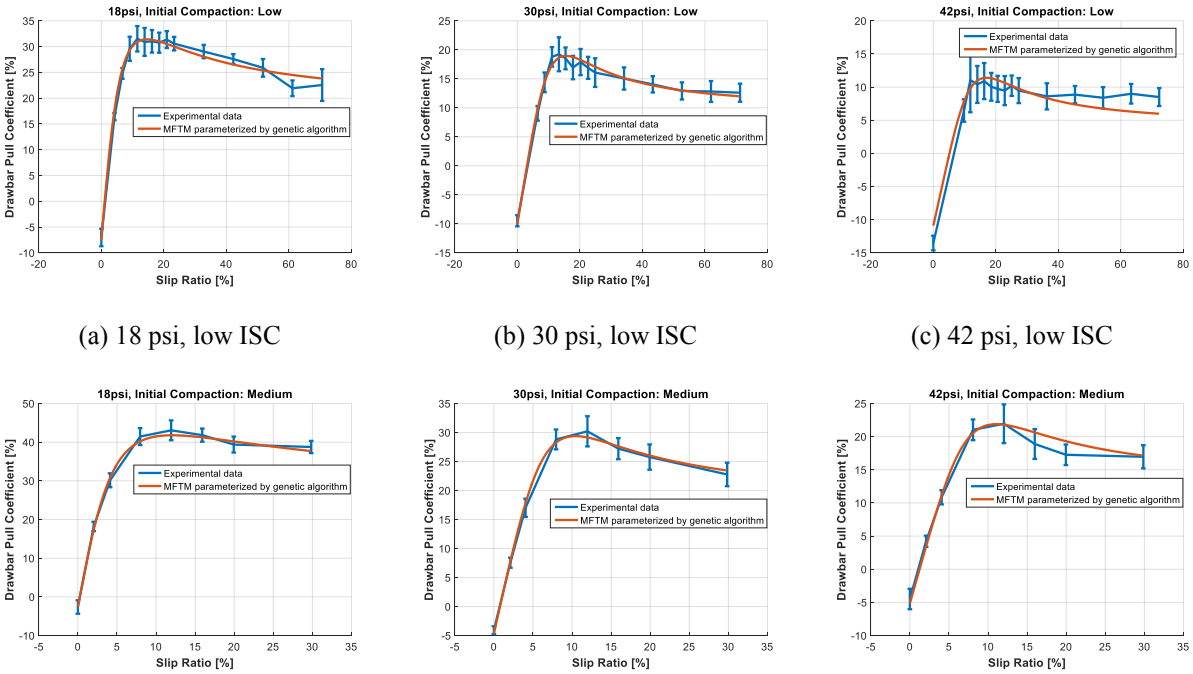

(a) 18 psi, low ISC (b) 30 psi, low ISC (c) 42 psi, low ISC

(d) 18 psi, medium ISC (e) 30 psi, medium ISC (f) 42 psi, medium ISC

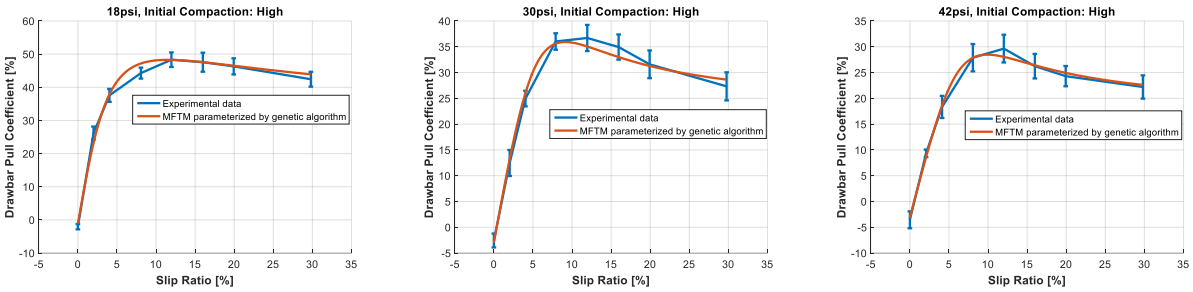

(g) 18 psi, high ISC (h) 30 psi, high ISC (i) 42 psi, high ISC

Figure 5.9: Curve fitting of the MFTM accounting for the influence of initial soil compaction and tire inflation pressure to the measured data of the DPC from the lab DTS tests at the 18 psi, 30 psi, and 42 psi inflation pressure; low, medium, and high initial soil compaction (ISC); and 5 kN normal load.

To validate the proposed Magic Formula tire model that accounts for the change in inflation pressure and soil initial soil compaction, a few laboratory dynamic tire-soil tests (the validation DTS tests) were conducted; their DOE, as shown in Table 5.7, is different from that of the laboratory dynamic tire-soil tests that provide the test data to parameterize the Magic Formula tire model. The test method for these validation DTS tests is nearly the same that is described in Section 4.5.1 except that three different nominal slip ratios were applied in each run of a few tests while only one nominal slip ratio was applied in each run of the lab DTS tests described in Section 4.5.1. Totally, six validation DTS tests were completed.

Table 5.7: Design of experiment for the laboratory dynamic tire-soil tests for the model validation (the validation DTS tests).

Operational parameters	Number of levels	Levels
Nominal normal load [kN]	1	5
Nominal slip ratio [%][a]	7	0[b], 2, 4, 6, 10, 20 ,30
Tire inflation pressure [psi]/[kPa]	2	24/165, 36/248
Rolling radius [mm][c]	2	333.01, 335.98
Soil compaction (CI [kPa], VWC [cm^3/cm^3])[d]	1	(780.37, 0.99%)

[a] Pure longitudinal slip, zero camber angle and toe angle.
[b] Tire is in the towing mode.
[c] The first and second entries are for 24 psi and 36 psi respectively.
[d] The mean values of the CI and VWC measurement data for all the tests at the slightly high initial soil compaction.

The values of CI and inflation pressure in Table 5.7 and the coefficient values in Table 5.6 were substituted to Equations (5.12), (5.18) – (5.23) to calculate the Magic Formula model

parameters. With these Magic Formula model parameters, the predicted drawbar pull coefficient vs. slip ratio curves were produced. The model prediction and the measured drawbar pull coefficient from the validation DTS tests are compared in Figure 5.10.

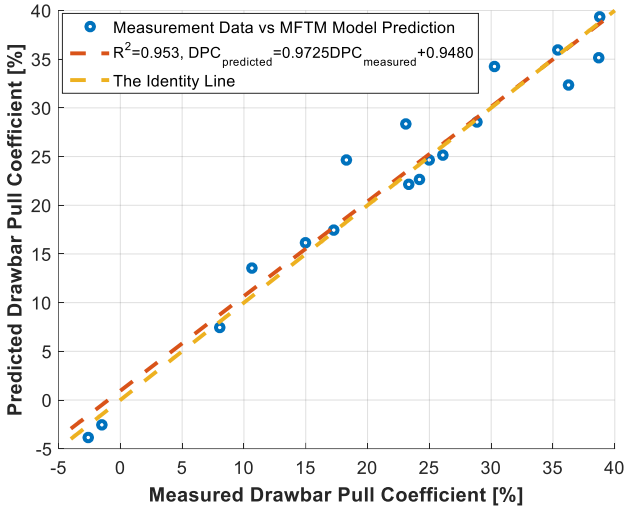

(a) Result of the linear regression to the measured drawbar pull coefficients and predicted drawbar pull coefficients.

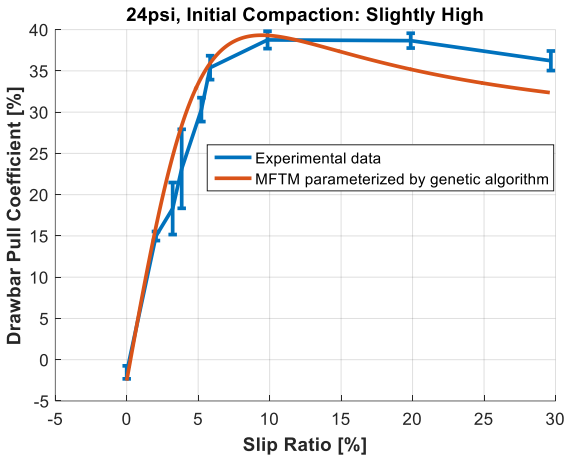

(b) Measured drawbar pull coefficients vs. the MFTM drawbar pull coefficient curve at the 24 psi inflation pressure and slightly high initial soil compaction.

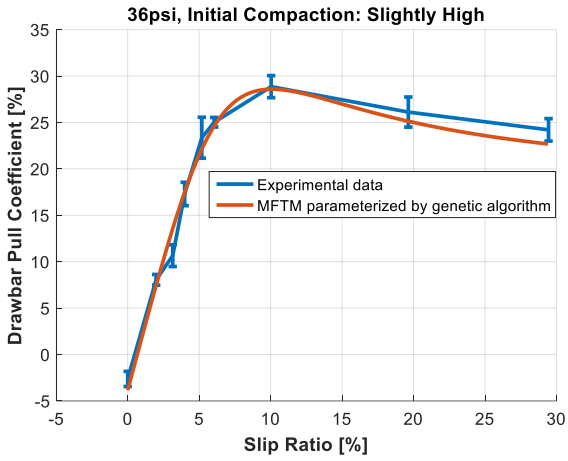

(c) Measured drawbar pull coefficients vs. the MFTM drawbar pull coefficient curve at the 36 psi inflation pressure and slightly high initial soil compaction.

Figure 5.10: Comparison between the MFTM drawbar pull prediction and measured data of drawbar pull coefficient from the lab DTS tests at the 24 psi and 36 psi inflation pressure, 5 kN normal load, and slightly high initial soil compaction. The slightly high initial soil compaction was achieved by 4 trips of the roller compacting.

It can be seen from Figure 5.10 that good agreements between the predicted drawbar pull

coefficients and the measured coefficients have been achieved. The coefficient of determination is 0.95 and very close to 1, which indicates that the scattered points of the DPC prediction and measured DPC are very close to the identity line and hence means that the prediction and measurement are nearly identical. Also, Figure 5.10b and Figure 5.10c show that the initial slope in the stable region, the peak drawbar pull coefficient, and the optimal slip ratio are well captured by the proposed version of MFTM. Little stray on asymptotic drawbar pull coefficient doesn't negate the good match between the model prediction and measured data. It can be concluded that the proposed MFTM is validated against the test data from the validation DTS tests.

5.3 Parameterization of the Pressure-Sinkage Model

The parameterization of the Bekker's pressures-sinkage model was completed by applying a newly proposed method: using the reconstructed ruts from the static tire-soil tests in October 2019. Besides, the measurement data of rut depth from the laboratory dynamic tire-soil tests of 2017 were fed into nonlinear regression analysis to compute the parameters of the modified Bekker's pressure-sinkage model. Compared with the Bekker's pressure-sinkage model, the modified one takes into account the influence of slip sinkage on tire sinkage. In this section, the Bekker's pressure-sinkage model, as well as the proposed parameterization method for the Bekker's model, is introduced first. Next, a slip sinkage model is introduced, followed by its parameterization results.

5.3.1 Parameterization Using Rut Reconstruction

The Bekker's pressure-sinkage model are among the classical terramechanics models. The model parameters of the Bekker's pressure-sinkage model k_c, k_ϕ, n are empirical model parameters. Physically, the Bekker's model characterizes the sinkage of the soil under a plate pressed vertically against the soil; therefore, the sinkage is only the static sinkage (due to the normal load of pressure source).

$$p = \left(\frac{k_c}{b} + k_\phi \right) z^n \tag{5.25}$$

For a wheel or a tire interacting with soil, the soil can be considered compressed in the radial direction; assuming the radial stress on the wheel rim or the tire tread rim is equal to the normal pressure beneath a plate at the same depth [14], the Bekker's pressure-sinkage model has been widely applied in the tire/wheel off-road dynamics modeling. The integration of the pressure (in vertical direction) over the tire-soil contact area is equal to the tire normal load, as indicated by Equation (5.26). It's worth mentioning that Equation (5.26) doesn't need the aforementioned assumption of the radial stress to hold true.

$$F_z = \iint p(x, y) dx dy \tag{5.26}$$

where x is the longitudinal coordinate, and y is the vertical coordinate.

Substituting the Bekker's pressure-sinkage model Equation 5.25 to Equation (5.26) gives the following equation.

$$F_z = \iint \left(\frac{k_c}{b} + k_\phi \right) \left[z(x, y) \right]^n dx dy \tag{5.27}$$

where z is the vertical coordinate as well as the sinkage.

It's extremely difficult yet not impossible to derive the formula of $z(x, y)$; however, the values of (x, y, z) are provided in the reconstructed ruts in Figure 4.21 and Figure 4.22. Assuming the model parameters of the Bekker's pressure-sinkage model remain constant at the same initial soil compaction level of the static tire-soil tests in October 2019, the squared errors, between the normal load calculated by Equation (5.27) and the 5 kN nominal normal load, are summed up for all the six reconstructed ruts at the same initial soil compaction level; an optimization can be run to tune the model parameters of the Bekker's model such that the value of the sum of these squared errors Equation (5.28) is reduced to a small value.

$$\sum \left\{ \iint \left(\frac{k_c}{b} + k_\phi \right) \left[z(x, y) \right]^n dx dy - Fz \right\}^2 \tag{5.28}$$

An optimization program based on the genetic algorithm was written to run optimizations

which obtain three sets of the Bekker's model parameter values for the three different initial soil compaction levels. The reconstructed ruts in Figure 4.21 and Figure 4.22 are fed into Equation (5.28) which is implemented in the optimization program by applying the numerical integration method (the trapezoidal rule). The genetic algorithm here has the same parameter values as the ones in Table 5.2.

Table 5.8 lists the model parameter values and the final values of the cost function computed by the optimization program. The variations in the cost function value at each ISC level is displayed in Figure 5.8. The cost function values are all reduced to values more than ten times as small as the initial value after a few hundred or dozen iterations. The final value of the cost function at the medium ISC level is larger than that at the low or high ISC level, which possibly means that the reconstructed rut data at the medium ISC has worse suitability for the model parameterization.

Table 5.8: Values of the pressure-sinkage model coefficients obtained from the optimization. Optimization is completed at each of the three initial soil compaction (ISC) levels.

Coefficient	Value at low ISC level	Value at medium ISC level	Value at high ISC level
k_c	29.58	106.41	35.93
k_ϕ	77.90	3.52	358.10
n	0.2233	0.3053	0.2525
Final value of the cost function Equation (5.28)	9.15e-2	3.26e-1	2.47e-2

The worse suitability of the reconstructed rut data at the medium ISC for the model parameterization may have several causes. The measurement error in reconstructing the rut could be the first cause. Also, the model parameterization assumes the Bekker's model parameters remain constant at the same initial soil compaction level; however, although at the same initial soil compaction level, the real initial soil compaction behind one of the six reconstructed ruts could differ slightly with that behind another one, which could vary the Bekker's model parameters.

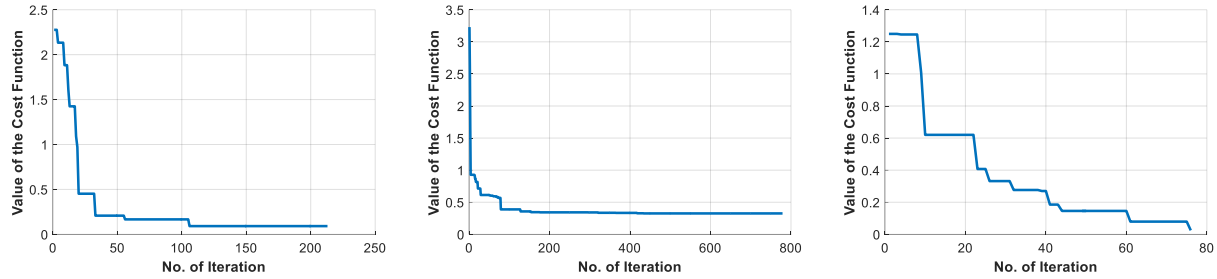

(a) Low initial soil compaction. (b) Medium initial soil compaction (e) High initial soil compaction.

Figure 5.11: Variations in the cost function values in parameterizing the Bekker's pressure-sinkage model by using the reconstructed ruts. The parameterization is completed at each of the three initial soil compaction levels.

The pressure was estimated by using the Bekker's pressure-sinkage model with the coefficient values in the 1st, 2nd , and 3rd columns of Table 5.8 for all the reconstructed ruts (the tire-soil contact area for the statically loaded tire) at the low, medium, and high ISC levels respectively. Next, the integration of the estimated pressure over the entire rut gives the estimated normal load for each of the reconstructed ruts. The estimated tire normal load and pressure distribution on the rut is displayed for all the reconstructed ruts in Figure 5.12, Figure 5.13, and Figure 5.14. The estimated normal load is more accurate at the low or high ISC level than that at the medium ISC level, which makes sense because the final cost function value at the low or high ISC level than that at the medium ISC level. The relative normal load estimation error is always lower than 5.78% and mostly lower than 3%, which indicates acceptable model parameterizations.

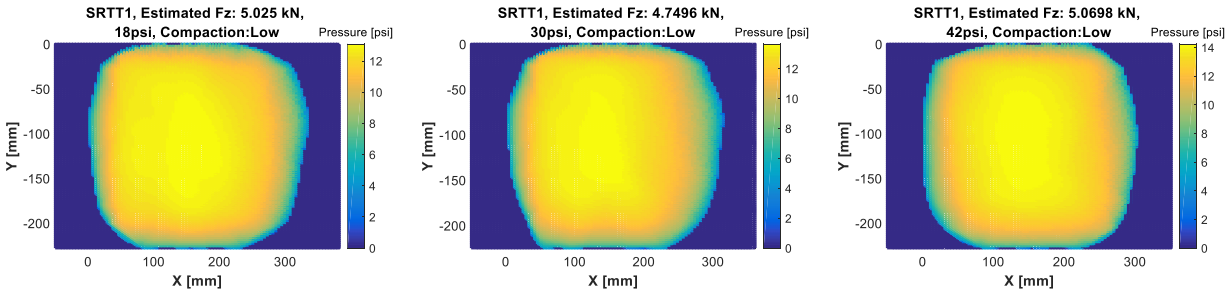

(a) SRTT, 18 psi. (b) SRTT, 30 psi. (c) SRTT, 42 psi.

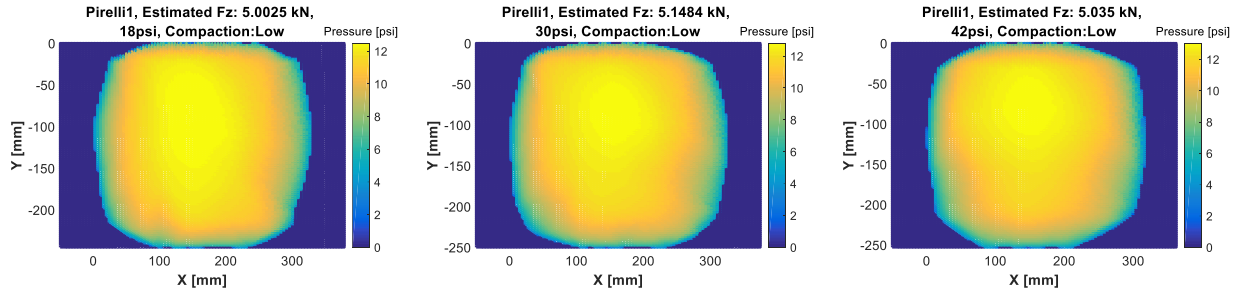

(d) Pirelli, 18 psi. (e) Pirelli, 30 psi. (f) Pirelli, 42 psi.

Figure 5.12: Estimated normal load and pressure distribution in the tire-soil contact area for the tires and soil at the low initial soil compaction in the static tire-soil tests of October 2019. The tires were statically loaded on the soil at 5 kN normal load and 18, 30, or 42 psi inflation pressure.

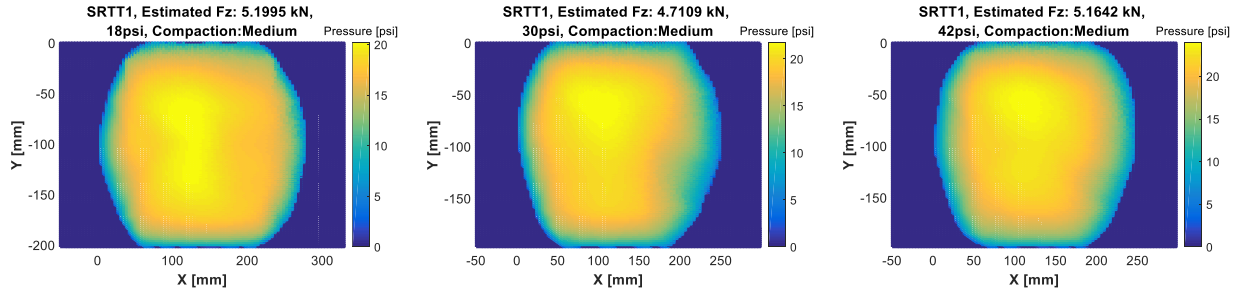

(a) SRTT, 18 psi. (b) SRTT, 30 psi. (c) SRTT, 42 psi.

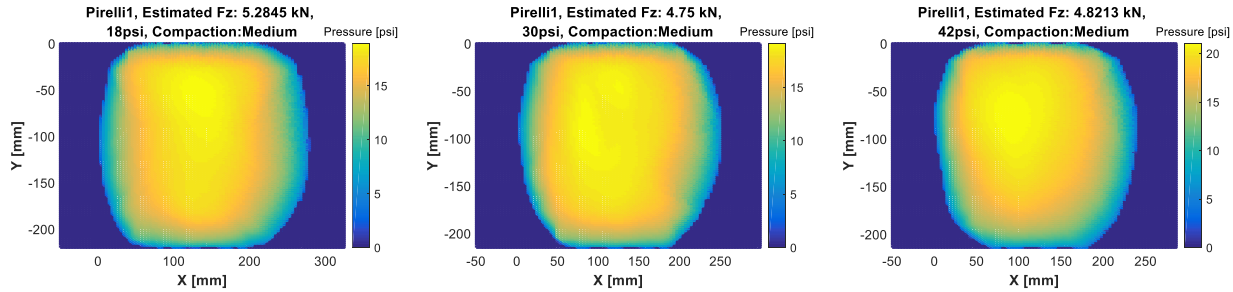

(d) Pirelli, 18 psi. (e) Pirelli, 30 psi. (f) Pirelli, 42 psi.

Figure 5.13: Estimated normal load and pressure distribution in the tire-soil contact area for the tires and soil at the medium initial soil compaction in the static tire-soil tests of October 2019. The tires were statically loaded on the soil at 5 kN normal load and 18, 30, or 42 psi inflation pressure.

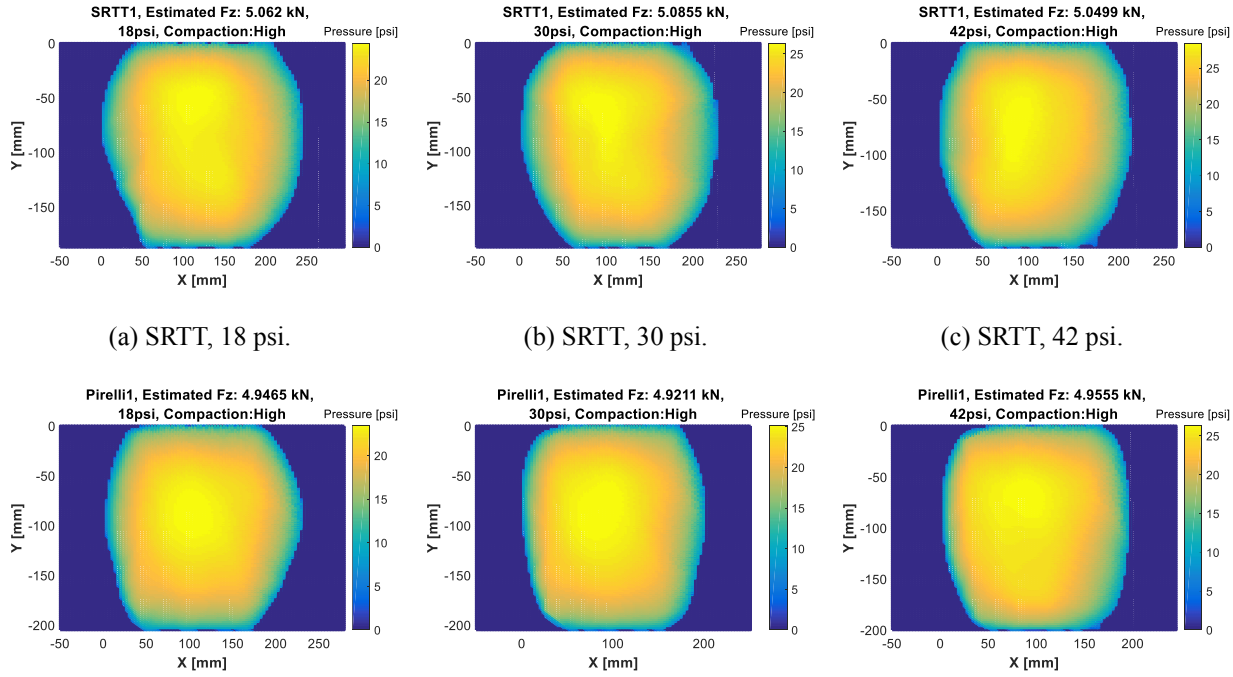

(a) SRTT, 18 psi. (b) SRTT, 30 psi. (c) SRTT, 42 psi.

(d) Pirelli, 18 psi. (e) Pirelli, 30 psi. (f) Pirelli, 42 psi.

Figure 5.14: Estimated normal load and pressure distribution in the tire-soil contact area for the tires and soil at the high initial soil compaction in the static tire-soil tests of October 2019. The tires were statically loaded on the soil at 5 kN normal load and 18, 30, or 42 psi inflation pressure.

It can be seen from Figure 5.12, Figure 5.13, and Figure 5.14 that the maximum pressure increases with inflation pressure when at the same ISC level and with ISC level when at the same inflation pressure. The first trend is due to more penetration and hence larger pressure as the inflation pressure is boosted. As for the second trend, although the sinkage is smaller at higher ISC level, however, the rut area is reduced at higher ISC level, which leads to higher average ground pressure and correspondingly higher maximum pressure.

To validate the parameterized Bekker's pressure-sinkage model (with the parameter values in Table 5.8), additional reconstructed ruts at the same initial soil compaction levels yet different nominal normal load or inflation pressure are needed; the estimation normal load using the parameterized Bekker's model needs to be compared with the nominal normal load.

The parameterization method in this section for the pressure-sinkage models can serve as an alternative method to the traditional method based on the plate-sinkage tests. It may have

some advantage over the traditional method. The reason is that the loading condition of the plate-soil interaction is two dimensional given that the plate is flat, while the loading condition of the tire-soil interaction is three dimensional given that the tire tread surface is curved, which makes the plate-sinkage tests possibly incapable of capturing the real tire-soil interaction physics. However, the proposed parameterization method in this section is based on tire-soil tests; hence the aforementioned incapability of the plate-sinkage tests is not a problem to the proposed method.

5.3.2 Modified Bekker's Pressure-Sinkage Model

The wheel or tire sinkage is not only due to the static sinkage but also due to the slip sinkage per Section 2.1; in many circumstances, slip occurs in the tire-soil or wheel-soil contact patch, generating tangential force that renders the layer of soil in the contact patch peeled off and hence causes the slip sinkage. The Bekker's pressure-sinkage model doesn't account for the slip sinkage. To overcome this drawback, the sinkage exponent of the Bekker's model was proposed to relate slip ratio by [152]:

$$n = n_0 + n_1 s \tag{5.29}$$

Substituting Equation (5.29) into the Equation (5.25) brings out the modified Bekker's model used in this study. Assuming that the tire in the towing mode is in the elastic mode and the tire-soil contact patch has a flattened portion (as portrayed by Figure 4.10) with its width being smaller than its length, Equation (5.30) was proposed to predict the tire sinkage [14]:

$$z_0 = \left(\frac{p_{gr}}{k_c / b_{ts} + k_\phi} \right)^{1/n} \tag{5.30}$$

The average ground pressure is denoted by p_{gr}. Bekker used the average ground pressure to represent the contact pressure in the flattened portion of the tire-soil contact patch [14]. The average ground pressure of the test tire was measured at multiple levels of tire inflation pressure in the static tire deflection test; in this study, the average ground pressure of the test tire can be found in Figure 4.8.

For the same tire moving on the soil in the same soil condition, if the small dimension of the flattened portion of the tire-soil contact patch is its width, the sinkage modulus can be defined as Equation (5.31). For the tire-soil interaction in the laboratory static tire-soil tests of July 2017 and in the laboratory dynamics tire-soil tests of 2017 at slip ratio up to 20%, the sinkage modulus, represented by Equation (5.31), is assumed to remain constant regardless of changes in slip ratio and in tire inflation pressure; this assumption can hold for several reasons:

(1) As indicated by the pressure map collected in the static tire deflection test of November 2016 (Figure 4.5), the width of the contact patch remains to be 176 mm for the 42 psi, 30 psi, and 18 psi tire inflation pressure and 5 kN normal load. Although the tire width is 225 mm, due to the tire design and structure, the flattened part width of the contact patch is smaller than the tire width. It could be assumed that the width of the flattened part of the tire-soil contact patch is the same as the width of the contact patch in the static tire deflection test of November 2016 if the normal load and tire inflation pressure are the same. Therefore, the width of the flattened part of the tire-soil contact patch is considered 176 mm in the lab DTS tests of 2017.

(2) Assuming that the tire-soil contact patch geometry of rolling tire can be represented by Figure 2.1b, and that the loaded radius remains constant for both static tire and rolling tire (with longitudinal speed as low as 6 cm/s per Section 3.1 and slip ratio $\leq$ 20%) at the same normal load, at the same tire inflation pressure, and in the same soil condition (similar to the assumption about loaded radius explained at the beginning of Section 4.4), the length of the flattened part of the tire-soil contact patch is calculated to be 266.56 mm, 201.59 mm, and 159. 43 mm for the 18 psi, 30 psi, and 42 psi tire inflation pressure respectively, and the assumption here ensures a same contact length in the lab DTS tests of 2017 and the lab STS tests of July 2017 at the same normal load, at the same tire inflation pressure, and in the similar soil condition (demonstrated by Table 4.6 and Table 4.9). Since for the 42 psi tire inflation pressure, the 159.43 mm contact length is only slightly smaller than the assumed 176 mm width of the tire-soil contact patch, and given that the smaller dimension of the flattened part of the tire-soil contact patch is the denominator for the coefficient k_c in the Bekker's model, setting the width of the tire-soil contact patch as the denominator for k_c

won't make a big difference compared with setting the contact length as the denominator.

(3) When applying the Bekker's model to compute the motion resistance of rigid wheel, the assumption according to [14] is "the normal pressure acting on the wheel rim is equal to the normal pressure beneath a plate at the same depth" (referred to as "the wheel rim normal pressure assumption" below).. The smallest dimension of the contact patch between the plate and the soil in this assumption is unknown, and at least, the authors of this paper think, not always the width of the plate. However, the wheel width is used in the Bekker's model to compute the motion resistance [14], which contradicts the original definition of the Bekker's model that the smallest dimension of the contact patch is used in the model.

The authors of this paper find "the wheel rim normal pressure assumption" has been adopted in almost all the research that applied either the Bekker's model or the Reece's pressure-sinkage model in the development of semi-empirical wheel off-road dynamics models, such as [87] and [152], and the wheel width was always used in the Bekker's or Reece's model therein, although contradicting the original definition of the Bekker's or Reece's model.

$$k = k_c / b_{ts} + k_\phi \tag{5.31}$$

Combining Equations (5.29) – (5.31), Equation (5.30) that is only for the prediction of tire sinkage in the towing model can be extended to the traction model at positive slip ratios.

$$z_t = \left(\frac{p_{gr}}{k} \right)^{\frac{1}{n_0 + n_1 s}} \tag{5.32}$$

5.3.3 Parameterization Using Data from Lab DTS Tests

At the 18 psi and 42 psi tire inflation pressure, the measurement data of rut depth from the lab DTS tests of 2017 and the measurement data of the average ground pressure from the static tire deflection tests of November 2016 were used in nonlinear regression analysis to parameterize Equation (5.32), and at the 30 psi tire inflation pressure, the measurement data of rut depth from the lab DTS tests of 2017 and the measurement data of the average ground

pressure from the static tire deflection tests of November 2016 were used to validate the parameterized Equation (5.32).

To facilitate the nonlinear regression analysis, Equation (5.32) was rewritten on the logarithmic scale to form the regression model:

$$\ln(p_{gr}) = \ln(k) + (n_0 + n_1 s)\ln(z_t) \qquad 5.33$$

Since the tire and soil condition have remained almost the same in the lab DTS tests of 2017 (Table 4.9) and the width of the tire-soil contact patch is used in Equation (5.31) and assumed constant, the sinkage modulus k and the coefficients n_0 and n_1 that relate slip ratio to the sinkage exponent are constant throughout the lab DTS tests of 2017. It's worth mentioning that the values of the model parameters of Equation (5.32) k, n_0, n_1 obtained in the model parameterization might not be extrapolated to other tires and soil conditions than that specified in this study.

The nonlinear regression analysis was conducted in MATLAB. Only measurement data of rut depth at the slip ratios up to 20% from the lab DTS tests of 2017 were used. The reason is that only when the rut rebound is negligibly small and the amount of the soil displaced to the rut due to the shearing in the tire-soil contact patch is not large, the rut depth can approximate the tire sinkage; in the lab DTS tests of 2017 at the slip ratios larger than 30%, it was observed that the rut depth had much smaller value than the tire sinkage such that the rut depth could not approximate the tire sinkage. Rut rebound was reported to be a function of slip ratio and to be neglected when slip ratio was not very high [87]. The measurement data of rut depth was also compared with the sinkage computed by a sinkage prediction model to validate the model [26].

The nonlinear regression analysis results are presented in Table 5.9. The value of sinkage modulus is relatively big compared with the ones listed in [14], due to the fact that the measured average ground pressure for the test tire is relatively large, and the measured rut depth (approximating the sinkage) is relatively small compared with the sinkage and pressure represented by the sinkage-pressure plots in [14]. Also, because the width of the tire-soil contact patch is assumed constant, the values of coefficients k_c and k_ϕ cannot be separated

from the value of the sinkage modulus in the nonlinear regression analysis.

Table 5.9: Nonlinear regression analysis outputs about the modified Bekker's pressure-sinkage model.

Coefficient	Value
n_0	1.996
n_1	1.266
k	3.306e+5
R^2	0.630
RMSE	0.159

The value of R^2 Table 5.9 is not large and close to one. This indicates that perfect fitting of the test data at 42 psi and 18 psi to Equation (5.32) is not obtained. However, considering that the largest relative error is 13% and most relative errors are smaller than 10%, per Figure 5.15a and Figure 5.15b, the fit between the test data (at 42 psi and 18 psi) and Equation (5.32) at the values of model parameters listed in Table 5.9 is deemed acceptable. For the model validation, the measurements of rut depth at 30 psi are compared with the rut depth calculated by Equation (5.32) that was parameterized by using the test data at 42 psi and 18 psi (the model parameter values applied are listed in Table 5.9), as shown in Figure 5.15c; the largest relative error is 9.7% and only two relative errors are larger than 6% (Figure 5.15e). Given these numbers, it can be concluded that, within the scope of this study, Equation (5.32) predicts tire sinkage within acceptable errors, and the parameterization method by using the test data collected from the lab DTS tests of 2017 works pretty well.

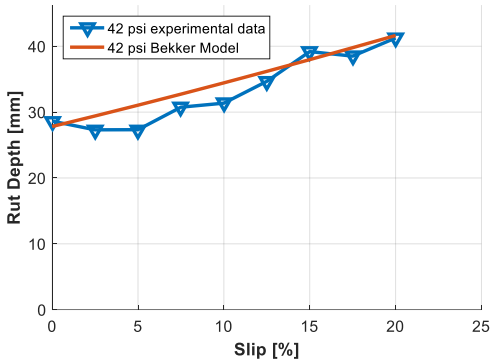

(a) Measurements of rut depth (used to parameterize Equation (5.32)) and the rut depth calculated by Equation (5.32) at 42 psi tire inflation pressure.

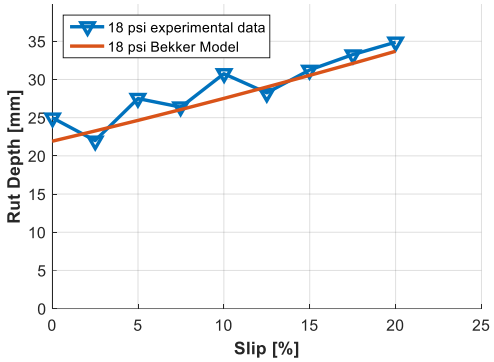

(b) Measurements of rut depth (used to parameterize Equation (5.32)) and the rut depth calculated by Equation (5.32) at 18 psi tire inflation pressure.

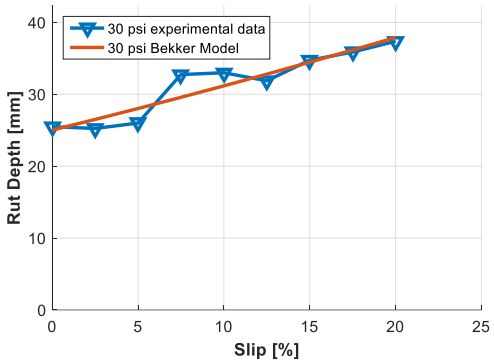

(c) Measurements of rut depth and the rut depth calculated by Equation (5.32) at 30 psi tire inflation pressure.

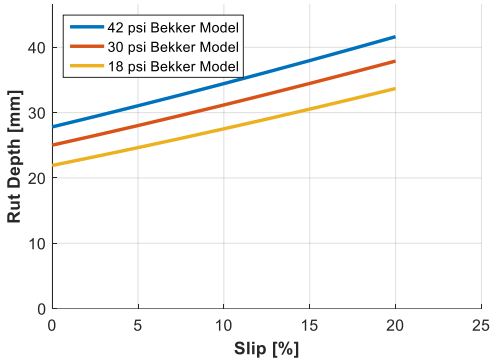

(d) Rut depth calculated by Equation (5.32) for all three levels of the test tire inflation pressure.

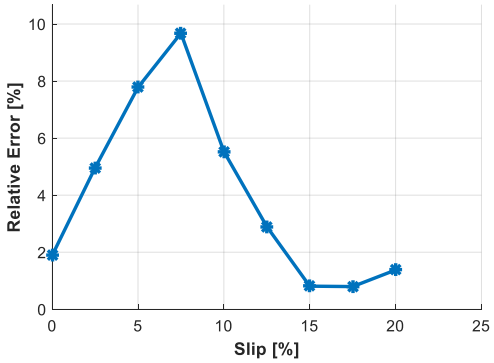

(e) Relative errors between the rut depth measurements and the rut depth calculated by Equation (5.32) at 30 psi tire inflation pressure.

Figure 5.15: Variations in rut depth with slip (≤ 20%) for all the three test tire inflation pressure levels.

Chapter 6

Conclusions and Future Work

This chapter draws conclusions and makes comments for the previous chapters of this dissertation. A list of publications based on this study is also included. Finally, the future research direction is pointed out.

6.1 Research Outcomes Summary

The research documented by this dissertation aimed to develop model parameterization methods for terramechanics models and tire models and test methods to study the tractive performance of tire on soil and soil response to tire traffic at various levels of operational parameters. The operational parameters are tire inflation pressure, slip ratio, initial soil compaction, tire normal load, and number of passes. The experimental tests of this research were completed at the TMVS Laboratory, Virginia Tech.

This research began with a general literature review on multiple aspects concerned in the study of tire-soil interaction: the soil condition characterization and parameters and relationships of interest in the experimental tests, the modeling approach, existing models and their parameterization methods, parameters and relationships of interest in the tire off-road traction dynamics, the effect of tire inflation pressure on tire tractive performance, and basic terminology in tire-soil interaction. It has been founded that:

(1) Very few experimental tests were completed at a wide range of slip ratio, tire inflation pressure, and initial soil compaction to study the combined effect of these three operational parameters on tire off-road tractive performance and soil response to tire traffic.

(2) The parameterization of terramechanics model for existing tire off-road dynamics models relied only on conventional model parameterization method such as the plate-sinkage test and plate-shear test, both of which is suspected not to capture the tire-soil interaction

adequately.

(3) The Magic formula was never adapted to account for the influence of large inflation pressure and initial soil compaction changes on tire off-road tractive performance.

These three findings from the literature review are the three main research motivations for this research.

As the experimental part of this research, a series of tire, soil, and tire-soil tests were conducted in the lab for a 225/60R16 97S Uniroyal (Michelin) Standard Reference Test Tire and a loamy sand. In the laboratory soil properties tests, bulk density, gravimetric water content, and cone index of the test soil were measured under various soil conditions. The water content of the test soil was found to be very low. At such a low level of water content, a sample of test soil with a high cone index larger than 1000 kPa had larger bulk density than the sample with a low cone index around 300 kPa did. Based on the measurement data, it could be concluded that the cone index value reflects the soil compaction (characterized by bulk density) of the test dry soil;

The loaded radius and the pressure distribution in the contact patch were measured under multiple levels of tire inflation pressure and normal load in the static tire deflection tests. The pressure map recorded indicates that as the tire inflation pressure became smaller, the location where there was relatively high inflation pressure shifted from the center of the contact patch to the rim sides of the contact patch. Also, the tire normal load was found to influence the average ground pressure less than the tire inflation pressure, although increases in both of them leads to increase in average ground pressure.

The data recorded from the laboratory static tire-soil tests showed that the initial soil compaction would influence the depth of the rut formed by the compaction of the non-rolling, loaded tire. The initial soil compaction seems to the primary influence on the rut depth, while both of the normal load and inflation pressure seem to be the secondary influence. By contrast, in terms of the influences on the loaded radius of the tire on the soil, the normal load and inflation pressure are the primary influences, while the initial soil compaction is the secondary influence. Looking at the rut profile in the static tire-soil tests of October 2019,

reconstructed by the developed method, the rut area tends to grow larger with the decrease in initial soil compaction area or inflation pressure. Other trends of parameters of interest when operational parameters change are summarized in Table 6.1.

By checking the measured rolling radius from the lab free-rolling tire-soil tests against the estimated rolling radius from the static tire-soil test of July 2017, the proposed estimation method is working acceptably at the medium and high initial soil compaction level and 5 kN normal load Band tends to give more accurate estimation when the soil gets more compacted (harder). Comparing the estimated rolling radius of the tire on the rigid surface and the measured rolling radius of the tire on soft soil, at the same 5 kN normal load and inflation pressure, the difference is ranging from 18.2 mm to 38.3 mm, which demonstrates the influence of initial soil compaction on the rolling radius. When the soil is at the low initial soil compaction, the measured rolling radius is larger than the unloaded radius,

Table 6.1: Trends of tire performance and soil response w.r.t. the changes in operational parameters in the laboratory static tire-soil tests.

Tire (non-rolling) and soil parameters / Change in operational parameters	Loaded radius	Rut depth	Rut length	Rut width	Rut area
Inflation pressure ↑	↑	↑	↓	→	↓
Initial soil compaction ↑	↓	↓	↓	↓	↓
Normal load ↑	↓	→ or ↑ [b]	N/A[a]	N/A[a]	N/A[a]

[a] Not measured in the static tier-soil tests at more than three levels of the operational parameter, and hence N/A.
[b] Only doesn't change in a very few tests at the low initial soil compaction level; increases with normal load in the rest of the static tire-soil tests.

From the test data from the laboratory dynamic tire-soil tests, it can be seen that the optimal slip ratio that corresponds to the maximum drawbar pull coefficient is around 12%. At the medium or high initial soil compaction level, the rut fluctuation already has occurred at 12% slip ratio, with the fluctuation frequency that tends to increase with slip ratio, while it doesn't appear at a slip ratio lower than or equal to 8%. Also at the medium or high initial soil compaction level, the optimal slip ratio that corresponds to the maximum drawbar efficiency is lower than the 12% optimal slip ratio for the drawbar pull coefficient; the optimal slip ratio for the drawbar efficiency tends to shift to the left as the inflation pressure decreases. A new multi-pass effect phenomenon is discovered: when the slip ratio is low such

that the rut fluctuation doesn't occur, the drawbar pull coefficient or drawbar efficiency increases with the number of passes at that slip ratio; when the slip ratio is high enough such that rut fluctuation appears, the drawbar pull coefficient or drawbar efficiency decreases with the number of passes at that slip ratio. The trends of tire performance parameters and soil response parameters w.r.t. to changes in operational parameters are summarized in Table 6.2 and Table 6.3

Table 6.2: Trends of tire performance and soil response w.r.t. the changes in operational parameters in the laboratory dynamic tire-soil tests in towing mode (free-rolling mode).

Tire and soil parameters / Change in operational parameters	Motion resistance coefficient	Motion resistance	Rolling radius	Rut depth	Tire sinkage	Cone Index
Inflation pressure ↑	↑	↑	↑	↑	N/A[a]	N/A
Initial soil compaction ↑	↓	↓	↓	↓	N/A[a]	↑
Normal load ↑	→ or ↓	→ or ↑	→ or ↓	→ or ↑	N/A[a]	N/A
Number of passes ↑	↓	↓	↓	↑	↑	↑

[a] Not measured in the laboratory dynamic tire-soil tests in free-rolling mode, and hence N/A.

Table 6.3: Trends of tire performance and soil response w.r.t. the changes in operational parameters in the laboratory dynamic tire-soil tests in traction mode.

Tire and soil parameters / Change in operational parameters	Drawbar pull coefficient	Drawbar efficiency	Rut depth	Rut width	Tire sinkage	Contact patch length	Cone Index
Inflation pressure ↑	↓	↓	↑	↓	↑	↓	N/A
Initial soil compaction ↑	↑	↑	↓	↓	↓	↓	↑
Slip ratio ↑	↑ ↓[b]	↑ ↓[b]	↑	↑	↑	↑	N/A
Number of passes ↑	↑ or ↓[c]	↑ or ↓[c]	↑	N/A[a]	↑	N/A[a]	↑

[a] Not measured in the laboratory dynamic tire-soil tests in traction mode, and hence N/A.
[b] Increase first before the optimal slip for the peak drawbar pull coefficient or drawbar efficiency, then decrease after the optimal slip.
[c] Increase if the rut fluctuation doesn't appear; decrease otherwise.

The test data collected from the series of the tire, soil and tire-soil tests was fed into a bulk density estimation model, the Magic Formula tire model, a modified Magic Formula tire model, the modified Bekker's pressure-sinkage model for their parameterization.

The bulk density estimation model discussed herein has the potential of application in on-site compaction evaluation, as the bulk density predicted by this model, once parameterized,

could follow the measurement data of bulk density from the lab soil properties tests.

The Magic Formula tire model seems another useful empirical model to predict the tire drawbar pull in off-road condition; it fitted the measurement data of drawbar pull from the lab dynamic tire-soil tests of 2017 adequately and simultaneously accounted for the influence of large variations in tire inflation pressure on drawbar pull. A modified Magic Formula tire model was proposed in this dissertation to account for the combined influence of tire inflation pressure and initial soil compaction, parameterized by the test data from the lab dynamic tire-soil tests, and validated by the test data from other lab dynamic tire-soil tests conducted with model validation purposes.

The Bekker's pressure-sinkage model was parameterized by a newly proposed method based on the rut reconstruction from the static tire-soil tests in October 2019. The Bekker's pressure-sinkage model was modified to account for the slip sinkage effect. The measurement data of rut depth at slip ratios up to 20% and at two levels of tire inflation pressure from the lab dynamic tire-soil tests of 2017 and the measurement data of the average ground pressure from the static tire deflection tests of November 2016 were used to parameterize the modified Bekker's pressure-sinkage model; the measurement data of rut depth at the other level of tire inflation pressure fitted the parameterized model acceptably, which demonstrates the usefulness of the sinkage exponent-slip model implemented and Bekker's pressure-sinkage model in predicting rut depth at various levels of slip ratio. The parameterization methods for pressure-sinkage models proposed herein can be particularly suited for determining the model parameters of pressure-sinkage model for tire off-road dynamics modeling.

Based on this study, journal papers, conference papers, and oral presentations have been produced as follows.

6.1.1 Journals

1. R. He, C. Sandu, and J. E. Osorio, "Systematic tests for study of tire traction on soft soil: Part I – Experimental data collection," J. Terramechanics, vol. 85, pp.59-76, 2019.

2. R. He, C. Sandu, and J. E. Osorio, "Systematic tests for study of tire tractive

performance on soft soil: Part II – Parameterization of terramechanics model and tire model," J. Terramechanics, pp.77-88, 2019.

3. V. Ivanov, D. Savitski, K. Augsburg, S. Els, C.-J. Kat, T. Botha, M. Dhaens, C. Sandu, R. He, S. M. Granda, A. G. A. Vazquez, and A. C. Victorino, "Challenges of integrated vehicle chassis control: Some findings of the European project EVE," *IEEJ J. Ind. Appl.*, vol. 8, no. 2, 2019.

4. R. He, C. Sandu, A. K. Khan, A. G. Guthrie, P. S. Els, and H. A. Hamersma, "Review of terramechanics models and their applicability to real-time applications," *J. Terramechanics*, vol. 81, pp.3-22, 2019.

5. R. He, E. Jimenez, D. Savitski, C. Sandu, and V. Ivanov., " Investigating the parameterization of Dugoff tire model using experimental tire-ice data," *SAE Int. J. Passeng. Cars - Mech. Syst.*, vol. 10, no. 1, pp.83-92, 2017.

6. D. Savitski, D. Schleinin, V. Ivanov, K. Augsburg, E. Jimenez, R. He, C. Sandu, and P. Barber, "Improvement of traction performance and off-road mobility for a vehicle with four individual electric motors: Driving over icy road," *J. Terramechanics*, vol. 69, pp.33-43, 2017.

6.1.2 Peer Reviewed Conference Papers

1. R. He, C. Sandu, and J. E. Osorio, "Modeling and Experimental Study of Tire Motion Resistance on Soft Soil," in *Proceedings of the 15th European-African Regional Conference of the ISTVS, Prague, September 8 – 11, 2019*, 2019, pp. 1-13.

2. R. He, M. N. Shenvi, H. Mousavi, C. Sandu, K. Braun, R. Kruger, and P. S. Els, "Updates of International Society for Terrain-Vehicle Systems Standards," in *Proceedings of the 15th European-African Regional Conference of the ISTVS, Prague, September 8 – 11, 2019*, 2019, pp. 1-91.

3. R. He, A. K. Khan, A. G. Guthrie, C. Sandu, and P. S. Els, "A technical survey on terminology , testing methodologies , and equipment used in modeling and

parameterization of soft soil for vehicular applications," in *Proceedings of the 19th International and 14th European-African Regional Conference of the ISTVS, Budapest, September 25-27, 2017*, 2017, pp. 1–39.

4. R. He, C. Sandu, and J. E. Osorio, "Investigating the difference of the effective rolling radius of a tire on a soft soil and a rigid surface," in *Proceedings of the 19th International and 14th European-African Regional Conference of the ISTVS, Budapest, September 25-27, 2017*, 2017, pp. 1–16.

5. R. He, C. Sandu, and J. E. Osorio, "Investigating the parameterization of Magic Formula tire model using data from dynamic tire-soil tests," in *Proceedings of the 10th Asia-Pacific Conference of the ISTVS, Kyoto, July 11–13, 2018*, 2018, pp. 1–18.

6. R. He, E. Jimenez, D. Savitski, C. Sandu, and V. Ivanov, "Investigating the parameterization of Dugoff tire model using experimental tire-ice data," in *SAE 2016 Commercial Vehicle Engineering Congress*, 2016, pp. 1–10.

6.1.3 Oral Presentations

1. R. He, C. Sandu, "A technical survey on equipment and techniques for testing and parametrization of soft soil for vehicular applications," in *the 8th ISTVS Americas Regional Conference, Troy, MI, September 12-14, 2016*.

6.1.4 Poster Presentations

1. R. He, C. Sandu, and J. E. Osorio, "Modeling and Experimental Study of Tire Motion Resistance on Soft Soil," in *Proceedings of the 15th European-African Regional Conference of the ISTVS, Prague, September 8 – 11, 2019*, 2019, pp. 1-13.

2. R. He, M. N. Shenvi, H. Mousavi, C. Sandu, K. Braun, R. Kruger, and P. S. Els, "Updates of International Society for Terrain-Vehicle Systems Standards," in *Proceedings of the 15th European-African Regional Conference of the ISTVS, Prague, September 8 – 11, 2019*, 2019, pp. 1-91.

3. R. He, C. Sandu, and J. E. Osorio, “Investigating the parameterization of Magic Formula tire model using data from dynamic tire-soil tests,” in *the 10th Asia-Pacific Conference of the ISTVS, Kyoto, July 11–13, 2018.*

4. R. He, A. G. Guthrie, C. Sandu, and P. S. Els, “Systematic testing and parameterization of soft soil for vehicular applications,” in *the 10th Asia-Pacific Conference of the ISTVS, Kyoto, July 11–13, 2018.*

6.2 Research Benefits and Future Research Recommendations

The research presented in this dissertation has the following benefits.

(1) Based on the influence of operational parameters on the tire tractive performance and soil behavior, as described in this dissertation, suggestions could be given to the tire or off-road vehicle manufacturers for the tire operation on soft soil to maximize the tire tractive performance and minimize the post-traffic soil compaction.

(2) The drawbar pull coefficient vs slip ratio plots at various levels of initial soil compaction could be useful to the path planning for off-road vehicles on a mission and to the development of the traction controller for off-road conditions and the soil compaction estimation algorithm.

(3) The test data presented in this dissertation can be used to validate high fidelity tire off-road dynamics models, such as the FEM or DEM models. Also, the test data can be used in a comparison with the test data from in-situ dynamic tire-soil tests, although it’s difficult yet not impossible to control the tire normal load around a constant value in the in-situ dynamic tire-soil tests.

A few research topics are worth investigating as the extension of the research presented in this dissertation:

Varying Tire Normal Load in Lab DTS Test

In the lab DTS tests per Section 4.5, only tire inflation pressure and initial soil compaction

varied, while nominal tire normal load remained almost unchanged. Varying the nominal tire normal load in lab DTS tests will be beneficial in several ways: 1. The test data can be analyzed to study the combined influence of tire inflation pressure, tire normal load, initial soil compaction on tire tractive performance and soil response to tire traffic; 2. The test data can be useful to developing the empirical or semi-empirical tire traction model that sets the model inputs to be tire normal load, tire inflation pressure, and soil parameters that characterize the initial soil compaction, e.g., the Magic Formula model parameters are set to be functions of the tire normal load, tire inflation pressure, and soil parameters.

Parameterization Method Possibly Based on Tire-Soil Test for Shear Stress-Shear Displacement Model

The parameterization method proposed for the modified Bekker's pressure-sinkage method can be applied to determine some soil parameters of the semi-empirical tire off-road dynamics model (the Senatore & Sandu model) recorded in [153]. However, to fully parameterize the Senatore & Sandu model, a parameterization method for shear stress-shear displacement model must be developed, the experimental part of the parameterization method is supposed to capture the shearing behavior of tire on soft soil sufficiently while the conventional plate-shear test cannot. After the parameterization is completed to the Senatore & Sandu model, the model can be joined with a multiple-DOF vehicle model, such as the ones in the literature [154], [155], or a multi-body dynamic vehicle model, like the one in the literature [156], for the development of traction controller that can strike a balance between the traction, drawbar efficiency, and the post-traffic soil compaction.

Adaptive Control Strategy for Tire Normal Load Control of Terramechanics Rig

The normal load controller of the T-Rig is a simple PID controller with constant PID gains. Its performance at high slip ratios is relatively poor compared with that at low or medium slip ratios. An adaptive control strategy could be developed for the normal load controller of the T-Rig such that the PID gains vary with slip ratio and even initial soil compaction to track the nominal tire normal load.

Appendix A

Rut Profile Image

Pictures were taken of the rut after each lab DTS tests of 2019, as shown in Figure A. 1 – Figure A. 6.

(a) Free rolling.

(b) 2% nominal slip.

(c) 4% nominal slip.

(d) 8% nominal slip.

(e) 12% nominal slip.

(f) 16% nominal slip.

(g) 20% nominal slip.

(h) 30% nominal slip.

Figure A. 1: Rut formed by the tire traffic in the laboratory dynamic tire-soil tests of 2019 at 18 psi inflation pressure and medium initial soil compaction level.

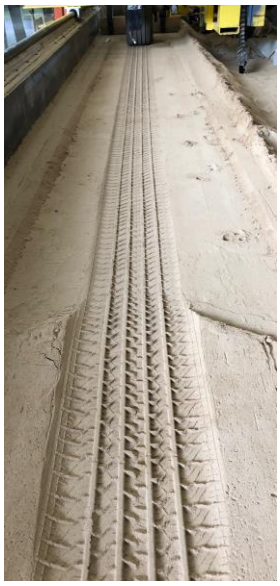

(a) Free rolling.

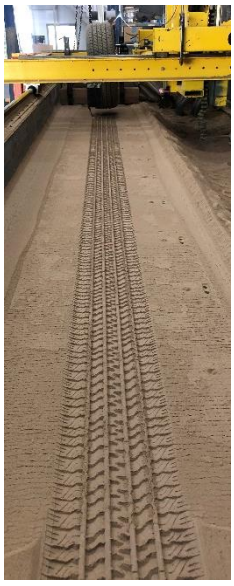

(b) 2% nominal slip.

(c) 4% nominal slip.

(d) 8% nominal slip.

(e) 12% nominal slip.

(f) 16% nominal slip.

(g) 20% nominal slip.

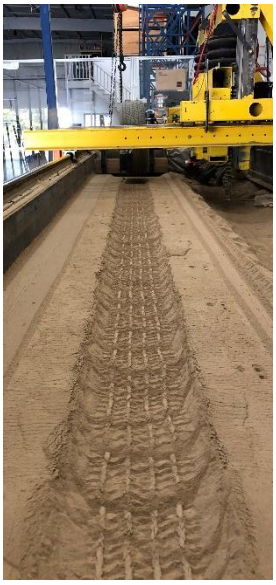

(h) 30% nominal slip.

Figure A. 2: Rut formed by the tire traffic in the laboratory dynamic tire-soil tests of 2019 at 30 psi inflation pressure and medium initial soil compaction level.

(a) Free rolling. (b) 2% nominal slip. (c) 4% nominal slip. (d) 8% nominal slip.

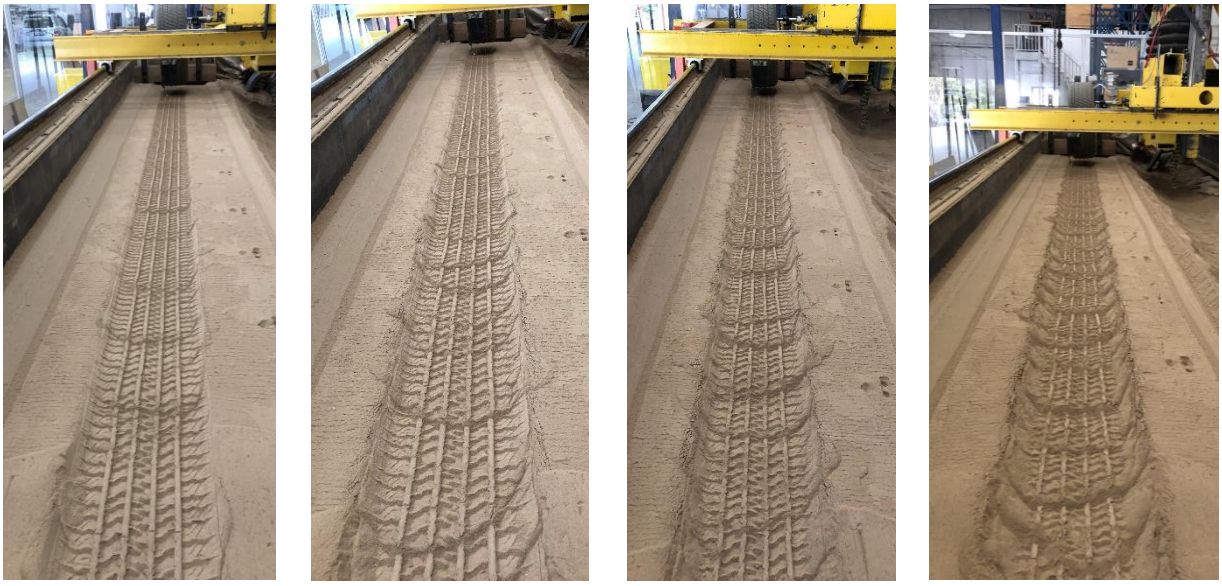

(e) 12% nominal slip. (f) 16% nominal slip. (g) 20% nominal slip. (h) 30% nominal slip.

Figure A. 3: Rut formed by the tire traffic in the laboratory dynamic tire-soil tests of 2019 at 42 psi inflation pressure and medium initial soil compaction level.

(a) Free rolling.

(b) 2% nominal slip.

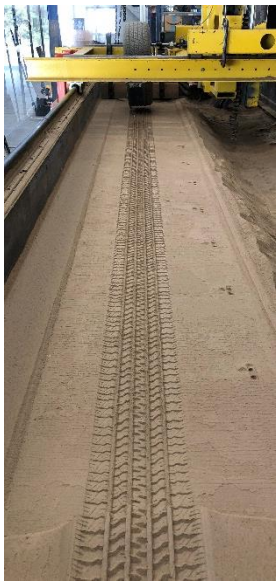

(c) 4% nominal slip.

(d) 8% nominal slip.

(e) 12% nominal slip.

(f) 16% nominal slip.

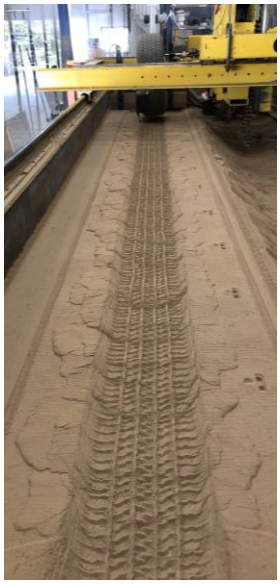

(g) 20% nominal slip.

(h) 30% nominal slip.

Figure A. 4: Rut formed by the tire traffic in the laboratory dynamic tire-soil tests of 2019 at 18 psi inflation pressure and high initial soil compaction level.

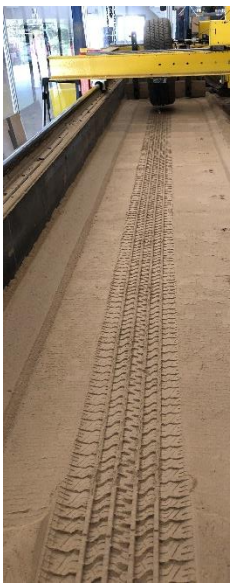

(a) Free rolling.

(b) 2% nominal slip.

(c) 4% nominal slip.

(d) 8% nominal slip.

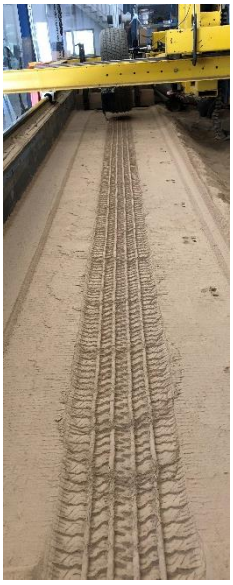

(e) 12% nominal slip.

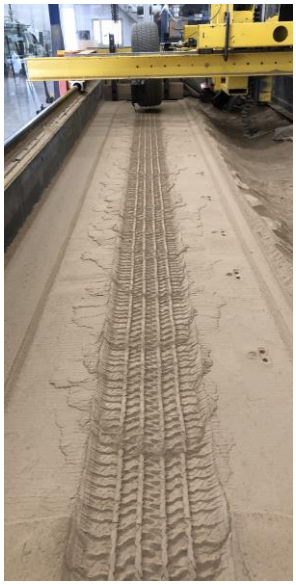

(f) 16% nominal slip.

(g) 20% nominal slip.

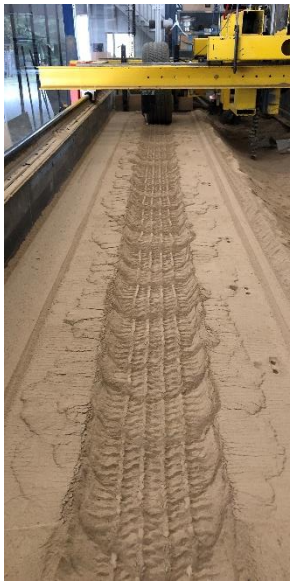

(h) 30% nominal slip.

Figure A. 5: Rut formed by the tire traffic in the laboratory dynamic tire-soil tests of 2019 at 30 psi inflation pressure and high initial soil compaction level.

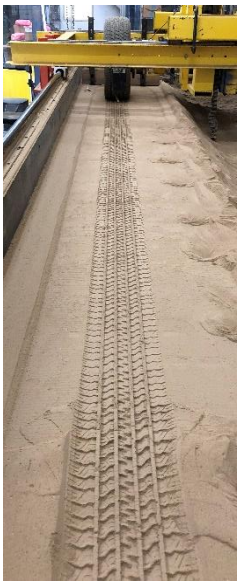

(a) Free rolling.

(b) 2% nominal slip.

(c) 4% nominal slip.

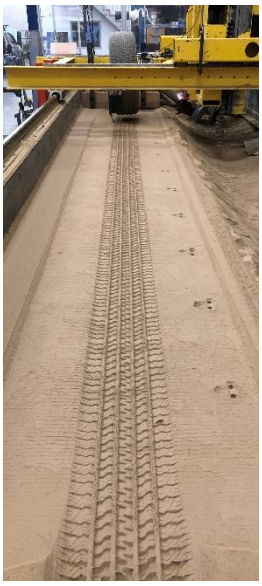

(d) 8% nominal slip.

(e) 12% nominal slip.

(f) 16% nominal slip.

(g) 20% nominal slip.

(h) 30% nominal slip.

Figure A. 6: Rut formed by the tire traffic in the laboratory dynamic tire-soil tests of 2019 at 42 psi inflation pressure and high initial soil compaction level.

Bibliography

[1] J. Y. Wong, *Terramechanics and off-road vehicle engineering: terrain behaviour, off-road vehicle performance and design*, 2nd ed. Oxford: Butterworth-Heinemann, 2009.

[2] ARMY TECHNOLOGY, "NIMR Wheeled Armoured Military Vehicles." [Online]. Available: https://www.army-technology.com/projects/nimr-armoured-vehicles-uae-emirates/.

[3] John Deere, "Equipment Application - Commercial Building." [Online]. Available: https://www.deere.com/en/construction/.

[4] Jackson County Chamber of Commerce, "Antique Tractor Pull." [Online]. Available: http://www.jacksoncounty.com/antique-tractor-pull.

[5] M. Schepke and BMW Group, "Dakar Rally 2019 – Second place for Nani Roma," 2019. [Online]. Available: https://www.press.bmwgroup.com/global/article/detail/T0290343EN/dakar-rally-2019-–-second-place-for-nani-roma?language=en.

[6] B. D. Soane, P. S. Blackwell, J. W. Dickson, and D. J. Painter, "Compaction by agricultural vehicles: a review II. Compaction under tyres and other running gear," *Soil Tillage Res.*, vol. 1, pp. 373–400, 1980.

[7] J. P. Pauwelussen and L. Laib, "Exploration of the Magic Formula as a basis for the modelling of soil-tyre interaction," in *Proceedings of the 7th European ISTVS Conference*, 1997, pp. 341–359.

[8] B. Maclaurin, "Using a modified version of the Magic Formula to describe the traction/slip relationships of tyres in soft cohesive soils," *J. Terramechanics*, vol. 52, no. 1, pp. 1–7, 2014.

[9] G. Stewart, "Heavy Equipment and Soil Compaction - Can large tires and low inflation pressures solve all your problems?," 2013. [Online]. Available: http://www.omafra.gov.on.ca/english/crops/field/news/croptalk/2013/ct-1113a1.htm.

[10] R. He, C. Sandu, A. K. Khan, A. G. Guthrie, P. Schalk Els, and H. A. Hamersma, "Review of terramechanics models and their applicability to real-time applications," *J. Terramechanics*, vol. 81, pp. 3–22, 2019.

[11] R. He, C. Sandu, and J. E. Osorio, "Systematic tests for study of tire tractive performance on soft soil: Part I – Experimental data collection," *J. Terramechanics*, vol. 85, pp. 59–76, 2019.

[12] R. He, C. Sandu, and J. E. Osorio, "Systematic tests for study of tire tractive performance on soft soil: Part II – Parameterization of terramechanics model and tire model," *J. Terramechanics*, vol. 85, pp. 77–88, 2019.

[13] C. Senatore and C. Sandu, "Off-road tire modeling and the multi-pass effect for vehicle dynamics simulation," *J. Terramechanics*, vol. 48, no. 4, pp. 265–276, 2011.

[14] J. Y. Wong, *Theory of ground vehicles*, 4th ed. John Wiley & Sons, 2008.

[15] T. R. Botha, P. S. Els, S. A. Shoop, C. M. Becker, and A. Sopher, “Three-dimensional rut profile measurement in snow and mud,” in *Proceedings of the 8th ISTVS Americas Regional Conference. Troy, MI*, 2016.

[16] M. P. Meyer, I. R. Ehrlich, D. Sloss, N. R. Murphy, R. D. Wismer, and T. Czako, “International society for terrain-vehicle systems standards,” *J. Terramechanics*, vol. 14, no. 3, pp. 153–182, 1977.

[17] B. J. Chan, “Development of an off-road capable tire model for vehicle dynamics simulations,” Virgnia Tech, 2008.

[18] R. Rajamani, *Vehicle Dynamics and Control*, 2nd ed. Springer US, 2012.

[19] R. N. Jazar, *Vehicle Dynamics: Theory and Application*, 2nd ed. Springer-Verlag New York, 2014.

[20] H. B. Pacejka, *Tire and Vehicle Dynamics*, 2nd ed. Butterworth-Heinemann, 2005.

[21] H. D. Kutzbach, A. Bürger, and S. Böttinger, “Rolling radii and moment arm of the wheel load for pneumatic tyres,” *J. Terramechanics*, vol. 82, pp. 13–21, 2019.

[22] F. M. Zoz and R. D. Grisso, *Traction and tractor performance*. St. Joseph, Michigan: American Society of Agricultural Engineers, 2003.

[23] T. Muro and J. O’Brien, *Terramechanics: land locomotion mechanics*, 1st ed. CRC Press, 2004.

[24] M. I. Lyasko, “How to calculate the effect of soil conditions on tractive performance,” *J. Terramechanics*, vol. 47, no. 6, pp. 423–445, 2010.

[25] J.-Y. Wong and A. R. Reece, “Prediction of rigid wheel performance based on the analysis of soil-wheel stresses. Part II. Towed rigid wheels,” *J. Terramechanics*, vol. 4, no. 2, pp. 7–25, 1967.

[26] M. Lyasko, “Slip sinkage effect in soil-vehicle mechanics,” *J. Terramechanics*, vol. 47, no. 1, pp. 21–31, 2010.

[27] D. R. Lee and K. U. Kim, “Effect of Inflation Pressure on tractive Performance of Bias-ply Tires,” *J. Terramechanics*, vol. 34, no. 3, pp. 187–208, 1997.

[28] B. D. Soane, P. S. Blackwell, J. W. Dickson, and D. J. Painter, “Compaction by agricultural vehicles: a review I. Soil and wheel characteristics,” *Soil Tillage Res.*, vol. 1, pp. 207–237, 1980.

[29] ASTM D6913/D6913M-17, *Standard Test Methods for Particle-Size Distribution (Gradation) of Soils Using Sieve Analysis*. West Conshohocken, PA: ASTM International, 2017.

[30] ASTM D7928-17, *Standard Test Method for Particle-Size Distribution (Gradation) of Fine-Grained Soils Using the Sedimentation (Hydrometer) Analysis*. West Conshohocken, PA: ASTM International, 2017.

[31] ISO 11277:2009, *Soil quality -- Determination of particle size distribution in mineral soil material -- Method by sieving and sedimentation*. ISO/TC 190/SC 3 Chemical and physical characterization, 2009.

[32] ISO 17892-4:2016, *Geotechnical investigation and testing -- Laboratory testing of soil -- Part 4: Determination of particle size distribution*. ISO/TC 182 Geotechnics, 2016.

[33] ASAE EP542 FEB1999 (R2013), *Procedures for Using and Reporting Data Obtained with the Soil Cone Penetrometer*. St. Joseph, Michigan: American Society of Agricultural and Biological Engineers, 2013.

[34] Society of Automotive Engineers, *Off-Road Vehicle Mobility Evaluation, SAE J939*. New York, NY.: SAE International, 1967.

[35] ASTM D7263-09, *Standard Test Methods for Laboratory Determination of Density (Unit Weight) of Soil Specimens*. West Conshohocken, PA: ASTM International, 2009.

[36] ASTM D2216-10, *Standard Test Methods for Laboratory Determination of Water (Moisture) Content of Soil and Rock by Mass*. West Conshohocken, PA: ASTM International, 2010.

[37] ASTM D4643-17, *Standard Test Method for Determination of Water Content of Soil and Rock by Microwave Oven Heating*. West Conshohocken, PA: ASTM International, 2017.

[38] ASTM D4959-16, *Standard Test Method for Determination of Water (Moisture) Content of Soil By Direct Heating*. West Conshohocken, PA: ASTM International, 2016.

[39] J. V Perumpral, "Cone Penetrometer Applications — A Review," *Trans. ASAE*, vol. 30, no. 4, pp. 939–944, 1987.

[40] C. M. P. Vaz and J. W. Hopmans, "Simultaneous Measurement of Soil Penetration Resistance and Water Content with a Combined Penetrometer–TDR Moisture Probe," *Soil Sci. Soc. Am. J.*, vol. 65, no. 1, pp. 4–12, 2001.

[41] M. S. Osman, "The measurement of soil shear strength," *J. Terramechanics*, vol. 1, no. 3, pp. 54–60, 1964.

[42] M. Lyasko, "LSA model for sinkage predictions," *J. Terramechanics*, vol. 47, pp. 1–19, 2010.

[43] M. Tai and M. Tomizuka, "Robust longitudinal velocity tracking of vehicles using traction and brake control," in *6th International Workshop on Advanced Motion Control. Proceedings (Cat. No. 00TH8494)*, 2000, pp. 305–310.

[44] B. Coutermarsh, "Velocity effect of vehicle rolling resistance in sand," *J. Terramechanics*, vol. 44, pp. 275–291, 2007.

[45] H. Taghavifar and A. Mardani, "Investigating the effect of velocity , inflation pressure , and vertical load on rolling resistance of a radial ply tire," *J. Terramechanics*, vol. 50, no. 2, pp. 99–106, 2013.

[46] S. K. Upadhyaya, W. J. Chancellor, and D. Wulfsohn, "Sources of variability in traction data," *J. Terramechanics*, vol. 25, no. 4, pp. 249–272, 1988.

[47] I. J. Guy, "An analysis of the interaction between the front and rear axles of a four-wheel-drive tractor, and its contribution to power delivery efficiency," Harper Adams University College, 2010.

[48] S. D. Naranjo, C. Sandu, S. Taheri, and S. Taheri, "Experimental testing of an off-road instrumented tire on soft soil," *J. Terramechanics*, vol. 56, pp. 119–137, 2014.

[49] I. Shmulevich and A. Osetinsky, “Traction performance of a pushed / pulled drive wheel,” *J. Terramechanics*, vol. 40, no. 1, pp. 33–50, 2003.

[50] R. A. Liston, “The land locomotion laboratory,” *J. Terramechanics*, vol. 2, no. 4, pp. 69–81, 1965.

[51] A. Yahya, M. Zohadie, D. Ahmad, A. K. Elwaleed, and A. F. Kheiralla, “UPM indoor tyre traction testing facility,” *J. Terramechanics*, vol. 44, no. 4, pp. 293–301, 2007.

[52] T. R. Way, “Three single wheel machines for traction and soil compaction Research,” *Agric. Eng. Int. CIGR Ejournal*, vol. XI, pp. 1–24, 2009.

[53] Y. Kawase, H. Nakashima, and A. Oida, “An indoor traction measurement system for agricultural tires,” *J. Terramechanics*, vol. 43, no. 3 SPEC. ISS., pp. 317–327, 2006.

[54] V. K. Tiwari, K. P. Pandey, and A. K. Sharma, “Development of a tyre traction testing facility,” *J. Terramechanics*, vol. 46, no. 6, pp. 293–298, 2009.

[55] A. Mardani, K. Shahidi, and H. K. Maslak, “An indoor traction measurement system to facilitate research on agricultural tires,” *J. Food, Agric. Environ.*, vol. 8, no. 2, pp. 642–646, 2010.

[56] H. Raheman and R. Singh, “Steering forces on undriven tractor wheel,” *J. Terramechanics*, vol. 40, no. 3, pp. 161–178, 2003.

[57] P. Farhadi, A. Mohsenimanesh, R. Alimardani, and H. Ahmadi, “Design and Fabrication of a Single Wheel Tester,” *J. Sci. today’s world*, vol. 2, no. 2, pp. 123–132, 2013.

[58] R. J. Godwin, J. L. Brighton, K. Blackburn, T. E. Richards, D. Ansorge, and P. N. Wheeler, “Off-Road Dynamics Research at Cranfield University at Silsoe,” in *ASAE Annual Meeting*, 2006.

[59] H. Abdolmaleki, A. Jafari, A. Tabatabaeifar, A. Hajiahmad, and H. Goli, “Development and evaluation of an in-situ tire testing facility with variable side slip angles,” *J. Terramechanics*, vol. 59, pp. 49–58, 2015.

[60] W. P. Billington, “The N.I.A.E. Mk II single wheel tester,” *J. Agric. Eng. Res.*, vol. 18, no. 1, pp. 67–70, 1973.

[61] A. K. Nagaoka, K. P. Lancas, P. C. Neto, and S. H. Benez, “Evaluation of a Single Wheel Testing Device with Mechanical Transmission,” in *2001 ASAE Annual International Meeting*, 2001.

[62] K. Armbruster and H. D. Kutzbach, “Combined lateral and longitudinal forces on driven angled tractor tyres,” *J. Terramechanics*, vol. 28, no. 4, pp. 331–338, 1991.

[63] J. A. Pytka *et al.*, “An instrumented vehicle for offroad dynamics testing,” *J. Terramechanics*, vol. 48, no. 5, pp. 384–395, 2011.

[64] S. Shoop and B. Coutermarsh, “Tire Cornering Force Test Method for Winter Surfaces,” in *SAE 2006 World Congress & Exhibition*, 2006.

[65] B. M. Hopkins, “Adaptive Rollover Control Algorithm Based on an Off-Road Tire Model,” Virgnia Tech, 2009.

[66] M. J. Stallmann, P. S. Els, and C. M. Becker, “Parameterization and modelling of large

off-road tyres for ride analyses: Part 1 - Obtaining parameterization data," *J. Terramechanics*, vol. 55, pp. 73–84, 2014.

[67] A. G. Guthrie, T. R. Botha, E. Jimenez, P. S. Els, and C. Sandu, "Dynamic 3D measurement of tyre-terrain interaction," in *19th International and 14th European-African Regional Conference of the ISTVS*, 2017.

[68] A. Mohsenimanesh and S. M. Ward, "On-the-move monitoring of soil-tire interaction on soft soil using wireless data acquisition," *Trans. ASABE*, vol. 50, no. 6, pp. 1919–1925, 2007.

[69] G. Krick, "Radial and shear stress distribution beneath rigid wheels and pneumatic tyres on yielding soils with regard to tyre deformation," *J. Terramechanics*, vol. 6, no. 3, pp. 73–98, 1969.

[70] H. Jun, T. Kishimoto, T. R. Way, and T. Taniguchi, "Three-directional contact stress distributions for a pneumatic tractor tire in soft soil," *Trans. ASAE*, vol. 41, no. 5, pp. 1237–1242, 1998.

[71] R. D. Wismer and H. J. Luth, "Off-road traction prediction for wheeled vehicles," *J. Terramechanics*, vol. 10, no. 2, pp. 49–61, 1973.

[72] J. Madsen *et al.*, "A Physics-Based Vehicle/Terrain Interaction Model for Soft Soil Off-Road Vehicle Simulations," *SAE Int. J. Commer. Veh.*, vol. 5, no. 1, pp. 280–290, 2012.

[73] J. C. Madsen, "Mobility Prediction of Multi-Body Vehicle Dynamics Handling Simulations on Deformable Terrain," UNIVERSITY OF WISCONSIN–MADISON, 2014.

[74] C. H. Liu, J. Y. Wong, and H. A. Mang, "Large strain finite element analysis of sand: model, algorithm and application to numerical simulation of tire-sand interaction," *Comput. Struct.*, vol. 74, no. 3, pp. 253–265, 2000.

[75] H. Nakashima and A. Oida, "Algorithm and implementation of soil–tire contact analysis code based on dynamic FE–DE method," *J. Terramechanics*, vol. 41, pp. 127–137, 2004.

[76] S. K. Upadhyaya, J. Mehlschau, D. Wulfsohn, and J. L. Glancey, "Development of a Unique, Mobile, Single Wheel Traction Testing Machine," *Trans. ASAE*, vol. 29, no. 5, pp. 1243–1246, 1986.

[77] S. K. Upadhyaya, "Effect of tread design on bias ply tire tractive characteristics," *Trans. ASAE*, vol. 31, no. 5, pp. 1338–1344, 1988.

[78] S. K. Upadhyaya, D. Wulfsohn, and G. Jubbal, "Traction prediction equations for radial ply tyres," *J. Terramechanics*, vol. 26, no. 2, pp. 149–175, 1989.

[79] S. K. Upadhyaya and D. Wulfsohn, "Traction prediction using soil parameters obtained with an instrumented analog device," *J. Terramechanics*, vol. 30, no. 2, pp. 85–100, 1993.

[80] S. K. Upadhyaya, M. Sime, N. Raghuwanshi, and B. Adler, "Semi-empirical traction prediction equations based on relevant soil parameters," *J. Terramechanics*, vol. 34, no. 3, pp. 141–154, 1997.

[81] E. Bakker, L. Nyborg, and H. B. Pacejka, "Tyre modelling for use in vehicle dynamics studies," *SAE Technical Paper 870421*. 1987.

[82] J. J. M. van Oosten and E. Bakker, “Determination of magic tyre model parameters,” *Veh. Syst. Dyn.*, vol. 21, no. S1, pp. 19–29, 1992.

[83] J. A. Cabrera, A. Ortiz, E. Carabias, and A. Simon, “An Alternative Method to Determine the Magic Tyre Model Parameters Using Genetic Algorithms,” *Veh. Syst. Dyn.*, vol. 41, no. 2, pp. 109–127, 2004.

[84] A. Ortiz, J. A. Cabrera, A. J. Guerra, and A. Simon, “An easy procedure to determine Magic Formula parameters: A comparative study between the starting value optimization technique and the IMMa optimization algorithm,” *Veh. Syst. Dyn.*, vol. 44, no. 9, pp. 689–718, 2006.

[85] H. B. Pacejka and E. Bakker, “The magic formula tyre model,” *Veh. Syst. Dyn.*, vol. 21, no. S1, pp. 1–18, 1992.

[86] G. Komandi, “Reevaluation of the adhesive relationship between the tire and the soil,” *J. Terramechanics*, vol. 30, no. 2, pp. 77–83, 1993.

[87] J.-Y. Wong and A. R. Reece, “Prediction of rigid wheel performance based on the analysis of soil-wheel stresses part I. Performance of driven rigid wheels,” *J. o/Terramechanics*, vol. 4, no. 1, pp. 81–98, 1967.

[88] M. Apfelbeck, S. Kuß, B. Rebele, and B. Schäfer, “A systematic approach to reliably characterize soils based on Bevameter testing,” *J. Terramechanics*, vol. 48, no. 5, pp. 360–371, 2011.

[89] J. Massah and S. Noorolahi, “Design, development and performance evaluation of a tractor-mounted bevameter,” *Soil Tillage Res.*, vol. 110, no. 1, pp. 161–166, 2010.

[90] H. Nakashima, Y. Takatsu, H. Shinone, H. Matsukawa, and T. Kasetani, “FE-DEM analysis of the effect of tread pattern on the tractive performance of tires operating on sand,” *J. Mech. Syst. Transp. Logist.*, vol. 2, no. 1, pp. 55–65, 2009.

[91] P. V. Lade, “Overview of constitutive models for soils,” in *Geo-Frontiers Congress 2005*, 2005, pp. 1–34.

[92] R. F. Scott, “Plasticity and constitutive relations in soil mechanics,” *J. Geotech. Eng.*, vol. 111, no. 5, pp. 559–605, 1985.

[93] F. L. DiMaggio and I. S. Sandler, “Material model for granular soils,” *J. Eng. Mech.*, 1971.

[94] K. Roscoe and J. B. Burland, “On the generalized stress-strain behaviour of wet clay,” 1968.

[95] M. Gysi, V. Maeder, and P. Weisskopf, “Pressure distribution underneath tires of agricultural vehicles,” *Trans. ASAE*, vol. 44, no. 6, pp. 1385–1389, 2001.

[96] L. Chi, S. Tessier, and C. Lague, “Finite element prediction of soil compaction induced by various running gears,” *Trans. ASAE*, vol. 36, no. 3, pp. 629–636, 1993.

[97] J. E. Saliba, “Elastic-viscoplastic finite-element program for modeling tire/soil interaction,” *J. Aircr.*, vol. 27, no. 4, pp. 350–357, 1990.

[98] H. D. Hibbit, B. I. Karlsson, and E. P. Sorensen, “ABAQUS user manual, version 6.12,” *Simulia*. Simulia, Providence, RI., 2012.

[99] S. A. Shoop, “Finite element modeling of tire-terrain interaction (ERDC/CRREL TR-01-16),” ENGINEER RESEARCH AND DEVELOPMENT CENTER HANOVER NH COLD REGIONS RESEARCH AND ENGINEERING LAB, 2001.

[100] C. W. Fervers, “Improved FEM simulation model for tire–soil interaction,” *J. Terramechanics*, vol. 41, no. 2–3, pp. 87–100, 2004.

[101] K. Xia, “Finite element modeling of tire/terrain interaction: Application to predicting soil compaction and tire mobility,” *J. Terramechanics*, vol. 48, no. 2, pp. 113–123, 2011.

[102] H. Li, “Analysis of Off-Road Tire-Soil Interaction through Analytical and Finite Element Methods,” TU Kaiserslautern, 2013.

[103] H. Yamashita, P. Jayakumar, M. Alsaleh, and H. Sugiyama, “Physics-Based Deformable Tire–Soil Interaction Model for Off-Road Mobility Simulation and Experimental Validation,” *J. Comput. Nonlinear Dyn.*, vol. 13, no. 2, p. 021002, 2018.

[104] Z. Asaf, D. Rubinstein, and I. Shmulevich, “Determination of discrete element model parameters required for soil tillage,” *Soil Tillage Res.*, vol. 92, no. 1–2, pp. 227–242, 2007.

[105] P. Schjønning, M. Lamande, F. A. Tøgersen, J. Arvidsson, and T. Keller, “Modelling effects of tyre inflation pressure on the stress distribution near the soil – tyre interface,” *Biosyst. Eng.*, vol. 99, no. 1, pp. 119–133, 2008.

[106] P. Schjønning, M. Stettler, T. Keller, P. Lassen, and M. Lamandé, “Predicted tyre-soil interface area and vertical stress distribution based on loading characteristics,” *Soil Tillage Res.*, vol. 152, pp. 52–66, 2015.

[107] A. Mohsenimanesh, S. M. Ward, P. O. M. Owende, and A. Javadi, “Modelling of pneumatic tractor tyre interaction with multi-layered soil,” *Biosyst. Eng.*, vol. 104, no. 2, pp. 191–198, 2009.

[108] C. Salot, P. Gotteland, and P. Villard, “Influence of relative density on granular materials behavior: DEM simulations of triaxial tests,” *Granul. Matter*, vol. 11, no. 4, pp. 221–236, 2009.

[109] J.-P. Plassiard, N. Belheine, and F.-V. Donzé, “A spherical discrete element model: calibration procedure and incremental response,” *Granul. Matter*, vol. 11, no. 5, pp. 293–306, 2009.

[110] N. Belheine, J. P. Plassiard, F. V. Donzé, F. Darve, and A. Seridi, “Numerical simulation of drained triaxial test using 3D discrete element modeling,” *Comput. Geotech.*, vol. 36, no. 1–2, pp. 320–331, 2009.

[111] W. Smith, “Modeling of Wheel-Soil Interaction for Small Ground Vehicles Operating on Granular Soil,” University of Michigan, 2014.

[112] Z. Zheng, M. Zang, S. Chen, and H. Zeng, “A GPU-based DEM-FEM computational framework for tire-sand interaction simulations,” *Comput. Struct.*, vol. 209, pp. 74–92, 2018.

[113] O. G. Cueto, C. E. I. Coronel, C. A. R. Morfa, L. H. H. Sosa, Guillermo Urriolagoitia Gómez, G. U. Calderón, and M. H. Suárez, “Three dimensional finite element model of

soil compaction caused by agricultural tire traffic," *Comput. Electron. Agric.*, vol. 99, pp. 146–152, 2013.

[114] N. Moslem and G. Hossein, "Numerical simulation of tire/soil interaction using a verified 3D finite element model," *J. Cent. South Univ.*, vol. 21, no. 2, pp. 817–821, 2014.

[115] P. Gotteland and O. Benoit, "Sinkage tests for mobility study, modelling and experimental validation," *J. Terramechanics*, vol. 43, no. 4, pp. 451–467, 2006.

[116] J. Y. Wong, "Data processing methodology in the characterization of the mechanical properties of terrain," *J. Terramechanics*, vol. 17, no. 1, pp. 13–41, 1980.

[117] S. K. Upadhyaya, D. Wulfsohn, and J. Mehlschau, "An instrumented device to obtain traction related parameters," *J. Terramechanics*, vol. 30, no. 1, pp. 1–20, 1993.

[118] C. W. Plackett, "A review of force prediction methods for off-road wheels," *J. Agric. Eng. Res.*, vol. 31, no. 1, pp. 1–29, 1985.

[119] R. L. Raper, A. C. Bailey, E. C. Burt, T. R. Way, and P. Liberati, "Inflation pressure and dynamic load effects on soil deformation and soil–tire interface stresses," *Trans. ASAE*, vol. 38, no. 3, pp. 685–689, 1995.

[120] R. L. Raper, A. C. Bailey, E. C. Burt, T. R. Way, and P. Liberati, "The effects of reduced inflation pressure on soil-tire interface stresses and soil strength," *J. Terramechanics*, vol. 32, no. 1, pp. 43–51, 1995.

[121] A. K. Elwaleed, A. Yahya, M. Zohadie, D. Ahmad, and A. F. Kheiralla, "Effect of inflation pressure on motion resistance ratio of a high-lug agricultural tyre," *J. Terramechanics*, vol. 43, pp. 69–84, 2006.

[122] D. Wulfsohn, S. K. Upadhyaya, and W. J. Chancellor, "Tractive characteristics of radial ply and bias ply tyres in a California soil," *J. Terramechanics*, vol. 25, no. 2, pp. 111–134, 1988.

[123] L. L. Bashford, S. Al-Hamed, and C. Jenane, "Effects of tire size and inflation pressure on tractive performance," *Appl. Eng. Agric.*, vol. 9, no. 4, pp. 343–348, 1993.

[124] I. J. M. Besselink, A. J. C. Schmeitz, and H. B. Pacejka, "An improved Magic Formula/Swift tyre model that can handle inflation pressure changes," *Veh. Syst. Dyn.*, vol. 48, no. S1, pp. 337–352, 2010.

[125] K. Höpping, K. Augsburg, and F. Büchner, "Extending the Magic Formula Tire Model for Large Inflation Pressure Changes by Using Measurement Data from a Corner Module Test Rig," *SAE Int. J. Passeng. Cars - Mech. Syst.*, vol. 11, no. 2, pp. 1–11, 2018.

[126] A. J. C. Schmeitz, I. J. M. Besselink, J. de Hoogh, and H. Nijmeijer, "Extending the Magic Formula and SWIFT tyre models for inflation pressure changes," *VDI BERICHTE*, vol. 1912, pp. 201–225, 2005.

[127] S. D. Naranjo, "Experimental investigation of the tractive performance of an instrumented off road tire on a soft soil terrain," Virginia Tech, 2013.

[128] A. K. Bhoopalam, "Pneumatic tire performance on ice," Virginia Tech, 2015.

[129] Tekscan Inc., "Pressure Mapping Sensor 3150," 2018. [Online]. Available: https://www.tekscan.com/products-solutions/pressure-mapping-

sensors/3150?tab=electronics.

[130] Campbell Scientific Inc., “HS2 and HS2P Instruction Manual,” 2016. [Online]. Available: https://s.campbellsci.com/documents/au/manuals/hs2.pdf.

[131] Humboldt Mfg. Co., “HS-4210 product manual,” 2015. [Online]. Available: https://www.humboldtmfg.com/manuals/HS-4210_MAN_0815.pdf.

[132] ASTM D698-12e2, “Standard Test Methods for Laboratory Compaction Characteristics of Soil Using Standard Effort (12 400 ft-lbf/ft3 (600 kN-m/m3)).” ASTM International, West Conshohocken, PA, pp. 1–13, 2012.

[133] D. R. Freitag, “A dimensional analysis of the performance of pneumatics tires on clay,” *J. Terramechanics*, vol. 3, no. 3, pp. 51–68, 1966.

[134] Tekscan Inc., “I-Scan User Manual v.5.9x,” 2006. [Online]. Available: https://www.tekscan.com/products-solutions/systems/i-scan-system.

[135] H. Schwanghart, “Measurement of contact area, contact pressure and compaction under tires in soft soil,” *J. Terramechanics*, vol. 28, no. 4, pp. 309–318, 1991.

[136] R. A. Irani, R. J. Bauer, and A. Warkentin, “Modelling a Single-Wheel Testbed for Planetary Rover Applications,” in *ASME 2010 Dynamic Systems and Control Conference*, 2010, pp. 181–188.

[137] C. Senatore, M. Wulfmeier, I. Vlahinić, J. Andrade, and K. Iagnemma, “Design and implementation of a particle image velocimetry method for analysis of running gear-soil interaction,” *J. Terramechanics*, vol. 50, no. 5–6, pp. 311–326, 2013.

[138] S. Ozaki, K. Hinata, C. Senatore, and K. Iagnemma, “Finite element analysis of periodic ripple formation under rigid wheels,” *J. Terramechanics*, vol. 61, pp. 11–22, 2015.

[139] E. N. Slyuta, “Physical and Mechanical Properties of the Lunar Soil (A Review),” *Sol. Syst. Res.*, vol. 48, no. 5, pp. 330–353, 2015.

[140] J. Wang, L. Alexander, and R. Rajamani, “Friction Estimation on Highway Vehicles Using Longitudinal Measurements,” *J. Dyn. Syst. Meas. Control*, vol. 126, no. 2, p. 265, 2004.

[141] I. C. Holm, “Multi-pass behaviour of pneumatic tires,” *J. Terramechanics*, vol. 6, no. 3, pp. 47–71, 1969.

[142] M. Lyasko, “Multi-pass effect on off-road vehicle tractive performance,” *J. Terramechanics*, vol. 47, no. 5, pp. 275–294, 2010.

[143] J. . Hernanz, H. Peixoto, C. Cerisola, and V. Sánchez-Girón, “An empirical model to predict soil bulk density profiles in field conditions using penetration resistance, moisture content and soil depth,” *J. Terramechanics*, vol. 37, no. 4, pp. 167–184, 2000.

[144] C. M. P. Vaz, J. M. Manieri, I. C. de Maria, and M. Tuller, “Modeling and correction of soil penetration resistance for varying soil water content,” *Geoderma*, vol. 166, no. 1, pp. 92–101, 2011.

[145] P. Ayers and J. Perumpral, “Moisture and density effect on cone index,” *Trans. ASAE*, vol. 25, no. 5, pp. 1169–1172, 1982.

[146] J. Lin, Y. Sun, and P. Schulze Lammers, “Evaluating model-based relationship of cone index, soil water content and bulk density using dual-sensor penetrometer data,” *Soil Tillage Res.*, vol. 138, pp. 9–16, 2014.

[147] P. C. Hansen, V. Pereyra, and G. Scherer, *Least squares data fitting with applications*. JHU Press, 2013.

[148] R. He, E. Jimenez, D. Savitski, C. Sandu, and V. Ivanov, “Investigating the parameterization of Dugoff tire model using experimental tire-ice data,” *SAE Int. J. Passeng. Cars - Mech. Syst.*, vol. 10, no. 1, pp. 83–92, 2017.

[149] D. Savitski *et al.*, “Improvement of traction performance and off-road mobility for a vehicle with four individual electric motors: Driving over icy road,” *J. Terramechanics*, vol. 69, pp. 33–43, 2017.

[150] ANSI/ASAE S296.5 DEC2003 (R2018), *General Terminology for Traction of Agricultural Traction and Transport Devices and Vehicles*. St. Joseph, Michigan: American Society of Agricultural and Biological Engineers, 2018.

[151] ASTM F2493 - 19, *Standard Specification for P225/60R16 97S Radial Standard Reference Test Tire*. West Conshohocken, PA: ASTM International, 2019.

[152] L. Ding, H. Gao, Z. Deng, and J. Tao, “Wheel slip-sinkage and its prediction model of lunar rover,” *J. Cent. South Univ. Technol.*, vol. 17, no. 1, pp. 129–135, 2010.

[153] C. Senatore, “Prediction of mobility, handling, and tractive efficiency of wheeled off-road vehicles,” Virginia Polytechnic Institute and State University, 2010.

[154] C. Senatore and C. Sandu, “Torque distribution influence on tractive efficiency and mobility of off-road wheeled vehicles,” *J. Terramechanics*, vol. 48, no. 5, pp. 372–383, 2011.

[155] Y. Chen, “Modeling, Control, and Design Study of Balanced Pneumatic Suspension for Improved Roll Stability in Heavy Trucks,” Virginia Polytechnic Institute and State University, 2017.

[156] Y. Chen, A. W. Peterson, and M. Ahmadian, “Achieving anti-roll bar effect through air management in commercial vehicle pneumatic suspensions,” *Veh. Syst. Dyn.*, vol. 57, no. 12, pp. 1775–1794, 2019.